Dissertation
submitted to the
Combined Faculties for the Natural Sciences and for Mathematics
of the Ruperto-Carola University of Heidelberg, Germany
for the degree of
Doctor of Natural Sciences

presented by

Diplom-Physiker:	**Marcus Feierabend**
born in:	**Kaiserslautern**
Oral examination:	**30.06.2004**

Coherence-Gated Wave-Front Sensing
in Strongly Scattering Samples

Referees:	**Prof. Dr. Winfried Denk**
	Prof. Dr. Josef F. Bille

Zusammenfassung

In dieser Arbeit wird die Kohärenzgatter-Wellenfrontabtastung (CGWS), eine neue Methode um Wellenfronten in stark streuenden Proben zu messen, vorgestellt. Diese Methode kombiniert Shack-Hartmann Wellenfrontabtastung und Phasen-Verschiebungs-Interferometrie (PSI). Sie bedient sich virtueller Linsen um die Funktion eines konventionellen Shack-Hartmann Sensors zu imitieren. Die Benutzung eines modalen Rekonstruktionsalgorithmus erlaubt die Approximation der gemessenen Wellenfront in einer Linearkombination von Zernike Polynomen bis zum fünften radialen Grad.

Das Prinzip von CGWS wird an Messungen von zwei Wellenfrontaberrationen, Defokus und Astigmatismus, für eine Spiegelprobe und für eine stark streuende Probe getestet. Die Ergebnisse werden mit theoretischen Modellen verglichen. Der Hauptvorteil von CGWS ist die Unterdrückung von Licht welches nicht aus der Fokusregion zurückgestreut wird. Ein weiterer Vorteil ist die Erhöhung der effektiven Detektionssensitivität. Die Fähigkeiten von CGWS werden anhand von Wellenfrontmessungen in streuenden Proben mit einem Streuhintergrund, welcher das nutzbare Signal um etwa drei Größenordnungen übertrifft, demonstriert.

Für verschiedene Mikroskopieanwendungen könnte die Fähigkeit, die Wellenfront aufgrund von CGWS Meßdaten vorzukorrigieren, zu einer Verbesserung des optischen Fokus und damit zu einer erheblichen Steigerung der Auflösung und Tiefeneindringung in Gewebe führen.

Abstract

In this thesis coherence-gated wave-front sensing (CGWS), a new approach for measuring wave-fronts in strongly scattering samples, is presented. This method combines Shack-Hartmann wave-front sensing and phase shifting interferometry (PSI). It employs virtual lenses to mimic the function of a conventional Shack-Hartmann sensor. The use of a modal estimation algorithm allows an approximation of the measured wave-front with a linear combination of Zernike polynomials up to the fifth radial degree.

The principle of CGWS is tested by measuring two wave-front aberrations, defocus and astigmatism, for a mirror as a sample and a strongly scattering sample. The results are compared to theoretical models. The main advantage of CGWS is the discrimination against light backscattered from outside the focal region. A further advantage is the increase in the effective detection sensitivity. The capabilities of CGWS are demonstrated with wave-front measurements in scattering samples in the presence of background light that is dominant by about three orders of magnitude.

In various microscopy applications, the ability to pre-emptively correct the wave-front, employing CGWS measurement data, may allow improvements of the optical focus and thus enhance the resolution and depth penetration in tissue considerably.

CONTENTS

1 INTRODUCTION AND MOTIVATION 1

2 METHODS 4

2.1 Two-Photon Microscopy 4

2.2 Wave-front Sensing 7
  2.2.1 Shack-Hartmann Wave-Front Sensing 8
  2.2.2 Phase Shifting Interferometry 18

2.3 Mie Theory 22
  2.3.1 Scattering Properties in Detail 22

2.4 Coherence-Gated Wave-Front Sensing 27
  2.4.1 The Light Source 27
  2.4.2 The CCD Camera 28
  2.4.3 Implementation of CGWS – The Setup 34
  2.4.4 Piezo Control 44
  2.4.5 Dispersion Compensation 48

3 RESULTS AND DISCUSSION 55

3.1 Experiments with a Quasi Point Source 55
  3.1.1 Defocus with a Mirror Sample 55
  3.1.2 Astigmatism with a Mirror Sample 64

3.2 Experiments with Scattering Samples 70
  3.2.1 Scattering Samples 70
  3.2.2 Defocus with a Scattering Sample 74
  3.2.3 Astigmatism with a Scattering Sample 84
  3.2.4 Sensitivity and Accuracy 85

4 SUMMARY AND FUTURE PROSPECTS 89

REFERENCES 93

ACKNOWLEDGMENTS 99

Acronyms

Acronym	Expression
AWF	aberrated wave-front
BFP	back focal plane
CG	coherence gate
CGWS	coherence-gated wave-front sensing
FUL	fraction of useful light
FWHM	full width at half maximum
GVD	group velocity dispersion
MFP	mean free path length
OA	optical axis
PSD	position-sensitive detector
QPS	quasi point source
SHS	Shack-Hartmann wave-front sensor
TPE	two-photon excitation
TPM	two-photon microscopy
TRA	transverse ray aberration
VLC	virtual lenslet compartment

1 Introduction and Motivation

For many biomedical questions the detailed study of cellular processes in intact tissue is increasingly necessary. Light is refracted but barely absorbed in most biological tissues [Svoboda and Block 1994]. This is the result of a combination of two facts: First, the index of refraction varies locally due to the non-uniformly distribution of the cellular constituents within a cell. Second, within the visible and the near-infrared range of the electromagnetic spectrum the density of light absorbing molecules in most tissues is relatively low. Therefore light can penetrate into tissue but the effects of scattering often make it impossible to achieve diffraction-limited resolution. Yet for the examination of sub-cellular processes a resolution in the sub-micrometer range is often crucial. For example the chemical dynamics of intracellular second messengers in single dendritic spines [Denk et al. 1995], [Denk et al. 1996], [Yuste et al. 1999], [Oertner et al. 2002] play a major role in memory building modifications of synaptic connections in the brain.

Confocal microscopy [Minsky 1961], [Minsky 1988] eliminates scattered and out-of-focus light. But thereby it produces especially in scattering tissues considerable high photo-damage. This was reduced with the development of multi photon laser scanning microscopy (MPLSM) [Denk et al. 1990], [Denk and Svoboda 1997], which can use scattered fluorescence light without loss of resolution [Denk et al. 1994], [Centonze and White 1998]. Nevertheless here too scattering and wave-front aberrations of the excitation light limit the tissue penetration depth [Svoboda et al. 1997].

The efficiency of multi-quantum excitation increases nonlinearly with the local light intensity (to the n^{th} power) [Göppert-Mayer 1931], [Kaiser and Garrett 1961] depending, therefore, strongly on the quality of the optical focus. This is the reason why resolution and excitation efficiency of MPLSM are affected strongly by wave-front aberrations. Therefore pre-emptive corrections of the wave-front are expected to improve optical resolution and excitation efficiency considerably. As a result, tissue depth penetration would be increased significantly.

In astronomy a problem similar to the distortion of the laser focus by refractive index inhomogeneities is the distortion caused by propagation of light from stars through the (turbulent) atmosphere. Astronomers have been alleviating this problem by means of adaptive optics [Merkle et al. 1989]. The first of two steps is the measurement of the distortion, for example, by using light from a bright star [Merkle et al. 1989] or from an artificial reference. These “laser guide-stars” were suggested by Linnik [Linnik 1993] and Foy and Labeyrie [Foy and Labeyrie 1985] and realized by Humphreys et al. [Humphreys et al. 1991]. The second step, first proposed by Babcock [Babcock 1953], is to adapt the shape of a reflecting element so that the distortions of the optical wave-front are cancelled upon reflection.

In microscopy, where the same or similar optical corrector elements as in astronomy can be used [Albert et al. 2000], the determination of the wave-front aberration often requires a very different approach since neither natural nor artificial “guide stars” are available. The only situation where wave-front measuring techniques from astronomy can be directly applied is when the reflected light comes primarily from the focal plane. This is the case in the eye, where a single tissue layer (the retina) reflects or backscatters most of the light, which can then be used to determine the distortion caused by the intervening lens and cornea [Bille et al. 1989], [Liang et al. 1997]. In less favourable biological specimens one can take advantage of the fact that one has considerable control of and information about the light source, usually a scanned laser. For example, a possible approach is iterative wave-front optimization using a search-algorithm based on trial distortions of the incident wave-front [Neil et al. 2000], [Marsh et al. 2003], [Sherman et al. 2002]. This approach uses the fact that the amount of fluorescence generated by multi-photon absorption (or the fluorescence detected through a near optimal pinhole) strongly depends on the quality of the focus. This trial-and-error approach can be used in thick, scattering samples such as brain tissue, but, first, it requires the presence of a sufficiently bright fluorescence signal and, second, it is only feasible if the search space is sufficiently low dimensional, which limits the order to which distortions can be corrected.

Using all the reflected light indiscriminately for wave-front sensing is not feasible for imaging in scattering samples because most backscattered light comes from superficial layers and consequently does not carry information about the wave-front distortions caused by the tissue. Multi-photon imaging is routinely done to a depth of 3 mean free path lengths (MFPs) and is possible to 5 MFPs [Theer et al. 2003]. With the focus at such depths, the ballistic (unscattered) light from near the focus, which is all that can be used to determine the wave-front distortion, is a miniscule fraction of the total backscatter, which mostly originates from within the first 1.5 MFPs. Light from the focus can, however, be distinguished from multiply-scattered and out-of-focus light by arrival time [Duguay and Mattick 1971], and can be selected, for example, by using non-linear optical gates based e.g. on the Kerr effect [Duguay and Mattick 1971], or a coherent time gate, as in optical coherence tomography [Huang et al. 1991]. For multi-photon microscopy ultra-short-pulse lasers are typically used, which, conveniently, possess the short coherence length needed for coherence gating.

This dissertation describes a new approach to measure the wave-front in strongly scattering samples. It makes use of a short coherence length and does not depend on fluorescence. The wave-front is determined by the use of coherence-gated backscattered light from the focal region (coherence-gated wave-front sensing, CGWS [Feierabend et al. 2004]). CGWS is applicable to samples that are only weakly or sparsely fluorescent, or to specimens that are photosensitive or easily bleached.

This dissertation is structured as follows:

1. Chapter 1 contains the introduction.
2. Chapter 2 is divided into three parts. Part one gives a short overview of the future main application area of CGWS, namely two-photon microscopy. Part two describes the fundamental principles that form the basis for CGWS, phase measurement and depth discrimination with the help of phase shifting interferometry. Part three describes the combination of these two main elements to CGWS. The corresponding setup is illustrated and described in detail.
3. In Chapter 3, the theoretical expectations are derived and compared to the actual measurements. Possible deviations are discussed.
4. Finally, Chapter 4 summarizes the contents of the dissertation, and prospects on the future continuation of this project are given.

2 Methods

This chapter includes four sections. The first section deals with the main envisioned application area of CGWS, two-photon microscopy (TPM). In heterogeneous samples where the index of refraction is spatially inhomogeneous, the optical focus can become severely distorted. Since the efficiency of TPM depends on the squared local light intensity and therefore on the quality of this focus, it is desirable to correct for the arising focus distortions (cf. chapter 1). To perform this correction directly it is necessary to obtain knowledge about these distortions. In order to acquire this knowledge a wave-front measurement in a certain depth of the observed biological sample (cf. chapter 1) has to be done. The tools required for such a task are wave-front sensing and depth discrimination, the main topics of section two in this chapter. In order to be able to test the feasibility of CGWS in scattering media, it is necessary to start with corresponding scattering phantoms for which the result of the CGWS process is predictable. This requires the knowledge of the corresponding scattering properties of such phantoms. To determine these properties the scattering theory of Mie was used. The main features of this theory are outlined in section three of this chapter. Finally, in section four, the combination of the tools described in section two is described.

2.1 Two-Photon Microscopy

It has long been recognized that highly intense light has a potential for triggering nonlinear optical processes. As early as in 1931, Maria Göppert-Mayer predicted the existence of multiphoton excitation processes when working on the theory of two-photon quantum transitions in atoms [Göppert-Mayer 1931]. However, it took thirty years – and required the invention of the laser - until her theory was finally verified. Kaiser and Garret published the first report on two-photon excitation (TPE) of $CaF_2:Eu^{2+}$ fluorescence in 1961 [Kaiser and Garrett 1961]. In 1990 Denk et al. demonstrated the application of TPE of fluorescence to laser scanning microscopy [Denk et al. 1990]. TPE can in general be thought of as the simultaneous absorption of two photons that combine their energies to cause a molecular excitation that would otherwise need a single photon of higher energy. In this context, both photons carry approximately half of the energy that is needed for the single-photon absorption-induced transition (Figure 2.1). The excited molecule is typically a fluorophore. The rate n_a at which such a fluorophore at the center of the focus absorbs photon-pairs can be approximated, following a result from Denk et al. [Denk et al. 1990]:

$$n_a \approx \frac{p_0^2 d}{t_P f_P} \left(\frac{p\ A}{h c_0\, l} \right)^2, \qquad (2.1)$$

where p_0 is the average incident laser power, d the two-photon cross-section, t_p the pulse duration, f_p the pulse repetition rate, A the numerical aperture (NA) of the beam focusing lens, c_0 the speed of light in vacuum, h Planck's constant and l the center wavelength used.

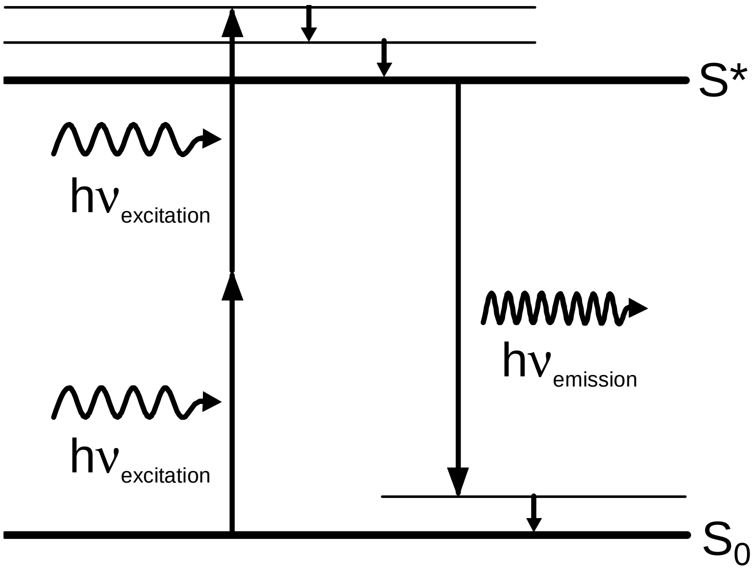

Figure 2.1: Schematic of the TPE principle. By simultaneous absorption of two low energy photons a molecule in its ground state (S_0) is excited to its first excited state (S; here to a vibrational level a little above S*). Through radiationless transitions it relaxes to S*. Via emission of a single high-energy fluorescence photon ($hn_{emission} \leq 2hn_{excitation}$) the molecule usually returns to a vibrational state above S_0.*

From Eq. (2.1) it is apparent that the generated fluorescence signal depends on the square of the instantaneous excitation light intensity. To achieve reasonable excitation levels, intensities in the range of GW/cm^2 are required. Clearly, a biological sample cannot sustain such high laser-powers over a long period of time. However, for the same average incident power, the instantaneous intensity is higher the shorter the laser pulse. Thus, using short pulses has a big advantage as it increases the average two-photon absorption probability. The combination with low repetition-rates, which again increase the two-photon absorption probability, results in high peak-power while the average power is kept low. This permits image acquisition in a reasonable time while using "biologically tolerable" power levels [Denk et al. 1995]. The actual tolerable power level depends on several parameters (for example the tissue and the wavelength) and is the subject of an ongoing debate [König et al. 1999],[Koester et al. 1999],[Hopt and Neher 2001].

The main advantage of TPM over single-photon microscopy techniques is its ability to provide images from deep within scattering tissues. This ability is due to two properties. First, the two excitation photons that act together are low-energy photons, and hence the illumination wavelength used for excitation is relatively long, typically between 800 and 1000 nm. Since scattering for long wavelength light (NIR) is less than for visible light, which is used in single-photon excitation, deeper penetration into biological tissue is feasible. Confocal microscopy [Minsky 1961] has been demonstrated to a depth of 250 micrometer in the rat brain in vivo [Dirnagl et al. 1991]. For TPM, in comparison, Theer et al. [Theer et al. 2003] showed that the depth penetration can reach 1000 µm. It is the further penetration that TPM affords that is crucial for neuroscientists [Denk and Svoboda 1997]. The second property that enables TPM to provide images from deep within scattering tissues is the fact that a signal is only generated in the vicinity of the focus due to the nonlinear dependence on the illumination intensity. This results in intrinsic optical sectioning. In single-photon techniques fluorescence is generated throughout the sample. To obtain three-dimensional information, a confocal pinhole is required to select only fluorescence generated in the focus. In addition, photo-bleaching and photo-damage occur throughout the sample. In the two-photon case all photons are signal because they were generated in the focus. Out-of focus effects are reduced or completely eliminated with TPM (for review see [Helmchen and Denk 2002]) and photo-bleaching and photo-damage are confined to the focal plane.

Another advantage is that UV fluorophores become more accessible with TPE. In one-photon confocal microscopy the excitation of these fluorophores is problematic due to low transmissivity of lenses, lens aberrations and other material problems occuring in that regime of the electromagnetic spectrum.

However, despite the many advantages associated with the three-dimensionally tight localized excitation it should also be kept in mind that the accessible imaging depth strongly depends on the structure of the tissue. Examples include surface blood vessels or cell-body layers that deform the wave-front and hence distort the focus (for review see [Helmchen and Denk 2002]). Difficulties with, or even the impossibility of imaging in the presence of such deformations is the direct consequence.

Due to its advantages TPM is used in many fields. Some examples:

- TPM allows the measurement of dendritic signals induced by light stimuli in the retina. It was recently shown by Euler et al. [Euler et al. 2002] that starburst amacrine cell dendrites possess direction-selective calcium signals and thus are the likely location of motion direction detection in the retina.
- Christie et al. [Christie et al. 2001] demonstrated the possibility of applying TPM to study brain pathologies by monitoring the size of senile plaques in a transgenic mouse model of Alzheimer’s disease. Repeatedly such plaques were imaged through a thinned-skull preparation over periods of up to five months.
- Brown et al. [Brown et al. 2001] introduced multi-photon microscopy for in vivo tumor characterization. Internal regions of tumors, which were previously inaccessible, could be investigated.
- A paper by Kuhn et al. [Kuhn et al. 2004] reveals the option to use voltage sensitive dyes with TPM. This method helps to visualize voltage changes in

cell membranes and thus signal transmission without the invasive use of electrodes.

2.2 Wave-front Sensing

Distortions of the optical focus will lead to a decrease in the TPE efficiency. Often the origin to such distortions is the inhomogeneity of the samples under observation. Their permanently varying index of refraction leads to wave-front aberrations that prevent the formation of a clean focus. Pre-emptive corrections of the wave-front can restore the formation of a clean focus, with the knowledge of the shape of the wave-front and its distortions being the basis for such pre-emptive corrections. Wave-front sensing techniques offer means to obtain this knowledge.

The underlying phenomenon of wave-fronts are three-dimensional waves. For such waves the surfaces joining all points of equal phase at any given time are known as wave-fronts [Hecht 1990]. Hence, wave-fronts represent phase information. But phase is not a measurable parameter since detectors respond to light intensity rather than differences in optical path length. Mostly, this response to intensity is related to some kind of length measurement by means of wave-front sensors [Geary 1995]. This length measurement is given by:

(1) The optical path difference W(x,y) between measured wave-front and a reference wave-front;

(2) The differential phase dW(x,y) between adjacent sampling points in the pupil;

(3) The transverse ray aberration TRA.

Figure 2.2 depicts schematically these three parameters. Depending on the parameters being measured, the measurement is categorized into direct wave-front sensing (if W(x,y) is measured) and indirect wave-front measurement (if either dW(x,y) or TRA are measured) [Geary 1995].

An approximate relation between optical path difference W(x,y) and TRA is (cf. [Rayces 1964])

$$\frac{\partial W(x,y)}{\partial x} = \frac{TRA}{d}. \qquad (2.2)$$

Eq. (2.2) describes the local wave-front slope. Thus, by measuring the TRA, the local slope can be determined so that the original optical path difference W(x,y) can be obtained by integration. If a planar wave-front is taken as the reference wave-front, as is the case in this work, W(x,y) corresponds to the actual wave form.

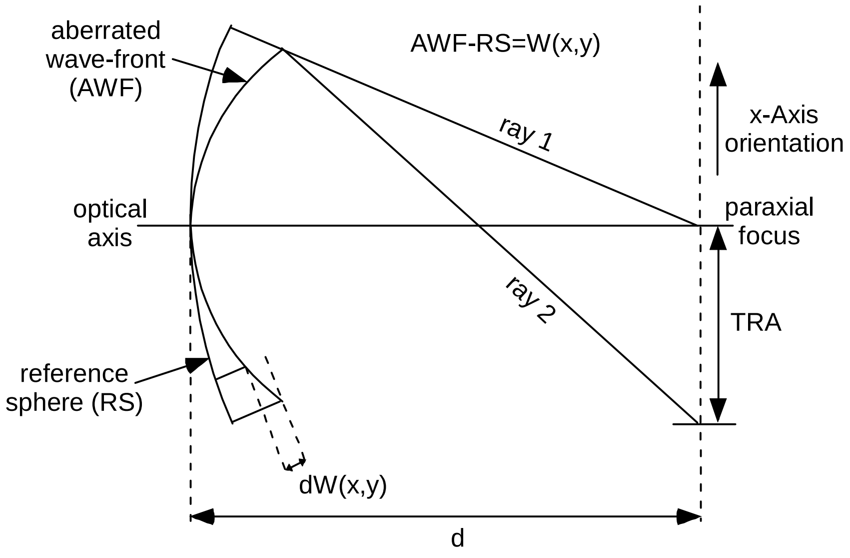

Figure 2.2: Measurable physical parameters of wave-fronts. The rays (e.g. ray1) of a spherical reference wave-front (RS) centered on the optical axis (OA) with radius d would hit a plane perpendicular to the OA at distance d in one point, the paraxial focus. Different from that, the rays (e.g. ray2) of an aberrated wave-front (AWF) would hit the same plane all at different locations. Since every point of the RS corresponds to a point of the AWF every ray of the RS corresponds also to a certain ray of the AWF. Ray1 and ray2 serve as an example. The distance between the points where they hit the plane perpendicular to the OA at distance d is the TRA. The path length difference W(x,y) describes the perpendicular distance from the RS to the AWF. And dW(x,y) denotes the differential path difference between two adjacent sampling points of the AWF with respect to the RS.

The following subsection describes the wave-front sensing technique used for measuring the TRAs, and how from these the original shape of the wave-front can be determined by comparing W(x,y) to a planar wave-front.

2.2.1 Shack-Hartmann Wave-Front Sensing

In indirect wave-front sensing there is a sensor that is based on the classical Hartmann test [Hartmann 1900], [Hartmann 1904], called Shack-Hartmann wave-front sensor (SHS) [Shack and Platt 1971]. This sensor is now the most widely used wave-front sensor for adaptive optics systems [Hardy 1998], [Tyson 1997]. The array of holes used in the classical Hartmann test is in this type of sensor replaced by an array of small lenslets.

From Hartmann test to SHS

An aperture plate with a tiny circular hole is placed in front of a ‘perfect’ lens (cf. Figure 2.3 a and b). The plate can be moved around so that the hole can be positioned anywhere in the entrance pupil. If a measurement is taken every time the hole is moved a distance equal to its own diameter the data sampling looks like Figure 2.3 c.

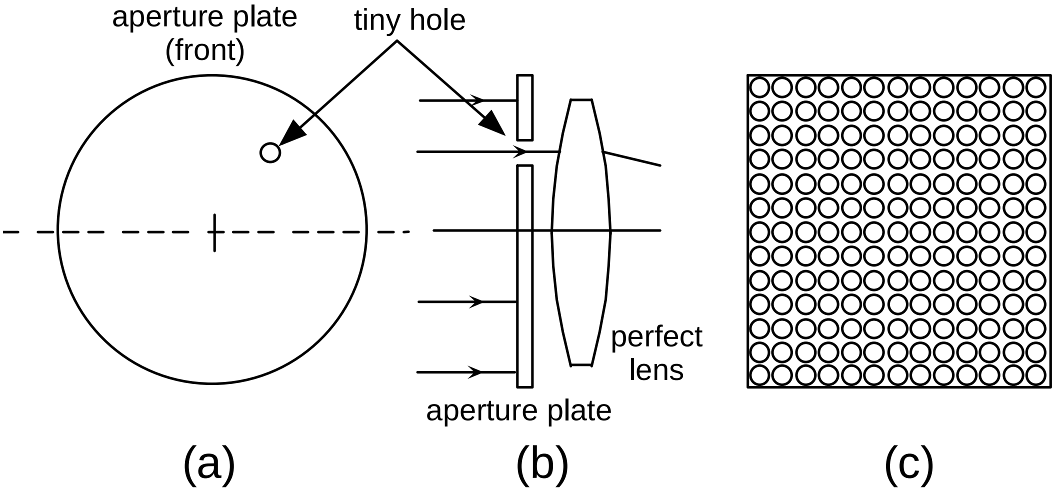

Figure 2.3: The front of an aperture plate with a tiny circular hole (a) that is positioned in front of a 'perfect lens' (b); the plate is moved so that the hole is positioned anywhere in the entrance pupil. The pupil sampling looks then like (c).

If a perfectly planar wave-front is incident on the plate, the hole passes a ray that will cross the OA at the paraxial focal point (Figure 2.4 a). The TRA is then measured with a position-sensitive detector (PSD), e.g. a CCD camera. Since the incoming wave-front is planar, all hole positions will result in a TRA that equals zero. If an AWF is incident, the hole passes a ray, which strikes the focal plane off axis (Figure 2.4 b), which indicates that the TRA is non-zero. Instead of moving one single hole around, an array of sub-apertures can be used to sample the entire wave-front simultaneously. To avoid massive overlap of data a lenslet is embedded in each sub-aperture and a PSD is associated with each sublens. If the sub-apertures are additionally contiguous the resulting system is called a Shack-Hartmann wave-front sensor (cf. Figure 2.5).

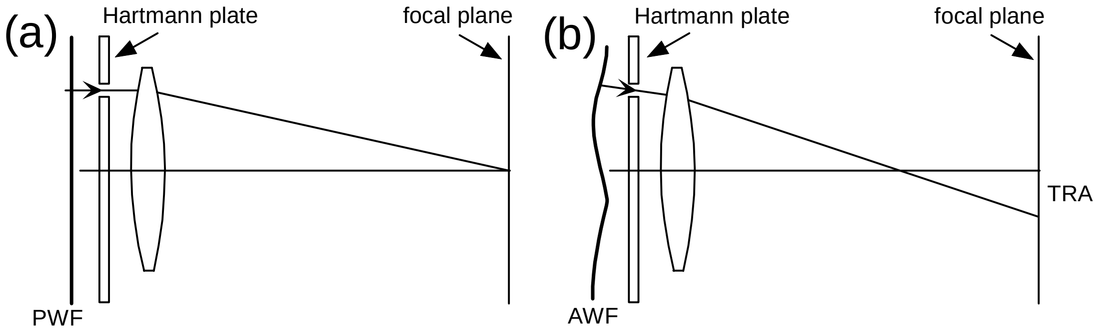

Figure 2.4: The TRA for a planar wave-front (PWF) (a); the TRA for an AWF (b).

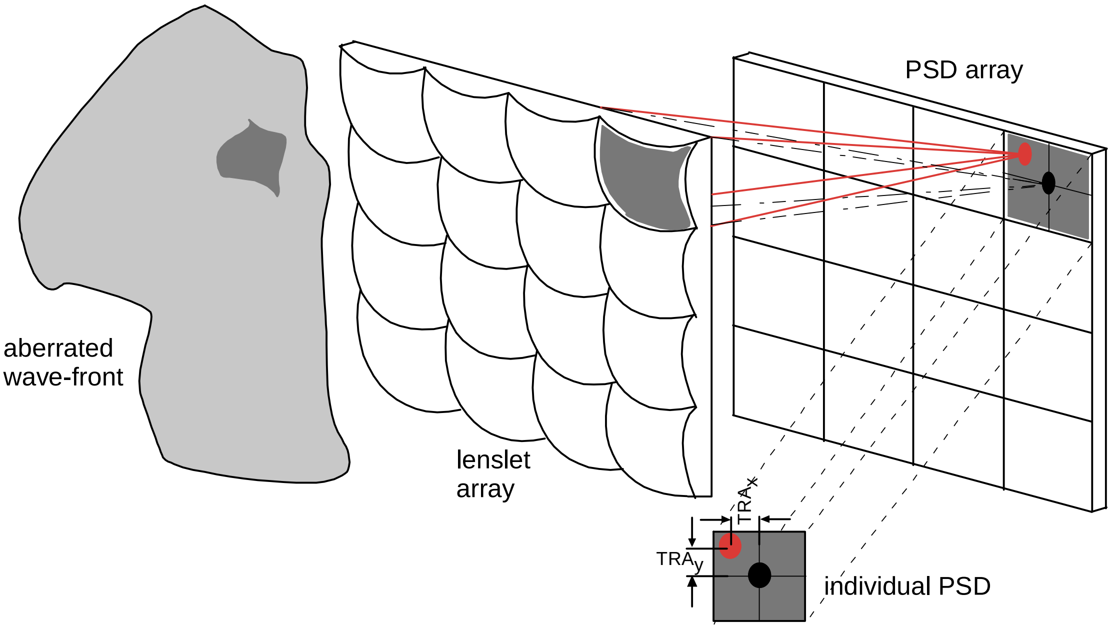

Figure 2.5: The principle of a SHS.

The amount of TRA corresponds to the averaged slope of the wave-front across the lenslet sub-aperture. Since W(x,y) is a function of two variables, two TRAs are present (TRA_x and TRA_y, respectively). The relation between these values and the local derivative of the wave-front for a focal distance *f* is (cf. Figure 2.6)

$$\begin{aligned} \frac{dW(x,y)}{dx} &= \frac{TRA_x}{f} \\ \frac{dW(x,y)}{dy} &= \frac{TRA_y}{f}. \end{aligned} \tag{2.3}$$

In reality the quantum nature of light needs to be taken into account. It is not possible to determine the TRA by simply measuring the distance from the lens center to the exact position where the ray hits the PSD because there is no such exact position. In reality light is not focused on a single point but on an extended diffraction spot. It can be shown [Yura and Tavis 1985] that the average wave-front slope over the sub-aperture of a lenslet is proportional to the displacement (Δx and Δy) of the centroid of the corresponding diffraction spot. The displacements Δx and Δy are the transverse ray aberrations TRA_x and TRA_y.

In consequence Eqs. (2.3) have to be replaced by

$$\begin{aligned} \Delta x &= \frac{f}{A} \int_A \frac{\partial W(x,y)}{\partial x} dx\,dy \\ \Delta y &= \frac{f}{A} \int_A \frac{\partial W(x,y)}{\partial y} dx\,dy, \end{aligned} \tag{2.4}$$

where *A* is the area of the lenslet.

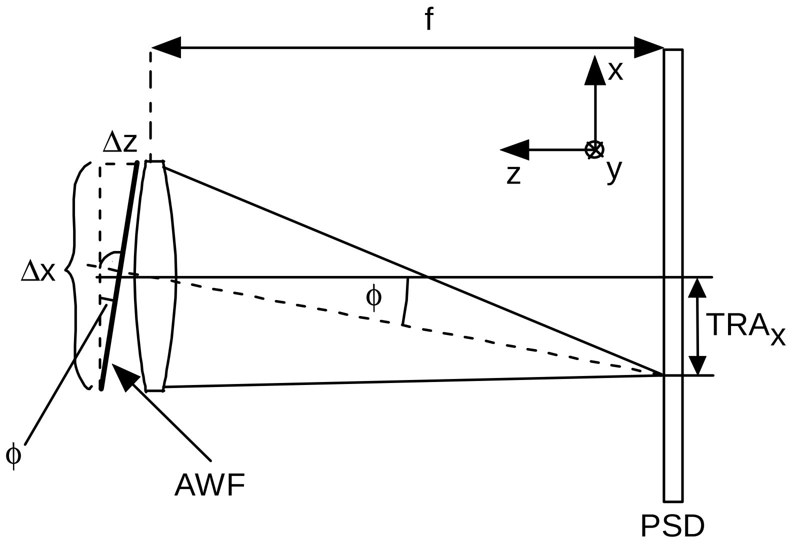

Figure 2.6: Average slope across an individual lens of the lenslet array. The two angles denoted by f are the same, so that tan f =Dz/Dx = TRA_x/f. Since Dz equals DW(x,y), it follows that dW(x,y)/dx = TRA_x/f.

Reconstructing the wave-front

To complete the wave-front sensing process, the original shape of the incident wave-front needs to be recovered. The measured wave-front is usually compared to a reference wave-front, commonly a planar wave-front. Then, for the reconstruction process, it is only necessary to find the optical path length difference W(x,y) since in this case W(x,y) is equivalent to the incident wave-front. In principle the reconstruction of the measured wave-front can be done in two ways, zonal or modal. The zonal approach divides the aperture into an array of independent sub-apertures or zones. For each of these sub-apertures the wave-front is characterized in terms of its optical path length, its local gradient or its local curvature. Most wave-front sensors used in adaptive optics, including the SHS, work on a zonal basis [Hardy 1998]. The modal approach treats the wave-front distortion W(x,y) as a sum of base functions of increasing complexity. A distorted wave-front can be described completely by using either the zonal or the modal wave-front representation [Hardy 1998], which are interchangeable [Tyson 1997]. However there are substantial practical differences between these two approaches. For example zonal systems can easily be expanded to arbitrarily high spatial resolution by increasing the number of sub-apertures while higher order polynomial terms become increasingly difficult to measure. On the other hand, low-order aberrations such as small amounts of defocus, can be described more easily using whole-aperture modes. Since in this work the system was tested with low-order aberrations modal representation was preferred.

As mentioned above, in the modal approach the wave-front is described as a sum of functions with increasing complexity. The Zernike polynomials [Zernike 1934] are a convenient set for this purpose. They are defined on the unit circle and are orthogonal. In this dissertation the widely used Noll normalization [Noll 1976] of these functions is employed:

$$\left.\begin{aligned} Z_{even\ j}(r,q) &= \sqrt{n+1}R_n^m(r)\sqrt{2}\cos mq \\ Z_{odd\ j}(r,q) &= \sqrt{n+1}R_n^m(r)\sqrt{2}\sin mq \end{aligned}\right\} m \neq 0 \qquad Z_j(r,q) = \sqrt{n+1}R_n^0(r) \quad m = 0 \tag{2.5}$$

where

$$R_n^m(r) = \sum_{s=0}^{(n-m)/2} \frac{(-1)^s (n-s)!}{s!\left[(n+m)/2-s\right]!\left[(n-m)/2-s\right]!} r^{n-2s} \ . \tag{2.6}$$

The variables *n* and *m* are integers satisfying $m \le n$ and $n-|m| = even$. The index *j* is a mode ordering number and can be expressed in terms of *n* and *m* as $j = n(n+1)/2 + m + 1$. The number of modes (n_{mds}) for a given radial degree *n* is $n_{mds} = (n+1)(n+2)/2$. The modal orthogonality can be expressed as

$$\int d^2 r\, W(r) Z_i Z_j = d_{ij} \ , \tag{2.7}$$

where d_{ij} is the Kronecker delta and

$$\begin{aligned} W(r) &= 1/p, & r &\le 1 \\ &= 0 & r &> 1 . \end{aligned} \tag{2.8}$$

In Table 2.1 the Zernike polynomials up to the 5th radial degree are listed, and in Figure 2.7 some of them are visualized.

Table 2.1: Zernike polynomials up to the 5th radial degree. For a given radial degree (n) modes with a lower value of azimuthal frequency (m) are ordered first.

radial deg. (n)	Zernike polynomial	Monomial representation	Meaning
0	$Z_1 = 1$	1	piston
1	$Z_2 = 2r\cos(q)$ $Z_3 = 2r\sin(q)$	$2y$ $2x$	tilt about x-axis tilt about y-axis
2	$Z_4 = \sqrt{3}(2r^2 - 1)$	$\sqrt{3}(2x^2 + 2y^2 - 1)$	defocus
	$Z_5 = \sqrt{6}r^2\sin(2q)$ $Z_6 = \sqrt{6}r^2\cos(2q)$	$2\sqrt{6}xy$ $\sqrt{6}(y^2 - x^2)$	astigmatism 45 astigmatism 0 90
3	$Z_7 = \sqrt{8}(3r^3 - 2r)\sin(q)$ $Z_8 = \sqrt{8}(3r^3 - 2r)\cos(q)$	$\sqrt{8}(-2x + 3xy^2 + 3x^3)$ $\sqrt{8}(-2y + 3yx^2 + 3y^3)$	coma along x-axis coma along y-axis
	$Z_9 = \sqrt{8}r^3\sin(3q)$ $Z_{10} = \sqrt{8}r^3\cos(3q)$	$\sqrt{8}(3xy^2 - x^3)$ $\sqrt{8}(y^3 - 3x^2y)$	
4	$Z_{11} = \sqrt{5}(6r^4 - 6r^2 + 1)$	$\sqrt{5}(1 - 6y^2 - 6x^2 + 6y^4 + 12x^2y^2 + 6x^4)$	spherical aberration
	$Z_{12} = \sqrt{10}(4r^4 - 3r^3)\cos(2q)$ $Z_{13} = \sqrt{10}(4r^4 - 3r^3)\sin(2q)$	$\sqrt{10}(-3y^2 + 3x^2 + 4y^4 - 4x^2)$ $\sqrt{10}(-6xy + 8y^3x + 8x^3y)$	
	$Z_{14} = \sqrt{10}r^4\cos(4q)$ $Z_{15} = \sqrt{10}r^4\sin(4q)$	$\sqrt{10}(y^4 - 6x^2y^2 + x^4)$ $\sqrt{10}(y^3x - 4x^3y)$	
5	$Z_{16} = \sqrt{12}(10r^5 - 12r^3 + 3r)\cos(q)$ $Z_{17} = \sqrt{12}(10r^5 - 12r^3 + 3r)\sin(q)$	$\sqrt{12}(3y - 12y^3 - 12x^2y + 10y^5 + 20x^2y^3 + 10x^4y)$ $\sqrt{12}(3x - 12xy^2 - 12x^3 + 10xy^4 + 20x^3y^2 + 10x^5)$	
	$Z_{18} = \sqrt{12}(5r^5 - 4r^3)\cos(3q)$ $Z_{19} = \sqrt{12}(5r^5 - 4r^3)\sin(3q)$	$\sqrt{12}(-4y^3 + 12x^2y + 5y^5 - 10x^2y^3 - 15x^4y)$ $\sqrt{12}(-12xy^2 + 4x^3 + 15xy^4 - 10x^3y^2 - 5x^5)$	
	$Z_{20} = \sqrt{12}r^5\cos(5q)$ $Z_{21} = \sqrt{12}r^5\sin(5q)$	$\sqrt{12}(y^5 - 10x^2y^3 + 5x^4y)$ $\sqrt{12}(5xy^4 - 10x^3y^2 + x^5)$	

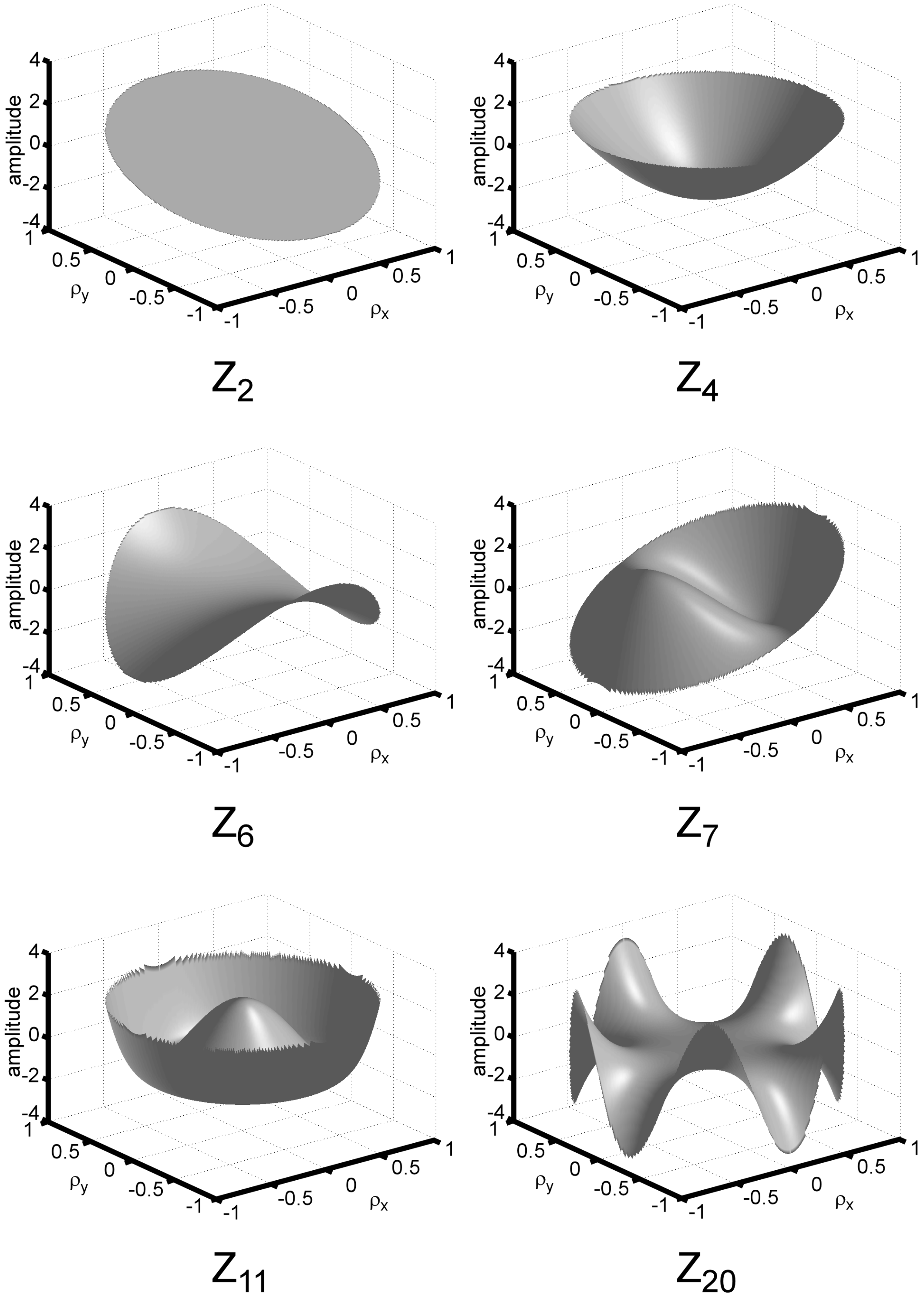

Z_2 Z_4 Z_6 Z_7 Z_{11} Z_{20}

Figure 2.7: Examples of Zernike polynomials representing the primary wave aberrations (Z_2 tilt, Z_4 defocus, Z_6 astigmatism, Z_7 coma, Z_{11} spherical aberration) and a 5 th-order term (Z_{20}).

With the Zernike polynomials the wave-front distortion, i.e. the optical path length difference W described above, can be expanded like:

$$W(r,q) = \sum_{j=1}^{\infty} c_j Z_j(r,q)\,. \tag{2.9}$$

Most PSDs measure shifts in the *x* and *y* directions rather than *r* and *q* directions. Therefore it is common to use the monomial representation, i.e. powers of *x* and *y*, of the Zernike polynomials. It must be kept in mind that due to the limitation to the unit circle x and y only take values between –1 and 1. A description of how the corresponding conversion can be performed is given in [Malacara 1992]. In monomial representation Eq. (2.9) becomes

$$W(x,y) = \sum_{i} k_i Z_i(x,y)\,. \tag{2.10}$$

The corresponding Zernike coefficients k_i can be determined via a modal estimation algorithm [Cubalchini 1979] using the measured average slope values, i.e. the gradients of the wave-front across the sub-apertures.

Assuming that the wave-front sensor measures the x-directional derivative, i.e. the slope of the phase denoted A, and the y-directional derivative, the slope of the phase denoted B, that is

$$\begin{aligned} A(x,y)_s &= \frac{\partial W(x,y)_s}{\partial x} \\ B(x,y)_s &= \frac{\partial W(x,y)_s}{\partial y}\,, \end{aligned} \tag{2.11}$$

where $(x,y)_s$ are the measured coordinates for the s^{th} sub-aperture, then the measured values can be combined into the vector $\vec{M}$

$$\vec{M} = \{A(x,y)_1, A(x,y)_2, \ldots, A(x,y)_L, B(x,y)_1, B(x,y)_2, \ldots, B(x,y)_L\}^T\,. \tag{2.12}$$

In reality the elements of $\vec{M}$ are averages of the directional derivatives across the sub-apertures (cf. the TRAs Eqs.(2.4)). Starting from $\vec{M}$, the estimation process will give a set of constants represented by the vector $\hat{K}$

$$\hat{K} = \left\{\hat{k}_2, \hat{k}_3, \ldots, \hat{k}_I\right\}, \tag{2.13}$$

with an estimated wave-front

$$\hat{W}(x, y) = \sum_{i=2}^{I} \hat{k}_i Z_i(x, y). \tag{2.14}$$

The term $\hat{k}_1 \cdot Z_1(x, y)$ corresponds to piston, a constant shift of the wave-front, and therefore usually is omitted. The criterion for finding $\hat{K}$ was, in the case of this dissertation, to minimize the squared error between the measurement and the estimate. Since the elements of $\vec{M}$ are the values of the wave-front gradients at the different locations of the sub-apertures, we can write

$$\begin{aligned} A(x, y)_l &= \frac{\partial W(x, y)_l}{\partial x} = \sum_{i=2}^{I} k_i \frac{\partial Z_i(x, y)_l}{\partial x}, \\ B(x, y)_l &= \frac{\partial W(x, y)_l}{\partial y} = \sum_{i=2}^{I} k_i \frac{\partial Z_i(x, y)_l}{\partial y}. \end{aligned} \tag{2.15}$$

In matrix notation

$$\vec{M} = D\vec{K}. \tag{2.16}$$

where $\vec{M}$ is the vector of measurements, $\vec{K}$ the vector of mode coefficients and D is a matrix containing the derivatives of the basis functions:

$$D = \begin{pmatrix} \frac{\partial Z_2(x,y)_1}{\partial x} & \frac{\partial Z_3(x,y)_1}{\partial x} & \cdots & \frac{\partial Z_I(x,y)_1}{\partial x} \\ \frac{\partial Z_2(x,y)_2}{\partial x} & \frac{\partial Z_3(x,y)_2}{\partial x} & \cdots & \frac{\partial Z_I(x,y)_2}{\partial x} \\ \vdots & \vdots & & \vdots \\ \frac{\partial Z_2(x,y)_L}{\partial x} & \frac{\partial Z_3(x,y)_L}{\partial x} & \cdots & \frac{\partial Z_I(x,y)_L}{\partial x} \\ \frac{\partial Z_2(x,y)_1}{\partial y} & \frac{\partial Z_3(x,y)_1}{\partial y} & \cdots & \frac{\partial Z_I(x,y)_1}{\partial y} \\ \vdots & \vdots & & \vdots \\ \frac{\partial Z_2(x,y)_L}{\partial y} & \frac{\partial Z_3(x,y)_L}{\partial y} & \cdots & \frac{\partial Z_I(x,y)_L}{\partial y} \end{pmatrix}. \tag{2.17}$$

If D is a square matrix of full rank the solution to Eq. (2.16) is given simply by multiplying $\vec{M}$ with the inverse of D:

$$\hat{K} = D^{-1}\vec{M} \; . \tag{2.18}$$

In this case, $\hat{K}$ is an exact solution to Eq. (2.16). Usually, however, the number of Zernike modes taken into account is smaller than the number of measurement points, and the linear system of equations corresponding to Eq. (2.16) is over-determined. The criterion for finding $\hat{K}$ to minimize the squared error between the measurement and the estimate then leads to the normal equation (cf. [Bronstein et al. 1995]):

$$\left(D^T D\right)\vec{K} = D^T \vec{M} \; . \tag{2.19}$$

The solution $\hat{K}$ to this equation minimizes the Euclidian norm $\left\|D\vec{K} - \vec{M}\right\|_2$ in the least-squares sense and is given by

$$\hat{K} = \left(D^T D\right)^{-1} D^T \vec{M} = A^{+}\vec{M} \; . \tag{2.20}$$

(The matrix D has full rank and thus $D^T D$ is regular and invertible). The matrix A^+ in Eq. (2.20) is referred to as pseudo-inverse of D [Golub and Van Loan 1983]. In general it can be calculated via singular value decomposition (SVD) [Golub and Van Loan 1983]. If $\hat{K}$ has been determined, the reconstruction process is completed. The estimation of the original wave-front $\hat{W}(x,y)$ is subsequently expressed with Eq. (2.14).

According to Southwell [Southwell 1980], the accompanying mean-square wave-front reconstruction error $s_{\hat{W}}^{2}$ for the solution Eq. (2.14) is given by

$$s_{\hat{W}}^{2} = s_{g}^{2} \cdot tr\left\{\left(D^{T} D\right)^{-1}\right\} \tag{2.21}$$

where s_g^2 is the mean-square error of the slope measurements of the measurement vector $\vec{M}$. The mean-square error in such slope measurements can be assumed to be the same for all elements [Dai 1996]. In Eq. (2.21) *tr{ }* denotes the trace of a matrix.

2.2.2 Phase Shifting Interferometry

As mentioned in chapter 1 the resolution and efficiency of multi-quantum-fluorescence microscopy are to a great extent affected by wave-front aberrations. In order to counteract those aberrations by pre-emptive distortion of the incoming wave-front it is necessary to know the correction to apply. To obtain this knowledge the fraction of light that comes from the focal region needs to be selected exclusively. Conventional microscopy lacks the ability to discriminate light that comes from the focal region against out-of-focus light. Different from this, interferometry can distinguish between out-of-focus light and light that does come from the focal region (cf. section 2.4). The interferometric detection technique that is used in this dissertation, phase shifting interferometry (PSI) [Carré 1966], [Crane 1969], is described in this subsection.

The basic concept of PSI is to introduce a varying phase shift between the reference wave-front and the wave-front to be measured. At each measurement point in the interferogram a signal results, which varies depending on this phase shift and contains the information about the relative phase between the two wave-fronts. Using monochromatic light, the electrical fields for the reference wave-front and AWF can be expressed as

$$\begin{gathered} E_{ref}(x,y,t) = A_{ref}(x,y,t)\,e^{i\left[f_{ref}(x,y)-d\right]} \\ \text{and} \\ E_{aberr}(x,y,t) = A_{aberr}(x,y,t)\,e^{i f_{aber}(x,y)}, \end{gathered} \tag{2.22}$$

with amplitudes $A_{ref}(x,y,t)$ and $A_{aberr}(x,y,t)$, the wave-front phases $f_{ref}(x,y)$ and $f_{aberr}(x,y)$ and the imposed additional phase shift d. The phase shift d can be introduced, for example, by varying the length of either of the interferometer's arms. The interferometrical intensity pattern measured at the detector is given by the square of the sum of the fields in Eqs. (2.22)

$$
\begin{aligned}
I(x,y,t) &= \left|E_{ref}(x,y,t)+E_{aberr}(x,y,t)\right|^2 \\
&= A_{ref}^2(x,y,t)+A_{aberr}^2(x,y,t) \\
&\quad +2A_{ref}(x,y,t)\cdot A_{aberr}(x,y,t)\cdot\cos\left[f_{ref}(x,y)-f_{aberr}(x,y)+d\right].
\end{aligned}
\tag{2.23}
$$

This can be rewritten as the fundamental equation for PSI [Malacara 1992]:

$$
I(x,y,t)=I_{ampl.}(x,y)+I_{interf.}(x,y)\cdot\cos[f(x,y)+d], \tag{2.24}
$$

where $I_{ampl.}(x,y)\propto\int A_{ref}^2(x,y,t)+A_{aberr}^2(x,y,t)dt$ is the average intensity, $I_{interf.}(x,y)\propto\int 2\cdot A_{ref}(x,y,t)\cdot A_{aberr}(x,y,t)dt$ is the intensity modulation and $f(x,y)=f_{aberr}(x,y)-f_{ref}(x,y)$ is the wave-front phase difference. At each point the intensity varies as a sinusoidal function of the introduced phase shift $\boldsymbol{d}$ with an offset given by the unknown wave-front phase (Figure 2.8).

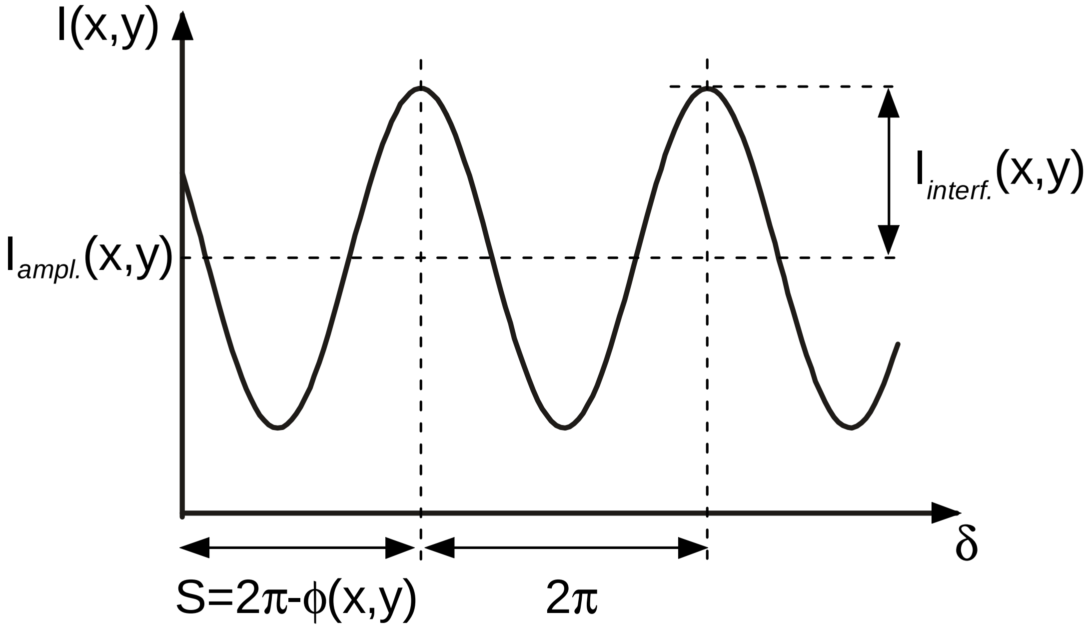

Figure 2.8: The intensity variation in an interferogram as function of the phase shift d(t) in one of the interferometer arms.

The three unknown variables of Eq. (2.24) are illustrated in Figure 2.8, where $I_{ampl.}(x,y)$ is the intensity bias, $I_{interf.}(x,y)$ is half the peak-to-valley intensity modulation and $f(x,y)$ is the unknown relative phase to be measured. From the shift S of the sinusoidal variation the unknown relative wave-front phase can be computed. Using an interferogram as depicted in Figure 2.8 for all positions *(x,y)* the entire relative wave-front phase *f(x,y)* can be measured and reconstructed.

One method to implement PSI is the *four-step algorithm* [Malacara 1992]. Four separate interferograms, each with δ increasing in steps of ${}^{\pi}/_{2}$

$$d_i = 0, \frac{p}{2}, p, \frac{3p}{2}; \qquad i = 1,2,3,4 \tag{2.25}$$

are recorded and digitized. Substituting each of the values in Eq. (2.25) into Eq. (2.24) results in four equations describing the expected intensity patterns:

$$\begin{aligned} I_1(x,y) &= I_{ampl.}(x,y) + I_{interf.}(x,y)\cos[f(x,y)] \\ I_2(x,y) &= I_{ampl.}(x,y) + I_{interf.}(x,y)\cos\left[f(x,y) + \frac{p}{2}\right] \\ I_3(x,y) &= I_{ampl.}(x,y) + I_{interf.}(x,y)\cos[f(x,y) + p] \\ I_4(x,y) &= I_{ampl.}(x,y) + I_{interf.}(x,y)\cos\left[f(x,y) + \frac{3p}{2}\right]. \end{aligned} \tag{2.26}$$

Using the trigonometric identities *cos(x+*${}^{p}/_{2}$*) = -sin(x), cos(x+p) = -cos(x)* and *cos(x+*${}^{3p}/_{2}$*) = sin(x),* we find

$$\begin{aligned} I_1(x,y) &= I_{ampl.}(x,y) + I_{interf.}(x,y)\cos[f(x,y)] \\ I_2(x,y) &= I_{ampl.}(x,y) - I_{interf.}(x,y)\sin[f(x,y)] \\ I_3(x,y) &= I_{ampl.}(x,y) - I_{interf.}(x,y)\cos[f(x,y)] \\ I_4(x,y) &= I_{ampl.}(x,y) + I_{interf.}(x,y)\sin[f(x,y)]. \end{aligned} \tag{2.27}$$

We then eliminate the intensity bias term $I_{ampl.}(x,y)$ and get:

$$\begin{aligned} I_4(x,y) - I_2(x,y) &= 2I_{interf.}(x,y)\sin[f(x,y)] \\ I_1(x,y) - I_3(x,y) &= 2I_{interf.}(x,y)\cos[f(x,y)]. \end{aligned} \tag{2.28}$$

In principle, Eqs. (2.28) allow the direct calculation of the AWF's phase. One possible way to obtain the actual wave-front is to use the notoriously unstable and noise-sensitive process of phase unwrapping. A different method is used in this dissertation (described in subsection 2.4.3).

In addition to providing phase information that can be used in various ways to reconstruct the wave-front, PSI allows coherence gating if illumination light of sufficiently short coherence length is used since any light that does not cause an intensity variation with *d* will be rejected by applying Eqs. (2.28). If continuous waves are used, no depth-discrimination is possible, because all the light is coherent, and interference can be observed at all points in time. In order to obtain sufficient temporal discrimination femtosecond light pulses need to be used. Then, in Eqs. (2.23) to (2.28) an additional factor in front of $I_{interf.}(x,y)$, the complex degree of coherence, has to be added [Goodman 2000], which is equal to 1 as long as continuous waves are used. The actual value of the complex degree of coherence depends on the spectral properties of the light source used and can be, if the power spectral density of the source has a Gaussian shape, described as ([Goodman 2000])

$$\exp\left[-\left(\frac{p\ \Delta n\ \Delta t}{2\sqrt{\ln 2}}\right)^2\right]. \tag{2.29}$$

In this equation $\Delta\nu$ is the FWHM of the power spectral density. The transit time difference between the two interferometer arms due to their path length difference *Ds(x,y)* is Dt =*Ds/c* (c is the speed of light). As can be seen, the value of the envelope in Eq. (2.29) depends on the arm length mismatch in the interferometer. Thus, when using femtosecond light pulses the rejection of incoherent light is of significance, because if Eqs. (2.28) are applied a signal results only if the arm length mismatch is less than or equal to the coherence length of the light source. To make this clearer the phase in Eqs. (2.28) as well as Dt in Eq. (2.29) are expressed as a function of the interferometer's arm length mismatch *Ds(x,y)*. The discrete phase shifts of *d* become spatial shifts of $^{\lambda}/_4$, $^{2\lambda}/_4$ and $^{3\lambda}/_4$, respectively. Accordingly the proportionalities in Eqs. (2.28) can be expressed as follows

$$\begin{aligned}
I_4(x,y)-I_2(x,y) &\propto e^{-a\left[\Delta s(x,y)+\frac{3l}{4}\right]^2}\cos\left\{\tfrac{2p}{l}\left[\Delta s(x,y)+\tfrac{3l}{4}\right]\right\}- \\
&\qquad e^{-a\left[\Delta s(x,y)+\frac{l}{4}\right]^2}\cos\left\{\tfrac{2p}{l}\left[\Delta s(x,y)+\tfrac{l}{4}\right]\right\} \\
I_1(x,y)-I_3(x,y) &\propto e^{-a[\Delta s(x,y)]^2}\cos\left\{\tfrac{2p}{l}\Delta s(x,y)\right\}- \\
&\qquad e^{-a\left[\Delta s(x,y)+\frac{2l}{4}\right]^2}\cos\left\{\tfrac{2p}{l}\left[\Delta s(x,y)+\tfrac{2l}{4}\right]\right\}.
\end{aligned} \tag{2.30}$$

Here, *a* is equal to $1/(2\sigma^2)$ with σ being the width of the Gaussian function. We now make the assumption that the exponential function varies only little over one wavelength. This is known as the slowly varying envelope approximation. In this case, the phase steps used to implement the PSI algorithm do not change the exponential function in Eqs. (2.30) significantly. Eqs. (2.30) can then, using again the trigonometric identities *cos(x+*$^{p}/_{2}$*) = -sin(x)*, *cos(x+p) = -cos(x)* and *cos(x+*$^{3p}/_{2}$*) = sin(x)* be combined to

$$\begin{aligned} I_4(x,y) - I_2(x,y) &\propto e^{-a\Delta s(x,y)^2} \sin[\Delta s(x,y)] \\ I_1(x,y) - I_3(x,y) &\propto e^{-a\Delta s(x,y)^2} \cos[\Delta s(x,y)]. \end{aligned} \tag{2.31}$$

The sum of the square of each of the Eqs. (2.31) will be a Gaussian:

$$\begin{aligned} &[I_4(x,y) - I_2(x,y)]^2 + [I_1(x,y) - I_3(x,y)]^2 \\ &\propto e^{-2a\Delta s(x,y)^2} \left(\sin^2[\Delta s(x,y)] + \cos^2[\Delta s(x,y)]\right) \\ &= \exp\left[-2a\Delta s(x,y)^2\right]. \end{aligned} \tag{2.32}$$

Since the parameter *a* is proportional to *Dn* (cf. Eqs. (2.29) and (2.30)) and the coherence length l_{coh} is proportional to 1/ *Dn* [Hecht 1990] the algorithm depicted in Eq. (2.32) results in a reasonable signal only if *Ds(x,y)* is less than or equal to the coherence length l_{coh} (the maximum signal results at *Ds(x,y)=0*). If *Ds(x,y)* becomes larger than l_{coh}, the signal rapidly falls off and light with the wrong path length is rejected accordingly. This results in depth resolution on the order of the coherence length.

2.3 Mie Theory

The aim of this work is to demonstrate the feasibility of measuring wave-fronts from light that stems from within scattering samples. For testing CGWS such samples were produced by embedding polystyrene beads in agarose (cf. subsection 3.2.1). The properties of these samples were determined using Mie's theory, which is briefly summarized in the following.

2.3.1 Scattering Properties in Detail

It was in 1908 when Gustav Mie obtained, on the basis of electromagnetic theory, a rigorous solution for the diffraction of a plane monochromatic wave by a sphere of arbitrary diameter and composition but of a homogeneous refractive index embedded in a homogeneous medium [Mie 1908]. A derivation of Mie's formulae is given in [Born and Wolf 1999]. In general the intensity and polarization of the scattered light can be described as (see [Born and Wolf 1999])

$$\begin{aligned} I^{\text{scattered}}_{\text{parallel}} &= \frac{l^{(I)2}}{4p^2 r^2}\left|\sum_{l=1}^{\infty}(-i)^l\left[{}^eB_l P_l^{(1)'}(\cos q)\sin q - {}^mB_l\,\frac{P_l^{(1)}(\cos q)}{\sin q}\right]\right|^2 \\ I^{\text{scattered}}_{\text{perpendicular}} &= \frac{l^{(I)2}}{4p^2 r^2}\left|\sum_{l=1}^{\infty}(-i)^l\left[{}^eB_l\,\frac{P_l^{(1)}(\cos q)}{\sin q} - {}^mB_l P_l^{(1)'}(\cos q)\sin q\right]\right|^2 . \end{aligned} \tag{2.33}$$

Here, $l^{(I)}$ is the wavelength in the medium surrounding the sphere. The incoming beam, the scattering particle and the position of observation determine a plane called the scattering plane. Eqs. (2.33) represent the parallel and perpendicular components of the scattered light with respect to this plane (cf. Figure 2.9). The curvilinear coordinates used are the spherical polar coordinates, r, q and f

$$\begin{aligned} x &= r\sin q\cos f \\ y &= r\sin q\sin f \\ z &= r\cos q . \end{aligned} \tag{2.34}$$

The polynomials in *cos q* in Eqs. (2.33) without a superscript are Legendre polynomials, those with a superscript are the Legendre functions of the first kind:

$$\begin{aligned} P_l(\cos q) &= \sum_{m=0}^{l/2}(-1)^m\,\frac{(2l-2m)!}{2^l\,m!(l-m)!(l-2m)!}(\cos q)^{l-2m} \\ P_l^{(m)}(\cos q) &= (\sin q)^m\,\frac{d^m P_l(\cos q)}{d(\cos q)^m}. \end{aligned} \tag{2.35}$$

The complex coefficients ${}^eB_l$ and ${}^mB_l$ in Eqs. (2.33) are represented by

$$\begin{aligned} {}^eB_l &= i^{l+1}\,\frac{2l+1}{l(l+1)}\,\frac{\hat{n}\Psi_l'(q)\Psi_l(\hat{n}q)-\Psi_l(q)\Psi_l'(\hat{n}q)}{\hat{n}z_l^{(1)'}(q)\Psi_l(\hat{n}q)-z_l^{(1)}(q)\Psi_l'(\hat{n}q)} \\ {}^mB_l &= i^{l+1}\,\frac{2l+1}{l(l+1)}\,\frac{\hat{n}\Psi_l(q)\Psi_l'(\hat{n}q)-\Psi_l'(q)\Psi_l(\hat{n}q)}{\hat{n}z_l^{(1)}(q)\Psi_l'(\hat{n}q)-z_l^{(1)'}(q)\Psi_l(\hat{n}q)}, \end{aligned} \tag{2.36}$$

where the prime indicates the differentiation of the function with respect to its argument, $\hat{n}$ is the complex index of refraction and q is the dimensionless parameter bound with the radius a of the scattering sphere.

The parameters $\hat{n}$ and a are given by

$$\hat{n} = \frac{n^{(II)}}{n^{(I)}} \quad \text{and} \quad q = \frac{2p}{l^{(I)}} a \, . \tag{2.37}$$

Here, the superscripts *(I)* and *(II)* denote the parameter in the medium surrounding the sphere *(I)* and the parameter in the sphere *(II)*.

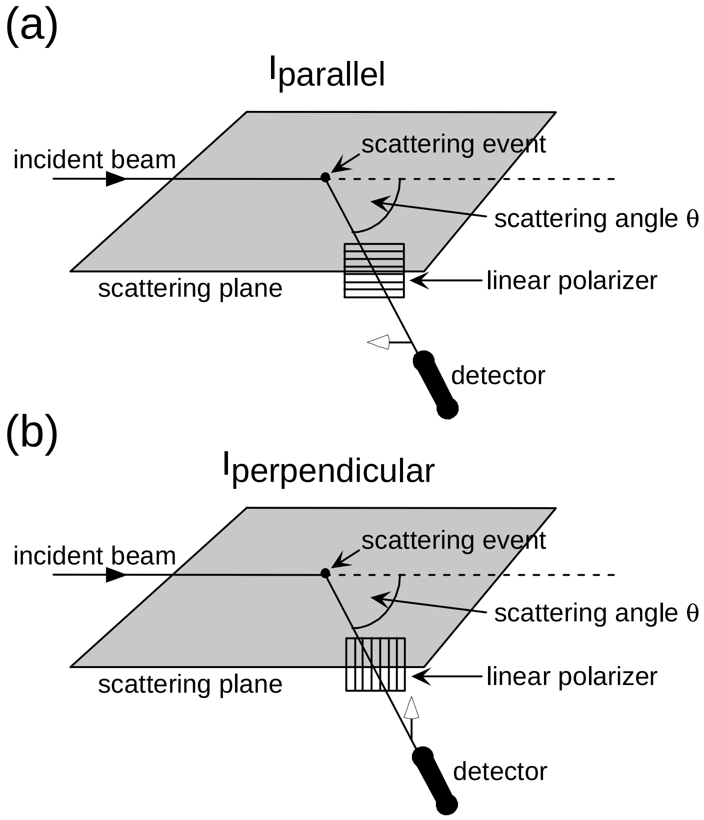

Figure 2.9: The geometry for the description of Mie scattering.

For the first term of Eqs. (2.37) it was assumed that the medium and the sphere are non-absorbing. Ψ and z in Eqs. (2.36) use the Bessel functions $J_{l+1/2}$ and the Hankel functions, which are given by a combination of Bessel and Neumann $(N_{l+1/2})$ functions (for further details see [Born and Wolf 1999]):

$$\Psi_l(r) = \sqrt{\frac{pr}{2}}\, J_{l+\frac{1}{2}}(r)$$

and (2.38)

$$z_l^{(1)}(r) = \Psi_l(r) + i\sqrt{\frac{pr}{2}}\, N_{l+\frac{1}{2}}(r) \equiv \sqrt{\frac{pr}{2}}\, H_{l+\frac{1}{2}}^{(1)}(r).$$

It is of practical interest to find the total amount of light that is absorbed or scattered by the sphere, i.e. the sum of the absorbed and the scattered energy. This can be done by using the optical cross-section theorem [Born and Wolf 1999]. For a non-absorbing sphere the sum of absorbed and scattered energy is equal to the extinction cross-section (cf. [Born and Wolf 1999]):

$$Q = \frac{l^{(I)2}}{2p}\,\mathrm{Re}\left(\sum_{l=1}^{\infty} (-i)^{l+1} l(l+1)\left({}^{e}B_l + {}^{m}B_l\right)\right). \tag{2.39}$$

That means that the MFP for a medium consisting of non-absorbing spheres can be calculated applying Eq. (2.39). Taking into account that the MFP is given by the inverse of the product of concentration of scattering particles *n* and scattering cross-section, we can write

$$MFP = \frac{1}{nQ}\,. \tag{2.40}$$

Another feature of the scattering process that is important for CGWS is the anisotropy, *g*, which is a measure of the amount of conserved forward direction after a single scattering event. If the trajectory of light scattered by a particle is deflected by an angle *q*, then the component of the new trajectory that is in the forward direction, is proportional to the cosine of *q* (cf. Figure 2.10). The anisotropy g is defined as the average cosine of the deflection angle *q*

$$g = \int_0^{p} p(q)\cos q \cdot 2p \sin q \, dq = \left\langle \cos q \right\rangle, \tag{2.41}$$

with *p(q)* being the probability of light scattering into a unit solid angle oriented at an angle *q*. This probability has also been called scattering phase function. To simplify matters the special case of azimuthally symmetric scattering is assumed. If the incident light is unpolarized, the total amount of scattered light intensity for a scattering angle q can be expressed as [Bohren and Huffman 1998]

$$I_{\text{total}}^{\text{scattered}}(q) = \frac{1}{2} \cdot I_{\text{parallel}}^{\text{scattered}}(q) + \frac{1}{2} \cdot I_{\text{perpendicular}}^{\text{scattered}}(q) \tag{2.42}$$

and the anisotropy can be calculated as follows:

$$g = \frac{\int_0^p I_{\text{total}}^{\text{scattered}}(q) \cos(q) 2p \sin(q) dq}{\int_0^p I_{\text{total}}^{\text{scattered}}(q) \cdot 2p \sin(q) dq}. \tag{2.43}$$

Thus, Eqs. (2.33), Eq. (2.40) and Eq. (2.43) allow the determination of the main scattering properties of a scattering sample.

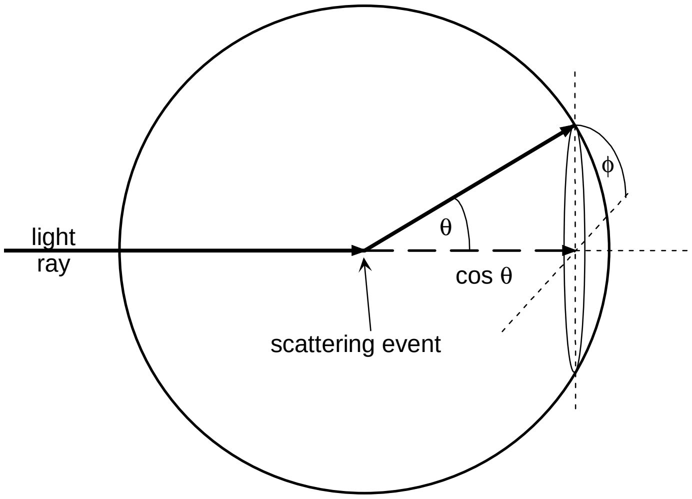

Figure 2.10: A scattering event causes a deflection q of the original light ray. The azimuthal scattering angle f, which is also present is of no importance for the conserved forward direction of the light, which is solely governed by cos q.

2.4 Coherence-Gated Wave-Front Sensing

As mentioned in preceding chapters, it is desirable to be able to correct the focus by pre-emptive distortions of the incident wave-front. The knowledge of their required form is a necessary condition to achieve these distortions. For a certain point at a certain depth in a scattering sample this means that the shape of the wave-front, which is formed by light that is backscattered from exactly this point needs to be known, because this light encounters the same sample inhomogeneities as the incoming light on its way to the focus. In the previous section the underlying principles that can be used to obtain this information were described.

In this section their combination to CGWS [Feierabend et al. 2004] is described. Subsection 2.4.1 deals with the light source - a femtosecond mode-locked laser - that provides one of the necessary parts for coherence-gating, namely low-coherent light. Subsection 2.4.2 describes the main features of the CCD camera that is used to record the interferograms. The setup used to demonstrate CGWS is the topic of subsection 2.4.3. The implementation of the PSI algorithm is described in detail in subsection 2.4.4. Finally an optimization process to compensate the group velocity dispersion (GVD), which is used to minimize the size of the coherence gate (CG) for a given coherence length is explained in subsection 2.4.5.

2.4.1 The Light Source

Since low-coherence light is required for the coherence-gating process the light source was chosen to be a Titanium Sapphire Oscillator (Coherent Model Mira 900-F). This laser provides low-coherent light in the form of femtosecond mode-locked laser pulses. The population inversion in the gain medium is achieved by using a frequency doubled Neodymium Vanadate (Nd:YVO_4) laser (Coherent Model Verdi^{TM} V-5) as a pump source. It provides single-frequency continuous-wave (green, 532nm) light output of 5 Watts. In order to obtain the short light pulses the Mira is Kerr lens mode-locked [Spence et al. 1991]. The optical cavity design leads to a higher round trip gain in the mode-locked versus continuous wave operation mode. This is because the spatial profile of the beam changes as a consequence of self-focusing due to the optical Kerr effect in the gain medium. As a result, the overlap between the pumped gain profile and the circulating cavity mode increases. To enhance this effect, an aperture is placed at a corresponding position within the cavity, which results in lower round trip loss in the mode-locked operation mode. Table 2.2 summarizes the Mira specifications.

The pulse length is about 100 femtoseconds (fs). Assuming a flat phase profile of the pulse, its temporal width can be calculated from a measured spectrum (e.g. Figure 2.11) via the time bandwidth product $t\ Dn = 0.44$ [Siegman 1986]. The outcome is referred to as Fourier limited pulse width [Siegman 1986]. From a value for the pulse width of about 100 fs the corresponding coherence length will be 30 μm. The CG depends only on this length (cf. subsection 2.2.2).

Table 2.2: Specifications of the used laser setup

Used Mira 900 configuration specifications	
Pump laser	Verdi V5
Pump power	5 Watts
Tuning range (XW optics set)	730 – 980 nm
Center Wavelength	915 nm
Average power	375 mW
Pulse width	≈ 100 fs
Repetition rate	76 MHz
Theoretical peak power	≈ 50 kW (calculated from measured average power, repetition rate and minimal pulse width)

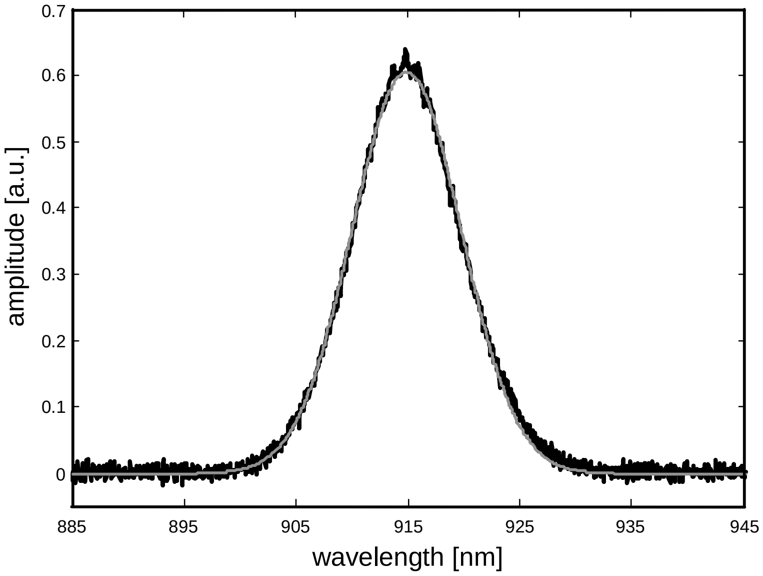

Figure 2.11: Example for the measured spectrum emerging from the Mira. The measurements are presented in black. The gray line represents a Gaussian fit, which gives a slightly higher squared regression coefficient (R^2) than a $sech^2$-fit. The measure for determining the pulse length is the width of this curve. The full width at half maximum (FWHM) is, in this case, 11.5 nm corresponding to a Fourier limited pulse of 107 fs assuming a Gaussian pulse shape.

2.4.2 The CCD Camera

A crucial part of CGWS is the detection of the light. As described in subsection 2.4.3 a PSI algorithm was used to detect the wave-front. While use of interferometric detection relaxes the requirement for low dark noise, linearity and quantum efficiency of the detector are still important. A monochrome CCD camera was therefore used (Sony Corporation, USA), controlled by a Hamamatsu (Hamamatsu, USA) C2400-60 control unit. Via a Matrox (Matrox Germany Electronic Systems GmbH) Meteor II frame grabber card the video signal of the camera was digitized for further processing on a personal computer.

Some of the properties of the camera used were carefully determined independently of the manufacturers specifications.

In order to automate the phase-stepping of the PSI algorithm used (cf. subsection 2.4.3), changing the reference arm path length needed to be synchronized with the frameclock of the camera. Therefore, the operation of the camera used was examined first. The Sony XC-77 CCD camera module produces video signal output that corresponds to the RS-170 (EIA standard) signal system. The RS-170 standard is an interlaced-working standard. That means, that in the case of classical video cameras after 63.56 µs the scanning process of the first odd row is finished and starts at the next odd row. This scanning and starting in the next row is repeated until all odd rows are scanned and the odd half-frame is completed. After 16.68 ms this is accomplished and a vertical-sync signal can initiate the next half-frame, the one for the even rows. Taking this operation principle into account, the half-frames are scanned with a frequency of 60 Hz. Obviously, in CCD camera devices there is no beam scanning, as the readout process replaces this function. However the frequency at which the half-frames are delivered remains 60 Hz. The organization of the Sony XC-77 follows an interline-transfer scheme (Figure 2.12). Light variations are sensed by the photo sensors, which generate electronic charges proportional to the incident light intensity. The generated charges are fed into the vertical shift registers simultaneously. Then they are transferred from the vertical shift registers to the horizontal shift registers successively and, finally they reach the output amplifier to be read out sequentially.

During the readout process light still falls onto the photo sensors. This light will be integrated. The corresponding time course can be summarized as:

1. Light falls onto both, the even and the odd lines.
2. The generated charges of the odd lines are read out while the light, which is still falling onto the even lines is further summed up.
3. As soon as the charges of the odd lines are transferred to the vertical shift registers, the integration of incoming light on them starts again, e.g. if line three is read out, the integration process for line one has already started again and so on.
4. Then the charges generated on the even lines will be read out. During this process the light falling onto the odd lines is integrated.

As soon as the charges of the even lines are transferred to the vertical shift registers, the summing up of incoming light on the even lines starts again. This means, that the integration time for one half-frame is equal to the inverse frequency at which the frames are delivered, 33.36 ms. Consequentially, in a complete frame there is the time information of three half-frames (Figure 2.13).

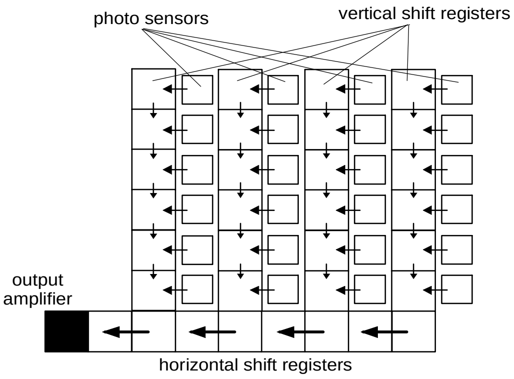

Figure 2.12: Interline transfer organization of the XC-77 CCD camera module.

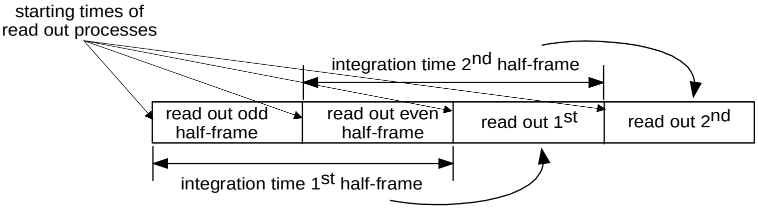

Figure 2.13: Schematic operation principle of the Sony CCD camera module. The full frame of interest consists of first and second half-frames. The integration process for each half-frame starts immediately after the start of the corresponding readout process, which runs quasi in parallel. The result is a time contents of three half-frames in a full frame.

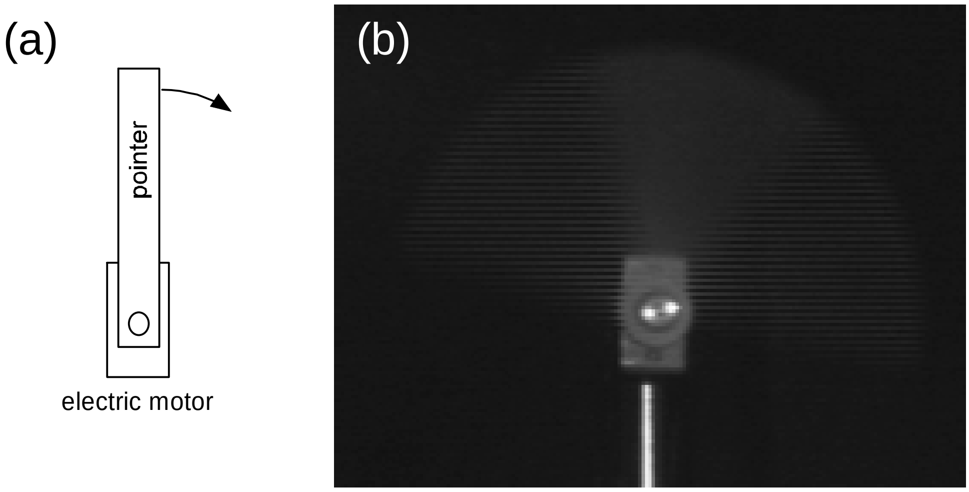

Figure 2.14: The time information contents of a full frame in practice. If a cardboard pointer rotating at a constant speed (a) is recorded with a CCD camera, the full frame clearly visualizes the three integration time phases (b). The rotation of the pointer leads to an image of a half circle, the 'pointer half circle'. First the lines of the first half-frame, the odd lines, are integrated. Evidently in (b) in the left part of the 'pointer half circle' only every other line contains light information. However there is a time period where the light falling on both odd and even lines is integrated. Correspondingly the middle sixth of the 'pointer half circle' in (b) shows no alternating behavior. Every line contains light information. Finally, only lines of the second half-frame are integrated. Unmistakably the right part of the 'pointer half circle' reveals again the alternating behavior. Thus a full frame contains time information of three half-frames.

To illustrate this, an experiment with a cardboard pointer, rotating at a constant speed, was performed. The rotation velocity was approximately half a rotation per camera frame. If the movement of the pointer was recorded with the CCD camera, a half circle became visible (Figure 2.14).

To be able to calculate the absolute intensity of the measured signals it is necessary to know how the number of photons incident on the photo-sensors of the CCD chip are converted into a value of analogue digital units (ADUs) or ‘gray values’, respectively. The camera system (consisting of controller, camera and frame grabber) does this conversion with a dynamic range of 8 bits. The underlying conversion factor was determined as follows below. When the arrival of photons can be regarded as the independent occurrences of a sequence of random events at a rate equal to the photon flux, photons will obey the Poisson statistics [Saleh and Teich 1991]. Then the corresponding variance, σ^2, and standard deviation, σ, of their number N is given by [Taylor 1997]

$$\begin{aligned} \sigma^2 &\equiv \left\langle \left(N-\langle N\rangle\right)^2 \right\rangle \overset{\textit{Poisson statistics}}{=} \langle N\rangle \\ \sigma &\equiv \sqrt{\langle N\rangle}\,. \end{aligned} \tag{2.44}$$

To show that the conversion factor is a constant, images at 18 different incident light power levels were taken. For each power level fifty images (with a size of 640×480 pixels) were averaged and the integral of gray values was plotted versus the corresponding power level (Figure 2.15). If the conversion factor is really a constant, the integral of gray values should increase linearly with incident light power. The straight line in Figure 2.15 is a fit to the measured data points, which has an R^2-value of 0.99. Under the assumption that the gray value ‘M’ is proportional to the number of incident photons N the conversion factor α can be calculated starting from

$$M = \alpha\, N\,. \tag{2.45}$$

An equivalent transformation under inclusion of Eq. (2.44) gives

$$\begin{aligned} \left\langle \left(M-\langle M\rangle\right)^2 \right\rangle &= \left\langle \left(\alpha\, N-\langle \alpha\, N\rangle\right)^2 \right\rangle = \left\langle \left(\alpha\, N-\alpha\langle N\rangle\right)^2 \right\rangle \\ &= \left\langle \left(\alpha\,\left(N-\langle N\rangle\right)\right)^2 \right\rangle = \alpha^2 \left\langle \left(N-\langle N\rangle\right)^2 \right\rangle \\ &= \alpha^2 \sigma^2 = \alpha^2 N = \alpha^2 \left\langle \frac{M}{\alpha} \right\rangle = \alpha \langle M\rangle \\ \Rightarrow\quad \alpha &= \frac{\left\langle \left(M-\langle M\rangle\right)^2 \right\rangle}{\langle M\rangle}\,. \end{aligned} \tag{2.46}$$

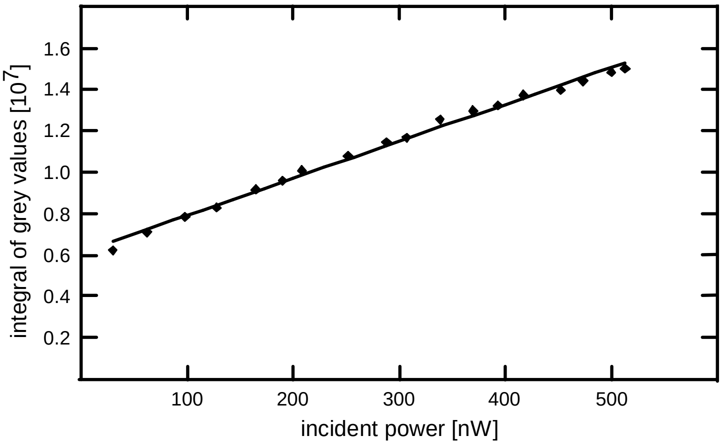

Figure 2.15: Measured response of the CCD chip to increasing power levels. As expected, the integral of gray values changes linearly with the incident power.

This shows that if the variance of gray values $\left\langle \left(M - \left\langle M \right\rangle\right)^2 \right\rangle$ is depicted as a function of the mean gray value $\left\langle M \right\rangle$, then according to Eq. (2.46) the slope is α. For a light emitting diode as the light source the photons obey Poisson statistics. The CCD chip was illuminated under a small angle with such a diode in order to provide a gradient of different gray values in each image. The mean and variance for each ADU were determined on the basis of 100 images. Subsequently the illumination strength of the diode was changed and another 100 images were taken to calculate again mean value and variance. This procedure was repeated fifteen times. The data points were background corrected which allows the comparison of the ordinate intersection with the otherwise measured dark noise. Each data pair (variance, mean gray value) was plotted, and a linear weighted fit was achieved (Figure 2.16). This linear fit yields a conversion factor of 0.00336, which means that the camera system translates ≈ 297 incident photons into one ADU.

To determine the black level and the dark noise of the camera, 10 times 100 images were taken while no light was falling onto the CCD chip. Each set of these 100 images was averaged and the produced ten mean values were again averaged. From the image generated in this way the black level was determined to 20.1626 ADUs and the dark noise to 0.7347 ADUs. While comparing the latter with the ordinate intersection (Figure 2.16), which should be its square value, a deviation of roughly 5% was found. That the black level is not equal to zero is due to the fact that the RS-170 standard introduces a small step on the blanking level [Inoué and Spring 1997].

In order to obtain an estimation of how efficiently the camera converts incident light, the power directly in front of the CCD chip was measured and compared to the number of photons that was calculated with the help of the conversion factor. An average of fifty images was taken, background corrected, and the integral of gray values was calculated. The energy per photon was ≈ $2.17 \cdot 10^{-19}$ Joule (915 nm wavelength). Hence, the measured power of $206 \cdot 10^{-9}$ W corresponds to $\approx 9.5 \cdot 10^{11}$ photons per second. The integral of gray values was $\approx 4.5 \cdot 10^{6}$. Since one ADU corresponds to 297 photons, this makes $\approx 1.34 \cdot 10^{9}$ photons per frame, i.e. per 33.36 ms, or $\approx 4 \cdot 10^{10}$ photons per second. This means that the camera efficiency is roughly 4%.

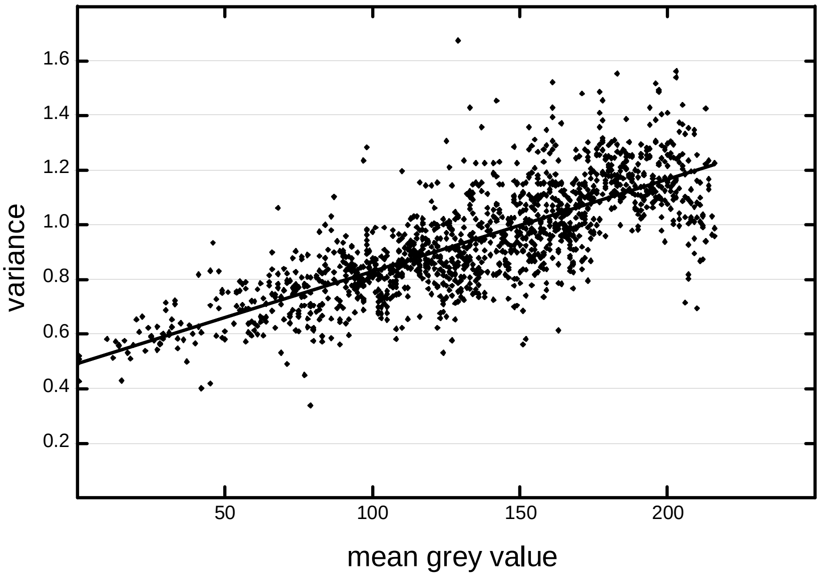

Figure 2.16: Variance plotted versus mean gray value. The slope of the linear fit line corresponds to the conversion factor, which was calculated to be 297 photons per ADU.

A specification for the fill factor of the XC-77 is not available. Typically for an interline-transfer CCD it lies between 25% and 70% (http://www.roperscientific.de/tinterline.html). This means that, if a fill factor of 70% is assumed, the quantum efficiency has to be 5.7%. On the other hand, if a fill factor of 30% is assumed, the quantum efficiency has to be 13.3%. Since the quantum efficiency for standard CCD video cameras at this wavelength is clearly under 10% (www.hamamatsu.de) it is more likely that the fill factor of the Sony XC-77 is in the vicinity of 70%.

As pointed out in section 2.2 the average slope of a wave-front across a sublens corresponds to the position of the diffraction spot in the focal plane of this sublens. To determine this position as accurately as possible, the size of a single pixel needs to be known. Therefore, the camera module was mounted on top of a linear stage and a standard Helium-Neon laser (Spindler & Hoyer HeNe-Laser 30) was aligned to shine its light orthogonally onto the CCD chip. To avoid that the camera got saturated, the beam was attenuated. Subsequently the camera was moved in small steps of 100 µm along a horizontal line perpendicular to the HeNe-laser beam. For every position of the camera the spot location of the laser on the CCD chip was determined by finding the spot centroid. Thus, the beam position on the camera was measured as a function of the distance covered by the camera.

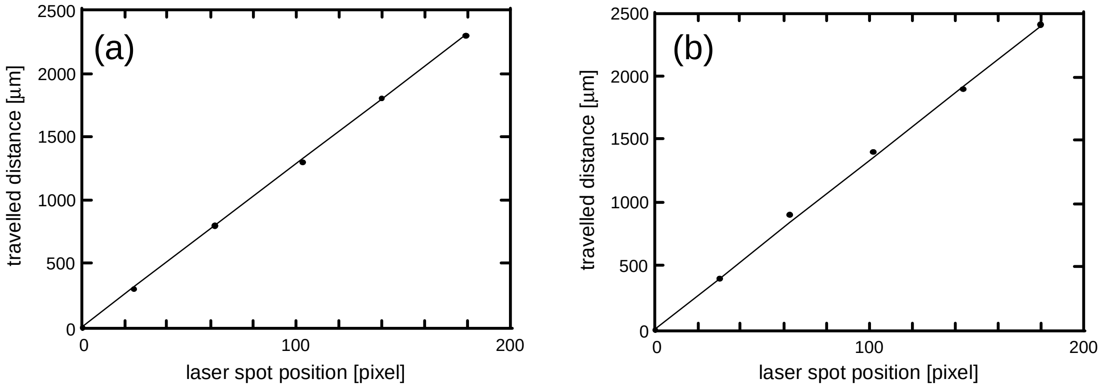

Figure 2.17: Distance covered by the camera as a function of laser beam spot position. For the long axis in (a), for the short axis in (b). The corresponding slopes are (12.85±0.07) mm per pixel and (13.25±0.22) mm per pixel, respectively.

If this is plotted as distance covered versus spot position in pixels (Figure 2.17) it becomes clear that

1. the data points should follow a straight line and
2. the slope of this line equals the pixel dimension along the horizontal orientation axis at the moment of measurement.

Similarly, the dimension for the perpendicular orientation was determined by rotating the camera by 90° (Figure 2.17). Short and long axis refers to the fact that the camera chip has a rectangular design. The images contain 640 pixels along the long axis and 480 pixels along the short axis. The individual pixel size was determined to be:

- Long side: (12.85±0.07) µm,
- Short side: (13.25±0.22) µm.

These results show that a single pixel is not square but rectangular – a fact that is important for the analysis of the diffraction spot shifts when measuring wave-fronts (cf. subsection 2.4.3).

2.4.3 Implementation of CGWS – The Setup

The basic idea of CGWS is to select exclusively the backscattered light from a small region within the sample and measure the accompanying wave-front. How this can be accomplished in practice is described in this subsection.

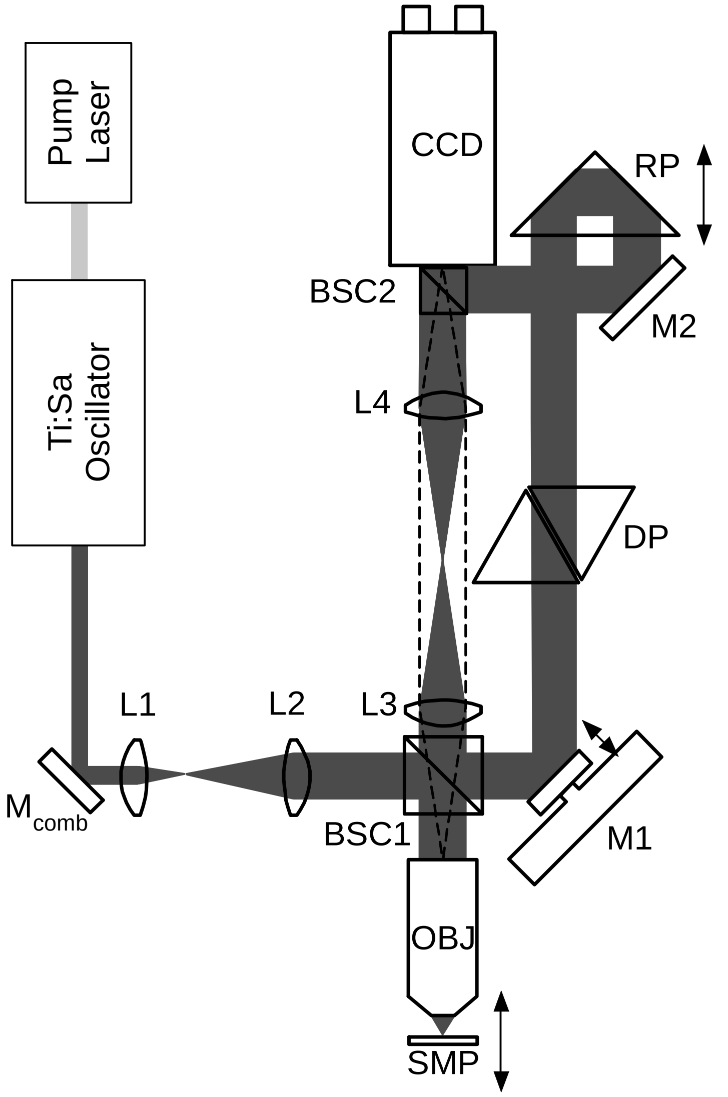

Figure 2.18: Schematic of the setup. A Neodymium Vanadate laser (Pump) pumps a Titanium Sapphire laser (Ti:Sa). This laser is tuned to produce modelocked laser pulses at a wavelength of 915 nm. The pulsed light is passed via a combination of several mirrors (M_{comb}, all LINOS Photonics) through a beam expander (L_1 and L_2; LINOS Photonics NIR doublets, f=40 mm and f=80 mm). A 50/50 beam splitter cube BSC1 (Coherent) splits the light into the reference and sample arms. In the sample arm the light is focused by an IR water immersion objective OBJ (Zeiss IR Achroplan 63x/0.9W) into the sample. A telescope consisting of lenses L3 and L4 (LINOS Photonics NIR doublets, f=140 mm) images the back focal plane (BFP) of the objective onto a CCD chip. The reference light is reflected from a mirror M1 (LINOS Photonics flat mirror, silver coated), which is mounted on a piezo ceramic (LINOS Photonics PCL100-40 controlled by LINOS Photonics Torque-Drive TD3-200). From there the light further propagates through dispersion matching prisms DP (LINOS Photonics BK7 prisms). The reference light is recombined with the backscattered light via a right-angle prism RP (LINOS Photonics), a mirror M2 (LINOS Photonics flat mirror, silver coated) and the beamsplitter cube BSC2 (LINOS Photonics).

Wave-front sensing is realized by the use of a PSI algorithm and virtual lenslets that mimic a SHS. This makes it possible to employ a modal estimation algorithm [Cubalchini 1979] for reconstructing the wave-front. The exclusive selection of backscattered light that comes from a certain depth within a sample is realized by means of a CG (cf. subsection 2.2.2). The phase shifts required for this algorithm are introduced by the controlled movement of a piezo ceramic translator (LINOS Photonics PCL 100-40). As mentioned in subsection 2.4.2 the light intensities are recorded via a monochrome CCD camera module and a frame grabber card for processing on a personal computer. The processing of the digitized data is performed by means of MATLAB (The MathWorks Inc.) routines.

As mentioned in subsection 2.2.2, PSI is achieved by using an interferometer setup. The setup is shown in Figure 2.18 and consists of two arms, i.e. the sample and the reference arm. Since the light source produces low-coherence light (cf. subsection 2.4.1), this interferometer can be used for depth discrimination as explained earlier (cf. subsection 2.2.2). The optical path length difference of the interferometer arms is adjusted by shifting the right-angle prism (RP, Figure 2.18). For small and deliberate changes the piezo ceramic can be used. Considering the statements of subsection 2.2.2, the interference signal on the CCD chip can be expressed as

$$\begin{gathered} I_D = i_r + i_s + 2\sqrt{i_r i_s}\, e^{-a\Delta t^2} \cos(j_s - j_r + d), \\ \text{where} \\ I_D = I_D(x,y,t), i_r = i_r(x,y,t), i_s = i_s(x,y,t) \\ j_s = j_s(x,y), j_r = j_r(x,y), d = d(t). \end{gathered} \tag{2.47}$$

For a given phase difference of the interferometer arms

$$f(x,y) = j_s(x,y) - j_r(x,y), \tag{2.48}$$

four small shifts of a quarter wavelength (915/4 nm) at a time make it possible to write Eqs. (2.26) as

$$\begin{aligned} I_4 - I_2 &= I_D(\text{position 4}) - I_D(\text{position 2}) = 4 i_r i_s e^{-a\Delta t^2} \sin(j_s - j_r) \\ I_1 - I_3 &= I_D(\text{position 1}) - I_D(\text{position 3}) = 4 i_r i_s e^{-a\Delta t^2} \cos(j_s - j_r) \end{aligned} \tag{2.49}$$

These four small shifts are produced by a corresponding movement of the piezo ceramic (cf. subsection 2.4.4). The movement of the piezo results in a decrease of the arm length of the reference arm and thus the intensities at the CCD chip for the four different positions are equal to

$$\begin{aligned}
I_1(x,y) &= I_{ampl.}(x,y) + I_{interf.}(x,y)\cos[f(x,y)] \\
I_2(x,y) &= I_{ampl.}(x,y) + I_{interf.}(x,y)\cos\left[f(x,y) - \frac{p}{2}\right] \\
I_3(x,y) &= I_{ampl.}(x,y) + I_{interf.}(x,y)\cos[f(x,y) - p] \\
I_4(x,y) &= I_{ampl.}(x,y) + I_{interf.}(x,y)\cos\left[f(x,y) - \frac{3p}{2}\right].
\end{aligned} \tag{2.50}$$

Using the trigonometric identities *cos(f-90°)=sin(f), cos(f-180°)=-cos(f)* and *cos(f-270°)=-sin(f)* yields

$$\begin{aligned}
I_1(x,y) &= I_{ampl.}(x,y) + I_{interf.}(x,y)\cos[f(x,y)] \\
I_2(x,y) &= I_{ampl.}(x,y) + I_{interf.}(x,y)\sin[f(x,y)] \\
I_3(x,y) &= I_{ampl.}(x,y) - I_{interf.}(x,y)\cos[f(x,y)] \\
I_4(x,y) &= I_{ampl.}(x,y) - I_{interf.}(x,y)\sin[f(x,y)].
\end{aligned} \tag{2.51}$$

Thus, we can write Eqs. (2.49) as

$$\begin{aligned}
I_4 - I_2 &= I_D(\text{position 4}) - I_D(\text{position 2}) = -4 i_r i_s e^{-a\Delta t^2} \sin(j_s - j_r) \\
I_1 - I_3 &= I_D(\text{position 1}) - I_D(\text{position 3}) = 4 i_r i_s e^{-a\Delta t^2} \cos(j_s - j_r).
\end{aligned} \tag{2.52}$$

Since *Dt* in the exponent of the exponential functions in Eqs. (2.52) equals the optical path length difference of the two interferometer arms divided by the speed of light (*Dx/c*$_0$*)*, the sum of the squares of each of the equations in Eqs. (2.52) can be written as

$$\begin{aligned}
(I_4 - I_2)^2 + (I_1 - I_3)^2 &= 16 i_r i_s e^{-\frac{2a\Delta x^2}{c_0^2}} \left(\sin^2[\Delta j] + \cos^2[\Delta j]\right) \\
&= 16 i_r i_s e^{-\frac{2a\Delta x^2}{c_0^2}}.
\end{aligned} \tag{2.53}$$

Therefore, changing *Dx* by moving the right-angle prism allows determining the position in which both arms have the same optical path length. For this particular position of the right-angle prism where *Dx=0*, the result of Eq. (2.53) becomes maximal. In practice, this length adjustment was achieved using a mirror in the focal plane of the objective. In scattering samples this length adjustment ensures that only light from the focal region contributes to the signal. The size of this region is governed by the coherence length of the light source used (cf. subsection 2.2.2). The middle position of this region is referred to as CG position. All incoherent light is rejected by making use of Eqs. (2.49). After the length adjustment procedure described, moving the scattering sample parallel to the OA determines the depth position in the sample from where backscattered light is detected.

Apart from its ability to adjust the arm lengths to the same optical path length, the algorithm in Eq. (2.53) also offers the option to check whether the setup is working correctly. From measurements of the FWHM of the power spectral density of the light source (cf. subsection 2.4.1), we can calculate a theoretical estimate for the FWHM of the envelope of Eq. (2.53) ($\mathrm{FWHM}_{\mathrm{env}}$). This can be compared to a real measurement. For this measurement a quartz plate that mimics a mirror was used as a sample. The reference arm length was changed in steps of ≈ 2 µm by moving the linear stage, on which the right-angle prism was mounted, in ≈ 1 µm steps. The error for the corresponding optical arm length change was assumed to be ±0.5 µm. This error was due to the inaccuracy in determining the division of the scale of the micrometer-screw that drives the linear stage. By moving the stage over a broad range and recording the signal at the CCD chip, the envelope of Eq. (2.53) is measured. Clearly, the dispersion present in both arms plays a significant role for the width of the resulting envelope. Therefore, dispersion matching prisms were introduced into the reference arm to adjust this dispersion (cf. subsection 2.4.5). If the FWHM of the frequency spectrum of the light source is known, and if the dispersion in both arms is identical, the exponential function term in Eq. (2.47) can be written as [Goodman 2000]

$$e^{-a\Delta t^2} \mathrel{\hat{=}} \exp\left[-\left(\frac{p \cdot \Delta n \cdot \Delta t}{2\sqrt{\ln 2}}\right)^2\right]. \tag{2.54}$$

Thus, the FWHM of the envelope $\exp\left(-\frac{2a\Delta x^2}{c_0^2}\right)$ of Eq. (2.53) can be expressed in terms of the frequency FWHM $\Delta\nu$ as:

$$FWHM_{env} = c_0\sqrt{\frac{2\ln 2}{a}} = \frac{2\sqrt{2}\ln(2)c_0}{p \cdot \Delta n}. \tag{2.55}$$

That means, that the frequency FWHM of the spectrum can be used to calculate the FWHM_{env}. In view of the fact that the spectrometer used measures the spectrum of a light source in the nanometer range, the required frequency FWHM is not directly available but can easily be calculated. In this wavelength range, it is possible to obtain a good approximation of the frequency FWHM by simply taking the difference between the frequency equivalents of the two wavelengths that mark the wavelength FWHM in the wavelength range. The resulting deviation from the actual value is only minor as will be seen later. In order to take the difference of the frequency equivalents, the abscissa is converted into corresponding frequency values via the relationship $n=c_0 /l$. Obviously the numerical distance of two adjacent frequencies becomes smaller and smaller the larger the wavelength. On the left hand side of this "new" x-axis the higher frequencies are situated whereas the lower ones are positioned on the right. In order to determine the FWHM for this new abscissa, i.e. for the spectrum expressed as a function of the frequency, it is necessary to draw the x-axis with the frequencies at equidistant spacing. Only this plot allows for a correct determination of the frequency FWHM. As a result of this redraw, an expansion effect at the lower frequency edge is produced, i.e. the gradient of the spectrum is smaller at lower frequencies compared to the higher frequency edge. The frequency FWHM determined in this plot of the spectrum is different from the frequency FWHM calculated by the corresponding frequency equivalents of the wavelength FWHM. In general, this becomes less important for higher wavelengths where the distance alteration between corresponding adjacent frequencies becomes negligible. In the case at hand, where wavelengths between 907 nm and 922 nm are observed (the measured wavelength FWHM was ≈ 14 nm, center wavelength 915 nm) the relative deviation between the two frequency FWHMs determined from the nanometer spectrum and from the frequency spectrum is only 3%. For the Mira spectrum, with a center frequency of $3.279\ 10^{14}$ Hz, the corresponding frequency FWHM was assumed to be $5.017\ 10^{12}$ Hz (derived from the nanometer spectrum). Applying Eq. (2.55) gives an expected FWHM_{env} of 37.3 μm. In practice the FWHM_{env} was determined with the help of a nonlinear least-squares fit. The MATLAB routine *nlinfit*, which uses the Gauss-Newton method, was applied for this purpose. A typical result, in this case for a wavelength FWHM of 14 nm, is shown in Figure 2.19, where the FWHM_{env} was 36.8 μm.

The FWHM_{env} corresponds to the achievable depth resolution since mainly the light from within a region of this size around the focus is detected (cf. subsection 2.2.2). For a coherence length of 30 μm the volume of this region amounts to roughly 6 picoliters. Of course, the objective is to keep this region as small as possible. The optimum is reached through compensation of second order dispersion (GVD) present in the sample arm. How this is done is described in detail in subsection 2.4.5.

Wave-front sensing is implemented by using PSI and virtual lenslets. These virtual lenslets are obtained by dividing the sensing area of the CCD chip into small compartments (from now on called virtual lenslet compartments, VLC) with a size of 15×15 pixels each.

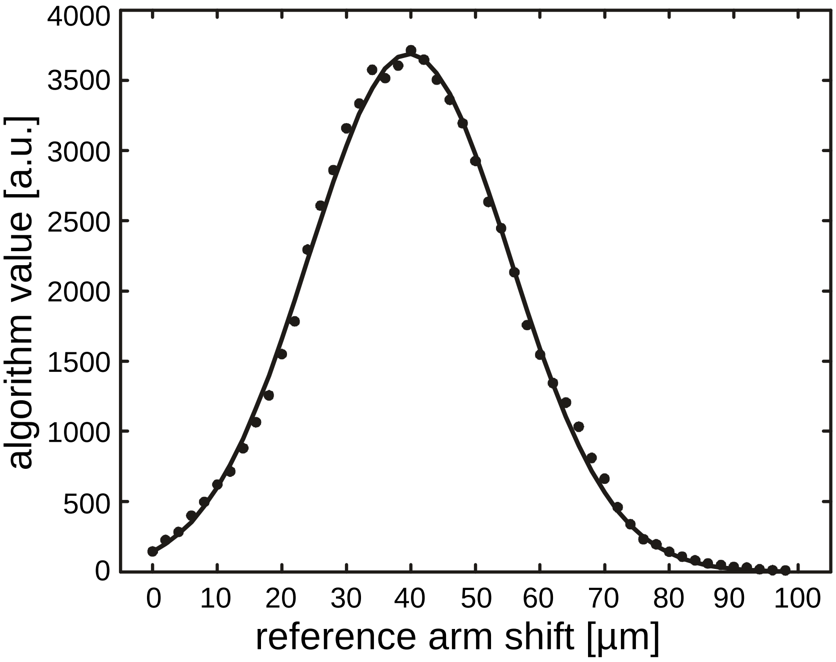

Figure 2.19: Envelope of Eq. (2.53) for a pulse with a wavelength spectrum FWHM of 14 nm. The solid line gives the best fit through the data points. The $FWHM_{env}$ is (36.8±0.2) mm. The error represents the standard deviation.

One advantage of the virtual lenslets is that there is no limitation to their size. The larger their size, the smaller the width of the diffraction pattern peak in their focal plane. The accuracy of the wave-front reconstruction depends on the accuracy with which the position of this peak can be determined. That means a smaller width of the diffraction peak results in higher accuracy. However, the shape of the wave-front becomes increasingly complicated with higher orders. In order to measure these complicated shapes the number of sampling points and thus the number of VLCs must be increased. An increase in the number of VLCs results in a reduction of the size of each VLC which in turn leads to a loss of reconstruction accuracy. Thus depending on the order of the wave-front aberrations to be measured a trade-off between size and number of VLCs has to be made. Several trials with a number of different VLC sizes have shown, that the 15×15 pixels size seems to be adequate for the aberrations with which CGWS was tested. An even greater advantage than variety in size is that due to the rather uniform light intensity in the sensor plane when employing VLCs, pixel saturation is not a problem. Earlier experiments with an actual lenslet array (Adaptive Optics Associates) showed that saturation is a common problem for real lenslets, because the intensity distribution in the sensor plane is very inhomogeneous. Besides that, all the other optical limitations associated with real lenses, such as lens errors, are eliminated if their virtual counterparts are used. The division into VLCs with a size of 15×15 pixels was achieved by covering the recorded image of the BFP of the objective on the CCD chip with a grid with a spacing of 15×15 pixels starting from the center of the objective BFP image. Each nodal point corresponds to the center of an individual VLC. In order to save computing time only those VLCs are taken into account whose radial distance to the center of the BFP image is less than or equal to 180 pixels. The resulting circle covers the complete image of the BFP. By combining the two parts of Eqs. (2.52), the electric field across the camera can be written in its usual complex form:

$$\begin{gathered}
I_1 - I_3 = I_D(\text{position }1) - I_D(\text{position }3) = A\cos(j_s - j_r) \\
I_4 - I_2 = I_D(\text{position }4) - I_D(\text{position }2) = -A\sin(j_s - j_r) \\
\Downarrow \\
I_1 - I_3 \hat{=} \operatorname{Re}\left(\tilde{E}_{\text{resultant}}\right) \\
I_4 - I_2 \hat{=} -\operatorname{Im}\left(\tilde{E}_{\text{resultant}}\right) \\
\Downarrow \\
\tilde{E}_{\text{resultant}} = (I_1 - I_3) - i(I_4 - I_2).
\end{gathered} \tag{2.56}$$

This electric field has the same wave-front as the sample arm, if, as is the case in this dissertation, the electric field in the reference arm has a planar wave-front. The light intensity distribution in the BFP of a lens is given by [Saleh and Teich 1991]

$$I(x,y) = \frac{1}{(l\ f)^2}\left|F\left(\frac{x}{l\ f},\frac{y}{l\ f}\right)\right|^2 \tag{2.57}$$

where l is the wavelength, f the focal length and $F\left(\frac{x}{l\ f},\frac{y}{l\ f}\right)$ is the Fourier transform of the electrical field distribution at the location of the lens, in the case at hand $\tilde{\mathrm{E}}_{\text{resultant}}(x,y)$. The position of the diffraction spots can thus be obtained by taking the square of the Fourier transform of the complex amplitude $\tilde{\mathrm{E}}_{\text{resultant}}(x,y)$ across each VLC, multiply it by the factor $1/(l\cdot f)^2$ and do a nonlinear position fit to the resulting data. This transform was implemented via the FFT algorithm supplied by MATLAB. The area to be Fourier transformed was padded with zeros until it reached the size of 65×65 pixels. This was done for a more precise sampling of the diffraction spot and to take the finite size of an individual VLC into account. The more precise sampling increases the position accuracy when the diffraction spot position is determined with the nonlinear fit. This fit uses again MATLAB's routine *nlinfit*. It turned out that in practice the individual diffraction images of the VLCs show high side peaks when CGWS is performed in scattering samples (cf. Figure 2.20). Therefore, the fit to find the diffraction spot position was restricted exclusively to the peak area, which was a 5×5 pixel area around the maximum value in the corresponding diffraction image.

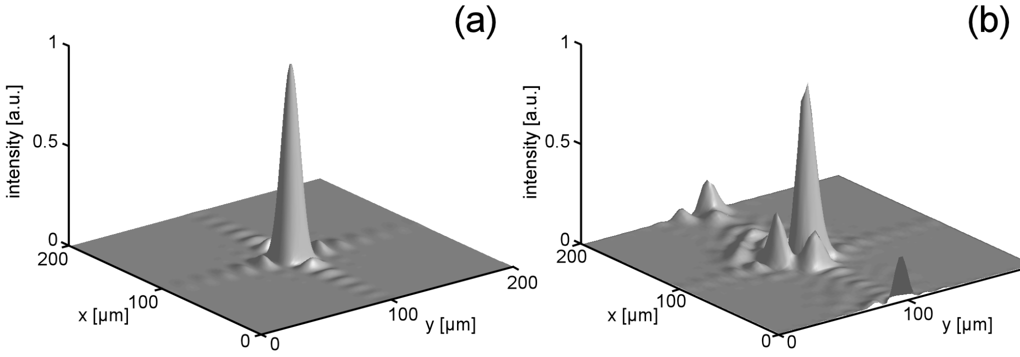

Figure 2.20: The theoretical intensity distribution of a diffraction pattern for a square lens with the parameters used in this thesis: an edge length of 195 mm and a focal length of 10120 mm (a). Typical diffraction pattern in the virtual focal plane of the virtual lenslets, calculated from the measured intensity across the VLCs via Fourier transform, in case of a scattering sample (b). x- and y-coordinates correspond to the coordinates in the focal plane of the lens. If the central peak of such a diffraction pattern is approximated by fitting a Gaussian the accompanying width parameter s of the Gaussian is » 5.44 mm in the theoretical case and only slightly different (6.12±0.16) mm in the case of the scattering sample, respectively. The small elevations at the ends of the parallel to the x-axis through the center peak in (b) are due to the interlaced operation of the camera resulting in an alternating intensity pattern in the recorded images.

Once the inverse coordinates of the diffraction spot positions in Fourier space are obtained, they are calculated backwards into real space coordinates by using

$$\begin{aligned} k_x &= \frac{x}{l\ f} \quad \Leftrightarrow \quad x = l\ f\, k_x \\ k_y &= \frac{y}{l\ f} \quad \Leftrightarrow \quad y = l\ f\, k_y \end{aligned} \tag{2.58}$$

with the spatial frequency coordinates k_x and k_y, and the real space coordinates x and y. With the conversion of the Fourier space coordinates into real space coordinates the wave-front sensing process is complete.

The reconstruction of the wave-front follows the scheme of a modal estimation algorithm [Cubalchini 1979] as already explained in section 2.2. For the real space coordinates obtained from Eqs. (2.58) the distance to the corresponding VLC center is determined. This corresponds to the TRAs *Dx* and *Dy* of subsection 2.2.1 and hence

$$\Delta x = \frac{f}{A}\int_{x_0-s}^{x_0+s}\int_{y_0-s}^{y_0+s}\frac{\partial W(x,y)}{\partial x}\,dx\,dy$$
$$\Delta y = \frac{f}{A}\int_{x_0-s}^{x_0+s}\int_{y_0-s}^{y_0+s}\frac{\partial W(x,y)}{\partial y}\,dx\,dy\ . \qquad (2.59)$$

Here, *f* and *A* represent the focal length and the area of the corresponding VLC. As mentioned earlier all VLCs are square with a side length of 15 pixels. Since the size of a pixel is roughly 13×13 μm^2 (cf. subsection 2.4.2) the side length of a VLC is 195 µm. Therefore *s* in the integral limits in Eqs. (2.59) has to be chosen half this side length, 97.5 µm. The variables x_0 and y_0 are the center coordinates of the related VLC and *W(x,y)* in Eqs. (2.59) represents the optical path length difference between the AWF and the plane reference wave-front. To expand *W(x,y)* in Zernike polynomials it must be mapped onto the unit circle. Thus

$$W(x,y) \quad \xrightarrow{u_x=\frac{x}{s.f.}\ ;\ u_y=\frac{y}{s.f.}} \quad W(u_x,u_y), \qquad (2.60)$$

where u_x and u_y are the dimensionless x- and y-coordinates on the unit circle and *s.f.* is the scale factor that ensures that u_x and u_y take only values between –1 and 1. This scale factor is equal to the distance between the outermost VLC and the center of the image of the BFP of the objective, i.e. 180·13 µm=2340 µm. Inserting the new variables in Eqs. (2.59), we can write

$$\frac{\Delta x}{f} = \frac{(s.f.)}{A}\int_{\frac{x_0-s}{s.f.}}^{\frac{x_0+s}{s.f}}\int_{\frac{y_0-s}{s.f.}}^{\frac{y_0+s}{s.f.}}\frac{\partial W(u_x,u_y)}{\partial u_x}\,du_x\,du_y$$
$$\frac{\Delta y}{f} = \frac{(s.f.)}{A}\int_{\frac{x_0-s}{s.f.}}^{\frac{x_0+s}{s.f}}\int_{\frac{y_0-s}{s.f.}}^{\frac{y_0+s}{s.f.}}\frac{\partial W(u_x,u_y)}{\partial u_y}\,du_x\,du_y\ . \qquad (2.61)$$

The next step is to replace $W(u_x,u_y)$ by its Zernike expansion (cf. section 2.2) $\sum k_i Z_i(u_x,u_y)$. The terms *Dx/f* and *Dy/f* in Eqs. (2.61) are combined for all VLCs to yield a vector that corresponds to the measurement vector $\vec{M}$ in section 2.2 Eq. (2.12). The integrals on the right hand side of Eqs.(2.61) are combined for all VLCs to form the matrix *D* (section 2.2 Eq. (2.17)), which contains the derivatives of the Zernike modes used (number two to number twenty-one). As explained in section 2.2 the least squares estimate for the k_i in the Zernike expansion of the wave-front is obtained by multiplying the measurement vector $\vec{M}$ with the pseudo-inverse of *D*, which is calculated applying MATLAB’s *pinv* routine. The multiplication with the pseudo-inverse completes the reconstruction process, and the reconstructed wave-front can then be represented by (cf. section 2.2)

$$W(u_x,u_y)=\sum_{i=2}^{21}\hat{k}_i Z_i(u_x,u_y). \tag{2.62}$$

2.4.4 Piezo Control

The depth discrimination in CGWS is achieved by using a phase shifting interferometry (PSI) algorithm as described above. Small changes in the optical path difference between the two interferometer arms were introduced by a movement of a piezo ceramic (cf. subsection 2.4.3). The resulting interference intensities can be used to eliminate the incoherent light by applying Eqs. (2.52). It is important that the piezo steps induce an interferometer arm length difference change of λ/8±10%, otherwise the PSI algorithm does not work correctly.

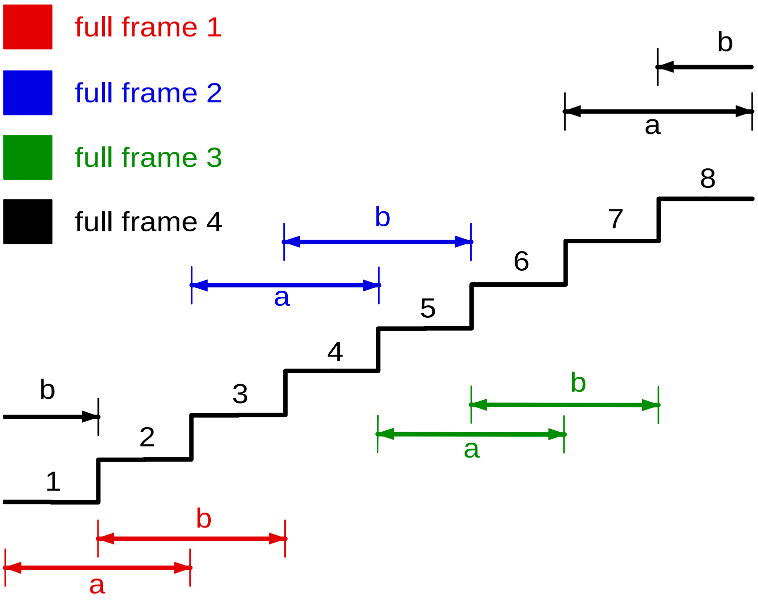

Figure 2.21: Arrangement of the piezo movements in order to implement a four-step PSI algorithm. The stair symbolizes eight actual positions of the piezo. Every position is kept for half the integration time of one half-frame of the camera module (a or b). In this manner four full frames (color coded red, blue, green and black) are recorded for eight piezo positions. If the positions of the piezo each induce a reference arm length reduction of 1/8 applying the difference (full frame 4 – full frame 2) as well as (full frame 3 – full frame 1) establishes the desired PSI algorithm.

This could be achieved with four steps of length λ/4 each. But taking the operation principle of the CCD camera (cf. subsection 2.4.2) into account, this would follow a scheme that unnecessarily needs more time than actually required for this task. A more appropriate way is to use the scheme depicted in Figure 2.21.

To be able to implement this scheme, the piezo and the camera must be synchronized. To ensure this, an appropriate electrical control circuit, depicted in Figure 2.22, was assembled. The core element of this circuit is a synchronous 4-bit binary counter (74LS161AN). Every time a vertical-sync (V_{sync}) signal from the camera arrives at the input pin of this counter, its count increases by one. The output pins follow the truth table shown in Table 2.3. If all the possible counting states of the 74LS161AN were used directly, fifteen piezo steps would result. In order to accomplish the scheme as illustrated in Figure 2.21 the highest bit (output pin number 11, Q_D in Figure 2.22, respectively) is neglected. As a consequence, the counting states number one through eight are indistinguishable from states number nine through sixteen. The outcome is eight piezo states instead of sixteen. As mentioned above, these states each need to induce the same path length difference of the interferometer arms. To achieve this, the resistors of the control circuit depicted in Figure 2.22 must be chosen appropriately. The control circuit can be depicted by the equivalent circuit diagram Figure 2.23 if R_A is chosen to be equal to $4R_C$ and R_B is chosen to be equal to $2R_C$.

Table 2.3: Pin assignment table in used circuit for output pins of the synchronous counter 74LS161AN.

	Count															
output pin	1	2	3	4	5	6	7	8	9	10	11	12	13	14	15	16
14	0	1	0	1	0	1	0	1	0	1	0	1	0	1	0	1
13	0	0	1	1	0	0	1	1	0	0	1	1	0	0	1	1
12	0	0	0	0	1	1	1	1	0	0	0	0	1	1	1	1
11	0	0	0	0	0	0	0	0	1	1	1	1	1	1	1	1

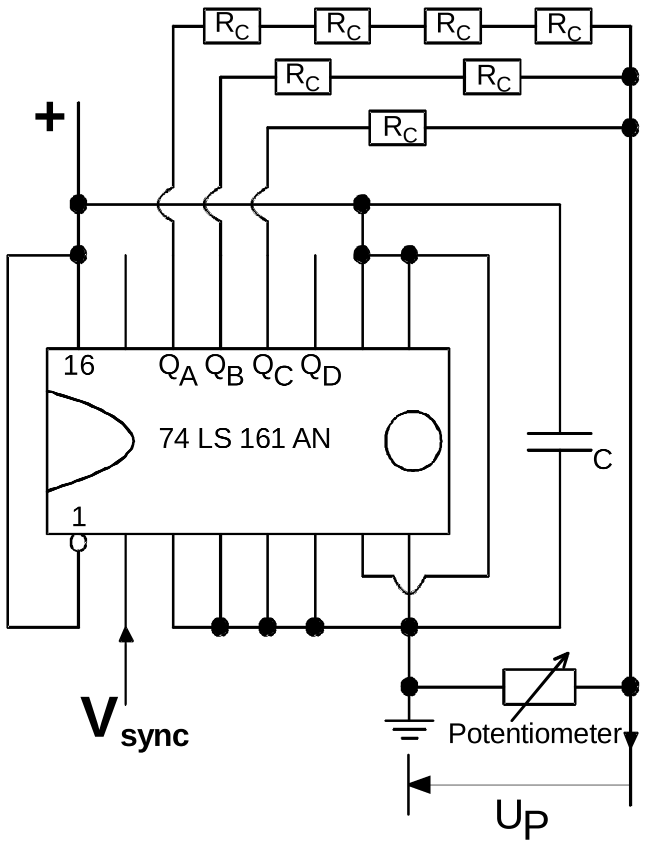

Figure 2.22: The electrical synchronization control circuit. V_{sync} is the input signal from the camera. As can be seen the output voltage is controlled via a potentiometer P.

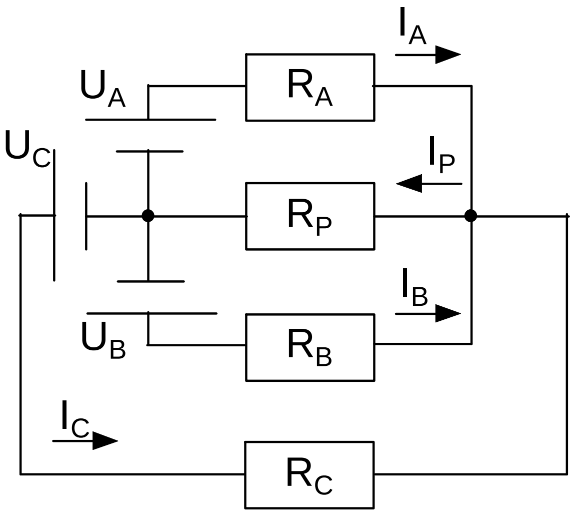

Figure 2.23: Equivalent circuit diagram for the wiring diagram depicted in Figure 2.22.

Applying Kirchhoff’s laws to the circuit depicted in Figure 2.23 leads to

$$\begin{aligned} U_P &= \left(\frac{U_A}{4R_C}+\frac{U_B}{2R_C}+\frac{U_C}{R_C}\right)\Big/\left(\frac{1}{4R_C}+\frac{1}{2R_C}+\frac{1}{R_C}+\frac{1}{R_P}\right) \\ &= \frac{U_A+2U_B+4U_C}{4R_C}\Big/\left(\frac{1+2+4}{4R_C}+\frac{1}{R_P}\right) \\ &= \frac{U_A+2U_B+4U_C}{4R_C}\Big/\frac{7R_P+1}{4R_C R_P} \\ &= \frac{(U_A+2U_B+4U_C)\cdot R_P}{7R_P+1}. \end{aligned} \tag{2.63}$$

This can be rewritten to

$$U_P = R_P\cdot(U_A+2U_B+4U_C)\cdot k(R_P). \tag{2.64}$$

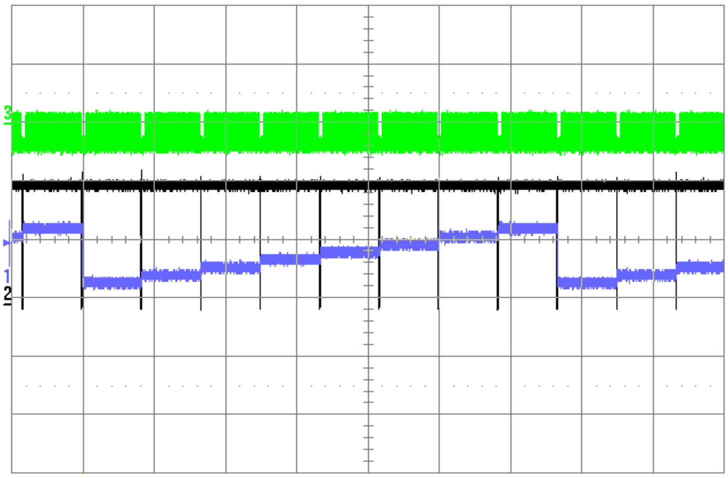

Figure 2.24: The synchronization and stepping process as seen on an oscilloscope. Trace number 3 (green) shows the measured readout signal of the CCD camera. The half-frames are clearly distinguishable. Trace number 2 (black) shows the V_{sync}-signals coming from the CCD camera. They represent the input for the circuit depicted in Figure 2.22. Trace number 1 (light blue) illustrates the measured stair structure output of this circuit.

Since the 74LS161AN component is a binary counter, the output pins can be either high or low. If a pin is low, no output voltage is generated for this pin. If a pin is high, an output voltage for this pin is generated with an amplitude that is the same for all pins that are high. Thus the mirror mounted on the piezo ceramic (cf. Figure 2.18) runs through eight individual equidistant positions (cf. Eq. (2.64)). In practice this synchronization and stepping process looks as depicted in Figure 2.24.

The resistance of the potentiometer R_P can be used for adjusting the step size so that it is equal to a length difference of $l/8$. These adjustments can be checked by means of the interferograms. In a first step, the interferometer is aligned in such a way that interference fringes become visible. The easiest way to achieve this is to use a planar reflecting surface as a sample, e.g. a plane-parallel BK7 plate. In a second step, the reference arm is scanned by adjusting the 90° right-angle prism until fringes appear. Then R_P is gradually increased, while the result of passing quadruplets of frames through the algorithm described in Eq. (2.53) is observed on the camera. The correct value of R_P is found if the resulting image is free of interference fringes (Figure 2.25).

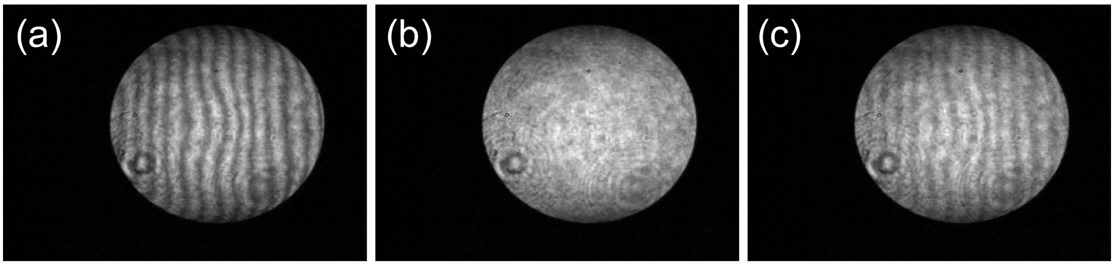

Figure 2.25: If the value for the potentiometer resistance R_P is either too low or too high, fringes are still visible after the algorithm Eq. (2.53) has been applied, (a) and (c). However, if the right value for R_P is selected these fringes vanish (b).

2.4.5 Dispersion Compensation

The depth discrimination ability of CGWS and in particular the depth resolution is determined by the coherence length of the light source (cf. subsection 2.2.2). Ultrashort laser pulses are, therefore, particularly suitable for CGWS. Such a pulse is spread in time due to GVD. This effect is due to the fact that the light in ultrashort pulses consists of quite a range of optical frequencies. The depth resolution of the CGWS method, that is the thickness of the layer from where light is detected, depends on the difference of GVD present in both interferometer arms. It is possible to minimize the layer thickness by minimizing the difference of GVD. This was done by adding the proper amount of glass in the reference arm with the BK7 prisms (cf. Figure 2.18). If the amount of GVD in both arms is the same, the envelope of the cross-correlation of the light pulses in both arms will be minimal. Mathematically this can be expressed as follows:

If we assume a Gaussian pulse form, an analytic treatment is possible. Such a pulse can be described in the time-domain as [Siegman 1986]

$$E(t) = \exp\left(-at^2\right)\exp\left(i\left[w_0 t + bt^2\right]\right) \equiv \exp\left(-\Gamma t^2\right)\exp\left(i w_0 t\right) \tag{2.65}$$

and in the frequency domain as

$$E_0(t) = \exp\left(-\Gamma_0\, t^2 + i w_0 t\right) \quad \overset{\text{Fourier transform}}{\Leftrightarrow} \quad \tilde{E}_0(w) = \exp\left(-\frac{(w - w_0)^2}{4\Gamma_0}\right). \qquad (2.66)$$

The extra phase, which is acquired while the pulse propagates through a dispersive medium can be described by including the term $\exp[-ib\,(w)z]$. Here the “free space” propagation constant b is given by [Siegman 1986]

$$b\,(w) = w\sqrt{me} = \frac{w}{c} = \frac{nw}{c_0}. \qquad (2.67)$$

If only narrowband signals having frequency components near some center frequency w_0 are of concern, the propagation constant of a dispersive medium can be expanded at w_0 to

$$b\,(w) = b\,(w_0) + \left.\frac{db}{dw}\right|_{w_0} \cdot (w - w_0) + \tfrac{1}{2}\left.\frac{d^2 b}{dw^2}\right|_{w_0} \cdot (w - w_0)^2 + O(3). \qquad (2.68)$$

Thus, if the input into such a dispersive medium is given by Eq. (2.66), the output pulse spectrum $\tilde{E}(z,w)$ is

$$\begin{aligned} \tilde{E}(z,w) &= \tilde{E}_0(w)\cdot \exp[-ib\,(w)z] \\ &= \exp\left[-ib\,(w_0) - ib\,'z\cdot(w - w_0) - \left(\frac{1}{4\Gamma_0} + \frac{ib\,''z}{2}\right)\cdot(w - w_0)^2\right]. \end{aligned} \qquad (2.69)$$

This is the general form of a chirped Gaussian pulse with the initial complex Gaussian parameter $\Gamma_0 = a_0 - ib_0$. Clearly the output pulse in time from this system will be the inverse Fourier transform of Eq. (2.69). After some mathematical effort [Siegman 1986] this looks like

$$E(z,t) = \frac{e^{i[w_0 t - b\,(w_0)z]}}{2p} \int_{-\infty}^{\infty} \exp\left[-\frac{(w - w_0)^2}{4\Gamma(z)} + i(w - w_0)(t - b\,'z)\right] d\,(w - w_0), \qquad (2.70)$$

where $1/\Gamma(z) \equiv 1/\Gamma_0 + 2ib^{''}z$. The Gaussian pulse parameter Γ(z) has changed but the pulse profile is still Gaussian. Using the mathematical identity

$$\int_{-\infty}^{\infty} e^{-ax^2-2bx}dx \equiv \sqrt{\frac{p}{a}}\exp\left[\frac{b^2}{a}\right], \quad \text{if } \mathrm{Re}(a) > 0 \tag{2.71}$$

yields

$$\begin{aligned} E(z,t) &= \exp[i(w_0 t - b(w_0)z)]\cdot\exp\left[-\Gamma(z)\cdot(t-b^{'}z)^2\right] \\ &= \exp\left[iw_0\left(t-\frac{z}{\mathrm{v}_j(w_0)}\right)\right]\cdot\exp\left[\Gamma(z)\left(t-\frac{z}{\mathrm{v}_g(w_0)}\right)^2\right]. \end{aligned} \tag{2.72}$$

As can be seen from the first exponent in Eq. (2.72) the phase of the carrier frequency w_0 is delayed by a midband phase shift $b(w_0)z$ after propagating a distance z. This means that the sinusoidal waves within the pulse envelope appear to move forward with *midband phase velocity*

$$\mathrm{v}_j(w_0) = \frac{w_0}{b(w_0)}. \tag{2.73}$$

The second exponent in Eq. (2.72) indicates that the pulse envelope itself is delayed by the group delay time $b'z$ and appears to move forward with *group velocity*

$$\mathrm{v}_g(w_0) = 1\bigg/\left(\frac{db}{dw}\right)\bigg|_{w=w_0}. \tag{2.74}$$

The change of the new Gaussian pulse parameter Γ(z) is determined by b'' as follows from Eq. (2.70). This parameter b'' is called the *group velocity dispersion (GVD)*

$$b^{''} = \frac{d}{dw}\left(\frac{1}{\mathrm{v}_g(w)}\right) = \left(-\frac{1}{\mathrm{v}_g^{\,2}(w)}\frac{d\mathrm{v}_g(w)}{dw}\right)\bigg|_{w=w_0} = -\frac{1}{\mathrm{v}_g^{\,2}(w_0)}\frac{d\mathrm{v}_g(w)}{dw}\bigg|_{w=w_0}. \tag{2.75}$$

The group velocity as a function of a frequency deviation of a signal can be expanded. Using Eq. (2.75) will reveal that the group velocity itself is a frequency dependent quantity

$$\mathrm{v}_g(w) \approx \mathrm{v}_g(w_0) - b''\mathrm{v}_{\mathrm{g}}^2(w_0)\cdot(w - w_0). \tag{2.76}$$

Physically this can be interpreted if we do not think of one pulse, but of a number of sub-pulses, each with a slightly different carrier frequency and correspondingly a slightly different group velocity. Then in a simple way it can be said, that each frequency component of the pulse travels at a slightly different group velocity. This influences the overall shape of the pulse. Mathematically this becomes apparent by the change in $\Gamma(z)$

$$\begin{aligned}
\frac{1}{\Gamma} &= \frac{1}{a - ib} + 2ib''z = \frac{a + i\left(b + 2b''\left(a^2 + b^2\right)z\right)}{a^2 + b^2} \\
\Gamma &= \frac{a^3 + ab^2}{a^2 + \left(b + 2b''\left(a^2 + b^2\right)z\right)^2} - i\frac{\left(a^2 + b^2\right)\left(b + 2b''\left(a^2 + b^2\right)z\right)}{a^2 + \left(b + 2b''\left(a^2 + b^2\right)z\right)^2}.
\end{aligned} \tag{2.77}$$

A pulse like Eq. (2.66) in the frequency domain is related to a pulse in the time domain by

$$\tilde{E}(w) = e^{-aw^2 + igw^2} \overset{\text{Fourier transform}}{\Leftrightarrow} E(t) = e^{-\frac{a - ig}{4\left(a^2 + g^2\right)}t^2} e^{-iw_0 t}. \tag{2.78}$$

The interference term in the cross-correlation of two such pulses is proportional to

$$\begin{aligned}
&\int_{-\infty}^{+\infty} \mathrm{Re}\left[E_1(t)E_2^*(t - t)\right] dt = \\
&\int_{-\infty}^{+\infty} \mathrm{Re}\left[\exp\left(-\frac{a_1 - ig_1}{4\left(a_1^2 + g_1^2\right)}t^2\right)\exp\left(-\frac{a_2 - ig_2}{4\left(a_2^2 + g_2^2\right)}(t - t)^2\right)\right] dt \equiv \\
&\int_{-\infty}^{+\infty} \mathrm{Re}\left[\exp\left(-At^2\right)\exp\left(-B(t - t)^2\right)\right] dt.
\end{aligned} \tag{2.79}$$

Since the pulses have the same spectral width, a_1 must be equal to a_2. With a quadratic completion the integral becomes tractable, and Eq. (2.79) then becomes

$$
\begin{aligned}
&\mathrm{Re}\left[\exp\left(\left[\frac{B^2}{A+B}-B\right]t^{2}\right)\right]= \\
&\exp\left[-\mathrm{Re}\left(\frac{A\cdot B}{A+B}\right)t^{2}\right]\cdot\mathrm{Re}\left(\exp\left[-i\,\mathrm{Im}\left(\frac{A\cdot B}{A+B}\right)t^{2}\right]\right).
\end{aligned}
\tag{2.80}
$$

The first term in the second line of Eq. (2.80) gives the envelope of the interference term and the second term corresponds to the oscillation term. For the width of the interference term only the first term has to be taken into account. The width of the square of the envelope is then proportional to

$$
\left[\mathrm{Re}\left(\frac{A\cdot B}{A+B}\right)\right]^{-1}.
$$

After some mathematical manipulation the result can be written as

$$
\mathrm{width}^{2}\propto\frac{2\left(4a+\left(g_1-g_2\right)^2\right)}{a}. \tag{2.81}
$$

Using Eqs. (2.69) and (2.78) we find

$$
.g=\frac{b\ z}{2}\quad\Rightarrow\quad g_1=\frac{b_1^{''}z_1}{2}\quad\text{and}\quad g_2=\frac{b_2^{''}z_2}{2}. \tag{2.82}
$$

It is clear from Eq. (2.81) that the width of the cross-correlation is minimal if the same amount of second order dispersion is present in both interferometer arms. If this condition is met the depth resolution of the PSI algorithm is at its optimum for the spectrum of the light source used.

As mentioned above the prisms in the reference arm (cf. Figure 2.18) were used to balance the GVD of the optical elements of the sample arm. The FWHM of the cross-correlation envelope was measured for various amounts of glass in the optical path of the reference arm (Figure 2.26). The minimum FWHM that could be achieved was (33.5±0.25) µm for 5 cm of BK7 glass (Figure 2.27), which is in good agreement with the expected value (32.7 µm), calculated from Eq. (2.55).

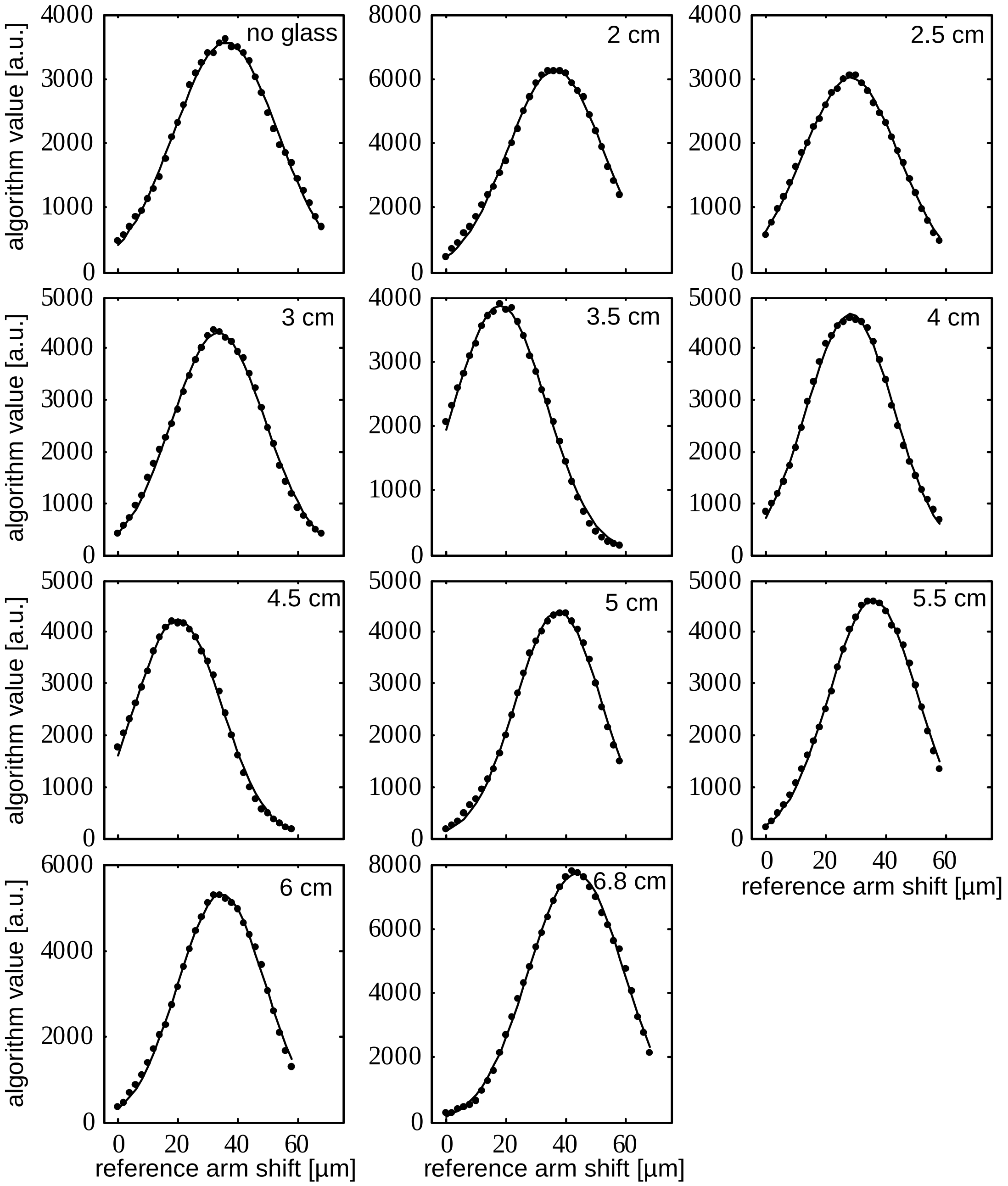

Figure 2.26: Data for envelopes of Eq. (2.53) as a function of optical reference arm length shift for several thicknesses of BK7 glass in the reference arm (the amount of glass is always given at the upper right of each subimage). The solid lines are nonlinear fits to the data.

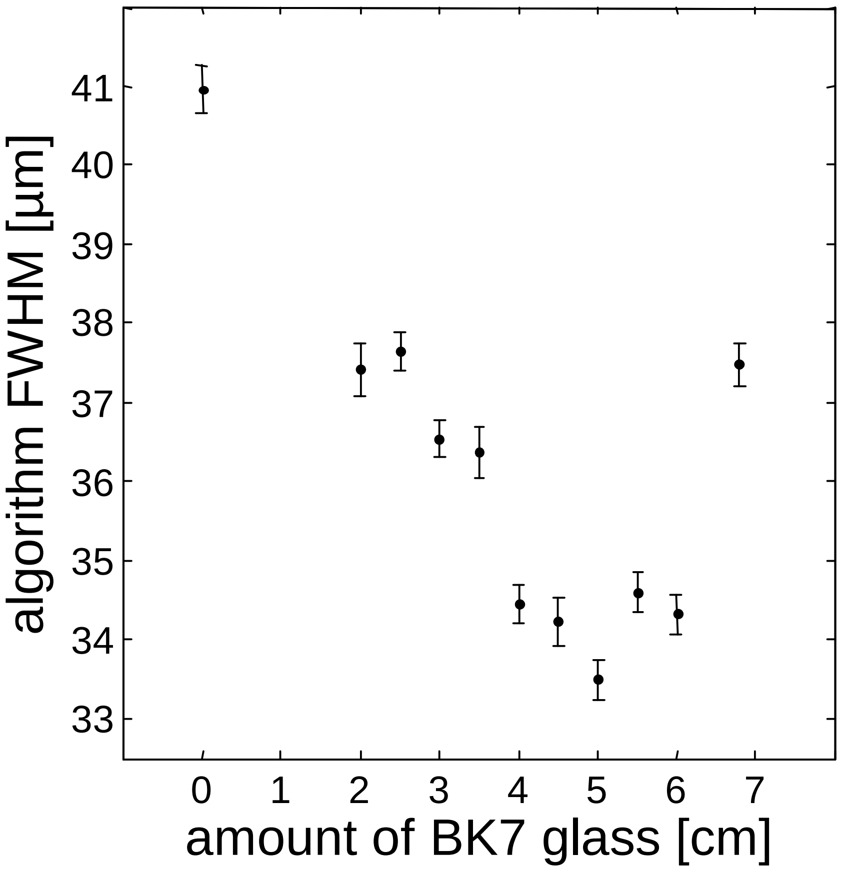

Figure 2.27: The FWHM for the envelopes resulting from the application of Eq. (2.53) to the cross-correlation of the interferometer as a function of the amount of BK7 glass in the reference arm. This illustration shows that the GVD induced in the sample arm is balanced when the BK7 in the reference arm has a thickness of 5 cm.

3 Results and Discussion

In the previous chapter the realization of CGWS was illustrated. This new approach of measuring wave-fronts was validated by studying the effects of two different wave-front aberrations, defocus and astigmatism, on two types of samples. The description of the resulting four tests and the discussion of the results is the topic of this chapter.

The first test sample was a mirror perpendicular to the OA and the first aberration tested was defocus. A glass cover slip was then added between mirror and objective with the surface normal tilted slightly away from the OA to induce aberrations of higher order than defocus, for example astigmatism. Both, defocus and astigmatism were subsequently tested using a scattering sample instead of a mirror.

3.1 Experiments with a Quasi Point Source

Inserting a mirror or a reflecting surface perpendicular to the OA results in the objective registering a spherical wave emitted by a quasi point source of light (QPS) on the OA. Only a section of this spherical wave, the detection cone, reaches the objective (Figure 3.1). Changing the position of the QPS along the OA induces defocus.

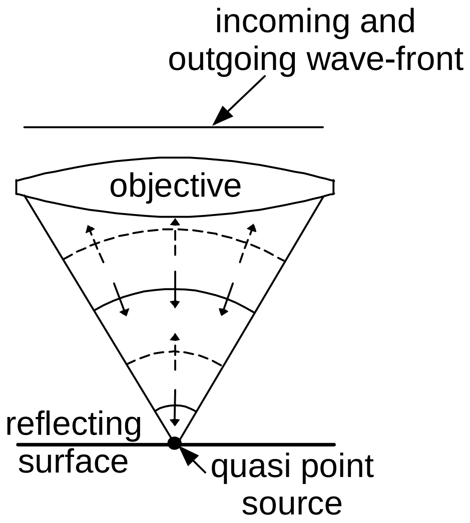

Figure 3.1: The objective converts a plane wave into a spherical wave (solid circle sections) converging onto the focus. If a reflecting surface is positioned beneath the objective (in the depicted case in the focus) the spherical wave-front will be reflected. For the objective this looks like a point source of light sitting in the focus. Defocus is induced by changing the position of this QPS along the OA.

3.1.1 Defocus with a Mirror Sample

The first step of the test measurement was to bring the reflecting surface into the focal plane of the objective. This was achieved by looking at the interference fringes on the CCD camera while the distance between reflecting surface and objective was changed. The curvature of the fringes will change with distance alteration. If the curvature is absent, the reflecting surface is in the focal plane and the QPS in the focus of the objective. Aligning the interferometer arms subsequently to equal optical path length, as explained in subsection 2.4.3, maximizes the contrast. The scattering sample does not allow this alignment. Therefore, the same procedure had to be performed prior to using scattering samples in order to ensure that the focal plane of the objective lies in the CG.

Defocus was induced by moving the reflecting surface in steps of 1 µm starting from 5 µm above the original objective focus to 5 µm below the original objective focus. This corresponds to a range of positions of the QPS from 10 µm above the original objective focus to 10 µm below the original objective focus in steps of 2 µm (Figure 3.2). The PSI algorithm was applied to extract the complex amplitude as pointed out in subsection 2.4.3. Then the propagation of this complex amplitude through the virtual lenses was calculated via Fourier transforms for each VLC (cf. subsection 2.4.3).

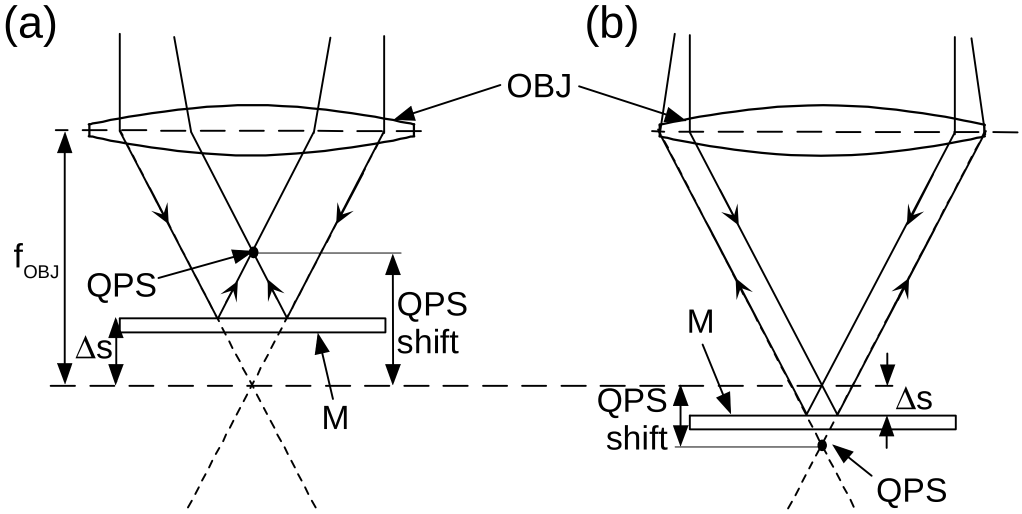

Figure 3.2: A mirror shift (Ds) results in a position change of the quasi point source (QPS shift) that is twice as large. If the mirror (M) is shifted towards the objective (OBJ), the distance OBJ-QPS becomes smaller than the focal length (f_{OBJ}) and the wave-front diverges after transmission through the objective (a). In analogy to this a mirror shift away from the objective leads to a converging wave-front after transmission through the objective (b).

Virtual diffraction patterns are the consequence. Phase-slope extraction was done by fitting the peak positions of these virtual diffraction patterns in the focal plane of the virtual lenslets and comparing these positions to the lenslet centers (cf. subsection 2.4.3). Fitting the twenty Zernike polynomials (Z_2 to Z_{21}, Z_1 represents piston and is neglected) to the wave-front gradient data allows the reconstruction of the wave-front (Figure 3.3).

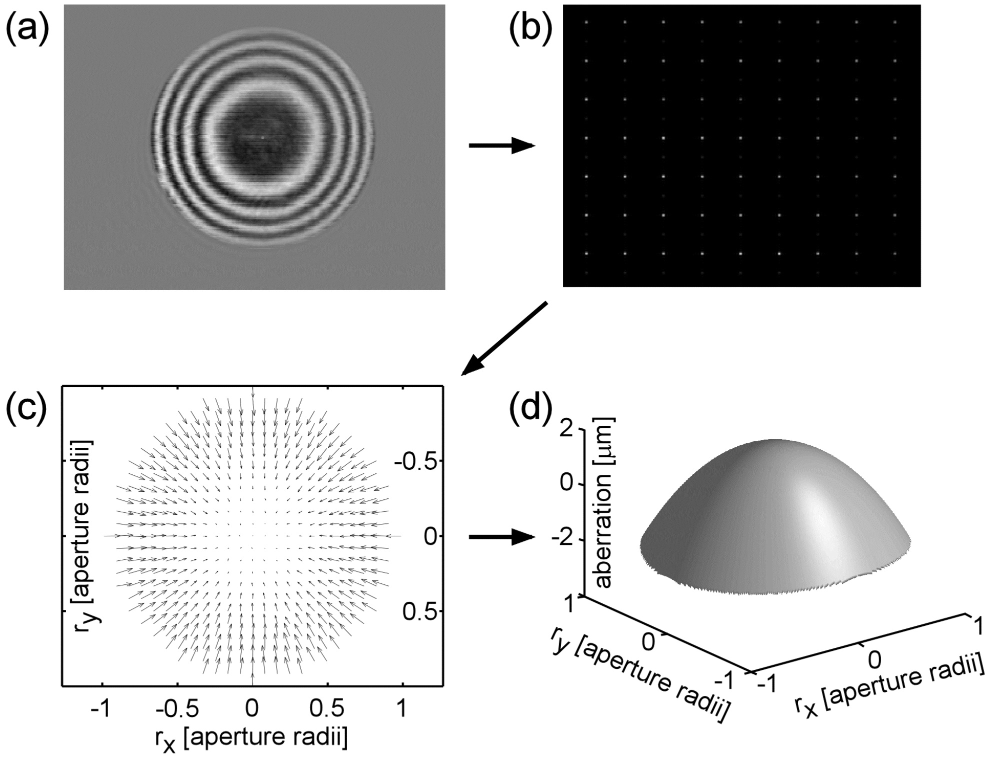

Figure 3.3: CGWS scheme for a mirror sample. Real part (a) of the complex amplitude for a QPS position 10 mm beneath the original focus. Numerical propagation through the virtual lenslets via Fourier transformation leads to virtual diffraction spots. A zoom is depicted in (b). Gradient information is extracted by fitting the diffraction spot positions and comparing these positions to the lenslet centers (c). Finally a sum of Zernike polynomials is fitted to these gradient data in order to reconstruct the wave-front (d).

A typical result for the Zernike coefficients obtained for a single QPS position experiment of this kind contains a dominant Zernike defocus coefficient (ZC_4) (Figure 3.4). All coefficients for higher order polynomials (> 11) were small. In addition to defocus, in this experiment the Zernike coefficient amplitudes for tilt about the y-axis (ZC_3), astigmatism (ZC_6) and spherical aberration (ZC_{11}) departed significantly from a zero value (Figure 3.4). Since tilt is no real wave-front aberration but misalignment problem, it is neglected. Piston cannot be measured in a SHS and is, therefore, also neglected. The Zernike coefficients of these three polynomials (ZC_1-ZC_3) will not be taken into account in the future considerations of this work (although ZC_2 and ZC_3 need to be included in the modal estimation algorithm). One potential source of spherical aberration (ZC_{11}) are the two beam splitter cubes in the sample arm, since they represent plane-parallel glass plates and hence can cause spherical aberration and, if tilted to the OA, astigmatism (cf. subsection 3.1.2). The value of the astigmatism coefficient depends mainly on the tilt angle and thickness of an inserted glass plate, in this case on the tilt angle of the beam splitter cubes and their thickness. Shifting the QPS position should have no effect on ZC_6. Nevertheless it can be observed that ZC_6 changes systematically with the QPS shift (Figure 3.5).

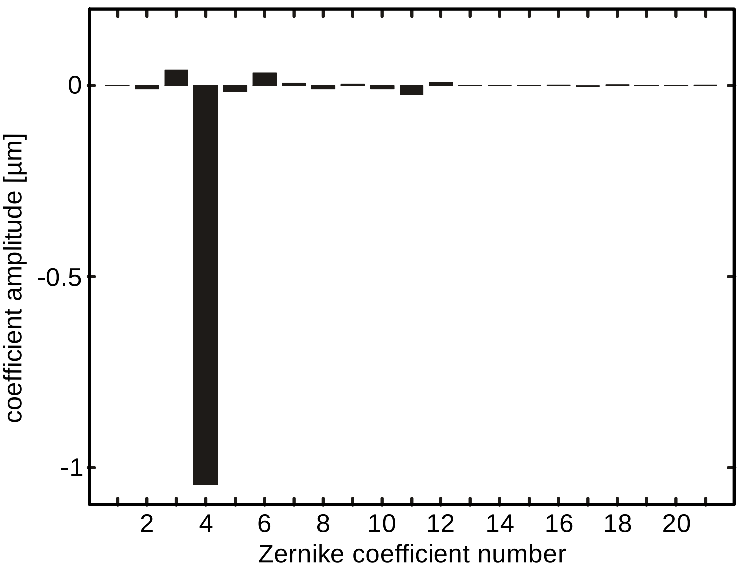

Figure 3.4: Fitted Zernike coefficients for a QPS position 10 mm below the original focus of the objective for a mirror as a sample. Dominant is the Zernike defocus coefficient (ZC_4). All higher order coefficients (coefficient number > 11) are negligible.

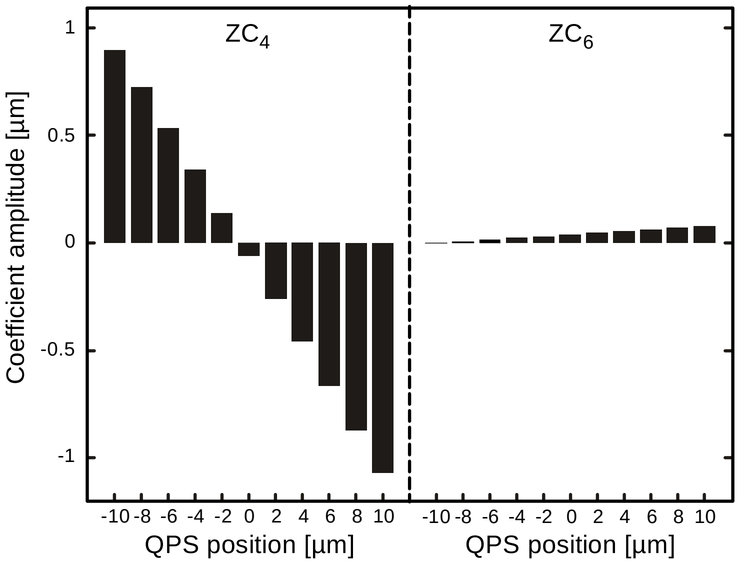

Figure 3.5: Zernike coefficient amplitude for defocus (ZC_4) and astigmatism (ZC_6) as functions of QPS position. Positive values of the QPS position are below the original focus. The numerical values for the shifts of the virtual diffraction spot positions from their lenslet centers were calculated with the dimensions for a camera pixel found in subsection 2.4.2, 13.25 mm for the short axis and 12.85 mm for the long axis. The fact that ZC_4 has an amplitude of -0.06 mm for the QPS in the focus is due to a positioning inaccuracy of the micrometer-screw that drives the mirror sample.

The systematic change did not vary when the camera was rotated about the OA and the QPS was shifted again. This indicates that the systematic change is a problem due to the camera pixel size asymmetry and may indicate that the pixel dimensions determined in subsection 2.4.2 were not precise enough.

Defocus is a rotationally symmetric aberration and if astigmatism is due to a disturbance of any of the elements of the setup, this symmetry is broken. If actual astigmatism is present in the wave-front, rotating the camera must, therefore, change the astigmatism coefficient because the orientation of the wave-front with respect to the camera is changed.

Since the dimensions of a camera pixel were used to calculate the shifts of the virtual focal spots of the VLCs they do influence the result of the wave-front reconstruction directly. And if the pixel dimensions used in the wave-front analysis calculations are different from the actual dimensions, spurious astigmatism that is fixed now in the camera frame of reference occurs. Rotating the camera would then change nothing. In addition, for defocus the shifts of the virtual focal spots increase linearly with QPS shifts away from the focus, which would lead to a linear change of ZC_6 with these QPS shifts if the pixel dimensions differ from the actual values.

Since no change of ZC_6 behavior for rotating the camera and a linear change of ZC_6 with QPS shift were observed, the dimensions for a single pixel used for the wave-front analysis found in subsection 2.4.2 have to be adjusted. This is done by adjusting their x- and y-values so that ZC_6 became independent of the QPS position. The new dimensions of a pixel were 13.15 µm for the short, (y-)axis and to 13 µm for the long, (x-)axis (these values for the pixel dimensions differ not significantly from their earlier found counterparts in subsection 2.4.2, which were (13.25±0.22) µm for the short axis and (12.85±0.07) µm for the long axis, respectively). Using the new pixel dimensions the astigmatism coefficient ZC_6 stays constant during changes of the QPS position (Figure 3.6).

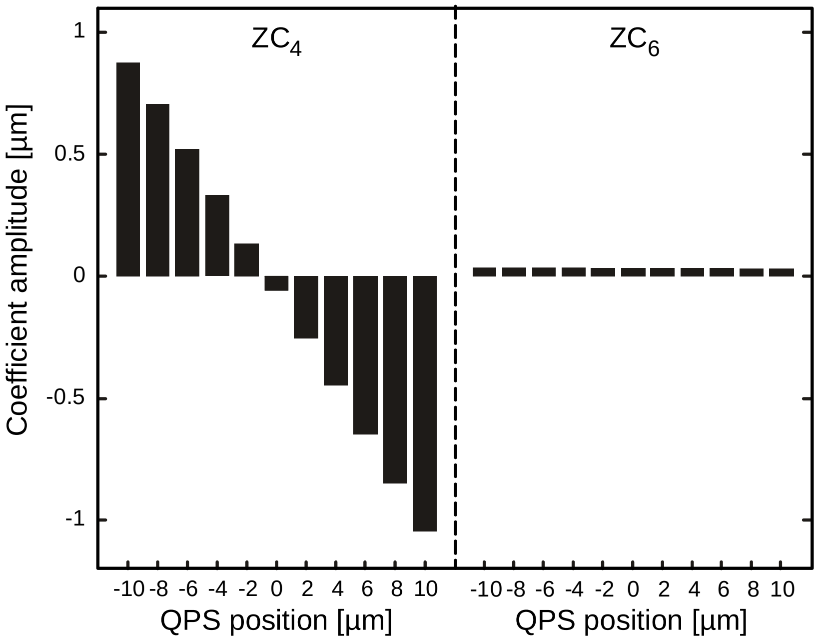

Figure 3.6: Zernike coefficient amplitude for defocus (ZC_4) and astigmatism (ZC_6) as functions of QPS position. Positive values of the QPS position correspond to positions below the original focus whereas negative values correspond to positions between objective and original focus. The numerical values for the shifts of the virtual diffraction peaks away from the lenslet centers were calculated in this case with camera pixel dimensions of 13.15 mm for the short axis and 13 mm for the long axis.

Deriving a theoretical estimate for the defocus coefficient

The defocus measurement was compared to a theoretical estimate that was derived by comparing transit times for different light paths that all start from different points on the OA and all end in points on the BFP of the objective, the plane which is imaged onto the virtual SHS (cf. subsection 2.4.3). Since defocus is a rotationally symmetric aberration it is sufficient to describe the situation in two dimensions (Figure 3.7).

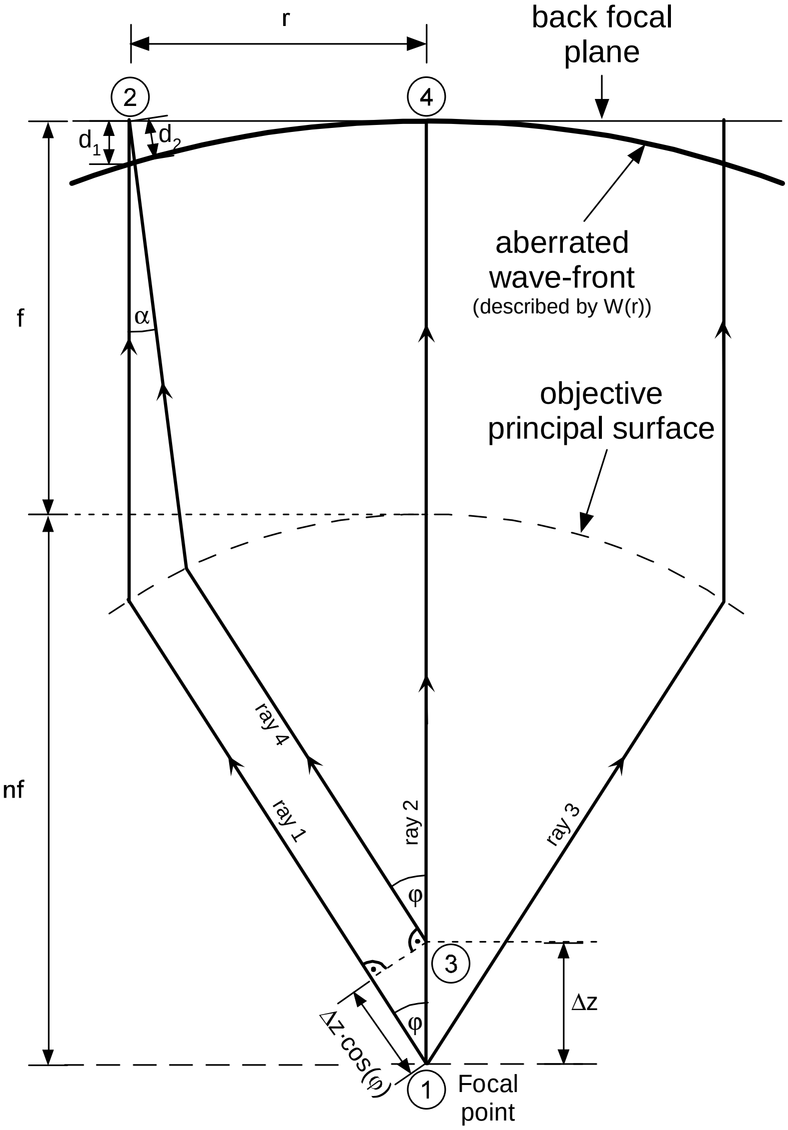

Figure 3.7: Comparing transit times for light starting from a point source (for example point 3) to transit times for light starting in the focus (point 1) leads to the theoretical estimate for the Zernike defocus coefficient behavior. According to Juškaitis [Juškaitis 2003] the principal surface of the objective corresponds to a circle segment of radius nf.

A spherical wave-front starting from a point source in the focus corresponds to a planar wave-front in the BFP. Thus all the light paths starting from the focus have the same transit time to reach the BFP of the objective (the planar wave-front will as always in this dissertation serve as reference wave-front). Light starting from points above or beneath the focus result in

AWFs in the BFP. It is the optical path length difference *W(r)* between those AWFs and the planar reference wave-front that is measured (cf. section 2.2). Starting at the focus (point 1 in Figure 3.7) there is exactly one angle j that corresponds to a point (point 2) in the BFP of the objective. All light paths starting in the focus (point 1) will have the same transit time t_0 to get to the BFP. Examples for equal transit time are ray 1, ray 2 and ray 3. However, the transit time is different for ray 4. Its angle with the OA is the same as for ray 1 and therefore it hits the BFP at the same point as ray 1, namely point 2 in Figure 3.7. According to their different optical path lengths the transit time $t_{3\to 2}$ for light propagating from a QPS in point 3 to point 2 will be smaller than for light propagating from point 1 to point 2. According to Fermat's Principle, all rays of a planar wave-front that are transmitted through the objective have the same optical path length when they reach their common focusing point in the BFP. Thus, the difference between t_0 and $t_{3\to 2}$ is

$$t_0 - t_{3\to 2} = \frac{\Delta z \cdot \cos j \cdot n}{c_0}. \tag{3.83}$$

The constant n in Eq. (3.83) is the index of refraction of the immersion medium, c_0 is the speed of light in vacuum and *Dz* is the distance between QPS and focus. The same argument for light propagating from point 3 to point 4 parallel to ray 2 yields the transit time difference

$$t_0 - t_{3\to 4} = \frac{\Delta z \cdot n}{c_0}. \tag{3.84}$$

Thus the transit time difference $Dt_{transit}$ between rays propagating from point 3 to point 2 and those propagating from point 3 to point 4 is

$$\Delta t_{transit} = t_{3\to 2} - t_{3\to 4} = \frac{\Delta z \cdot n}{c_0}(1 - \cos j). \tag{3.85}$$

As can be seen from the above derivation, for points on the OA above the focus $Dt_{transit}$ has to be positive. For light starting from a point on the OA beneath the focus an analogous derivation leads to the same equation (Eq. (3.85)), but then with the opposite sign. Thus Eq. (3.85) can be used for starting points above or below the focus, when assigning a negative *Dz* for points above and a positive *Dz* for those below. Eq. (3.85) is then

$$\Delta t_{transit}(r, \Delta z) = \Delta z \cdot \frac{n}{c_0}\left(\cos\left[\arcsin\left\{\frac{r}{n \cdot f}\right\}\right] - 1\right). \tag{3.86}$$

Here, *j* is expressed as arcsin(*r*/[*n*·*f*]) (cf. Figure 3.7). Figure 3.7 shows also that d_1 is the optical path length difference belonging to a certain *r* and certain *j*. But the calculated time difference for *W(r)* is actually described by d_2. For small focus shifts *Dz,* the angle *a* in Figure 3.7 is small and, therefore, the deviation from d_2 to d_1 is small. Expressing d_1 in terms of *Dz* and *r* yields

$$\begin{aligned} d_1 &= d_2 \cdot \cos a \\ &= d_2 \cdot \cos\left(\arcsin\left[\frac{r - \dfrac{r \cdot \left(nf - \Delta z\sqrt{1-\frac{r^2}{n^2 f^2}} \right)}{nf}}{nf + f - \Delta z - \sqrt{1-\frac{r^2}{n^2 f^2}} \cdot \left(nf - \Delta z\sqrt{1-\frac{r^2}{n^2 f^2}} \right)} \right] \right). \end{aligned} \tag{3.87}$$

Thus, a relative deviation of d_2 to d_1 of only one per cent is present for the maximum occurring radius in the actual experiment $r_{\max}$=2340 µm (cf. subsection 2.4.3) and a *Dz* of roughly 880 µm (above or below the focus). Therefore d_1 and d_2 can be treated as equal for all shifts *Dz* that occur in this dissertation, where *Dz* is always smaller than 80 µm.

The next step in deriving the theoretical estimate for the Zernike defocus coefficient is to expand the optical path length difference $c_0 \cdot Dt_{transit}(r)$ in terms of Zernike polynomials. In order to do so, the time difference must be mapped onto the unit circle, i.e. expressed as a function of radius $r = {}^{r}\!/_{r_{\max}}$ and the azimuthal angle *q*. The optical path length difference W(*r*,*q*) then is

$$W(r, q, \Delta z) = \Delta z \cdot n\left(\cos\left[\arcsin\left\{ \frac{r \cdot r_{\max}}{n \cdot f} \right\} \right] - 1 \right). \tag{3.88}$$

Expansion into Zernike polynomials and exploiting their orthonormal properties (cf. subsection 2.2.1) gives

$$W(r, q, \Delta z) = \sum_i ZC_i \cdot Z_i(r, q) \tag{3.89}$$

$$W(r, q, \Delta z) \cdot Z_4(r, q) = \sum_i ZC_i \cdot Z_i(r, q) \cdot Z_4(r, q) \tag{3.90}$$

$$
\begin{aligned}
\int_0^1\int_0^{2p} W(r,q,\Delta z)\cdot Z_4(r,q)\, r\, d\, r dq &= \int_0^1\int_0^{2p}\sum_i ZC_i\cdot Z_i(r,q)\cdot Z_4(r,q)\, r\, d\, r dq \\
&= \sum_i ZC_i \int_0^1\int_0^{2p} Z_i(r,q)\cdot Z_4(r,q)\, r\, d\, r dq \qquad (3.91)\\
&= \sum_i ZC_i\cdot d_{i4} = ZC_4
\end{aligned}
$$

where d is the Kronecker delta. Integrating the left hand side of Eq. (3.91) after inserting the numerical value of $W(r,q,Dz)= c_0\cdot Dt_{transit}$ yields directly the value of ZC_4 expected for a particular position shift Dz of the QPS. The coefficient ZC_4 should change linearly as a function of QPS position with a slope (dZC_4/dz) that can be obtained by integrating the left hand side Eq. (3.91) without inserting a numerical value for $W(r,q,Dz)$

$$
-0.0998921\cdot\Delta z = ZC_4\,. \qquad (3.92)
$$

Comparison of the theoretical estimate and the measurement

The theoretical estimate for (dZC_4/dz) Eq. (3.92) can be compared to the fit to the actual experimental data, which provides a slope value $dZC_4/dz = -0.0968\pm0.0029$ (Figure 3.8). The fit value and its error were obtained following a weighted fit procedure [Taylor 1997]. For calculating the error the positioning inaccuracy of the mirror sample was taken into account (Figure 3.5). Real measurement and theoretical estimate are in good agreement (deviation 3%).

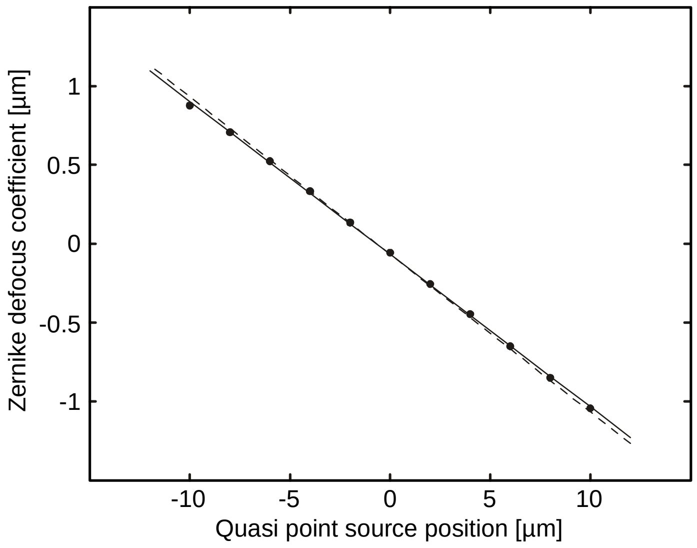

Figure 3.8: Measurement of the Zernike defocus coefficient ZC_4 as function of QPS position. Positive values of the QPS position are below the original focus. The dashed line depicts the theoretical estimate (slope: –0.0999). The solid line corresponds to a weighted fit to the data (slope: –0.0968±0.0029).

3.1.2 Astigmatism with a Mirror Sample

To induce an aberration that is of higher order than defocus, for example astigmatism, a standard glass cover slip (BK7, 180 µm thick) was inserted between the reflecting sample and the objective lens with its surface normal tilted away from the OA (angle ≈ 15°). A glass cover slip is a plane-parallel plate. Thus a light ray incident on such a plate will only be shifted laterally but keep its direction after transmission. The amount of lateral shift depends on plate thickness *T*, the angle of incidence a, and on the ratio of the refractive indices n_1 and n_2 (Figure 3.9). Using basic trigonometry and Snell's law yields the amount of parallel shift *s*

$$\left.\begin{array}{rcl} s &=& d_1 \sin(a - b) \\ d_1 &=& \dfrac{T}{\cos b} \\ b &=& \dfrac{n_1}{n_2}\arcsin a \end{array}\right\} \quad\Rightarrow\quad s = \frac{T \sin\left(a - \arcsin\left[\dfrac{n_1}{n_2}\sin a\right]\right)}{\cos\left(\arcsin\left[\dfrac{n_1}{n_2}\sin a\right]\right)}. \tag{3.93}$$

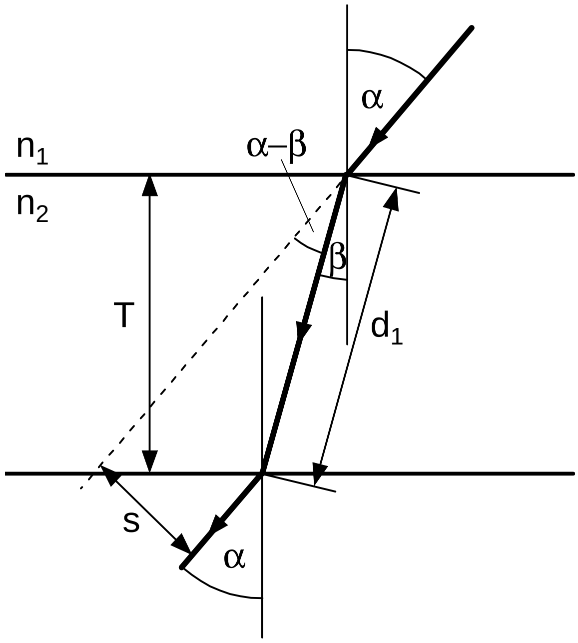

Figure 3.9: The parallel shift of a light ray incident on a plane-parallel glass plate.

If the glass plate is perpendicular to the OA only spherical aberration results. All light rays converging with the same angle from the OA experience the same shifts. The plate thus shifts the focus away from the objective down the OA (Figure 3.11 b), but it does so differently depending on the angles of the rays from the OA. For each angle from the OA there is a different focus position, but all these shifted foci are located on the OA. This changes if the plate, i.e. its surface normal, is tilted away from the OA. For an incident light cone the shifts for rays of equal angular aperture will be different from each other and an additional shift perpendicular to the OA is the result.

If a cross-section along intersection line 1 is regarded (Figure 3.10), an additional lateral shift of the focus position away from the OA becomes visible (Figure 3.11 a). This lateral shift is different for the foci of rays 1 and 2 and rays 3 and 4, respectively. This difference in foci shifts is coma. In a cross-section along intersection line 2 (Figure 3.10), there is only a shift down the OA (Figure 3.11 b). Again the shift is different for the foci of rays 3 and 4 and rays 1 and 2, respectively. This difference in foci shifts is astigmatism.

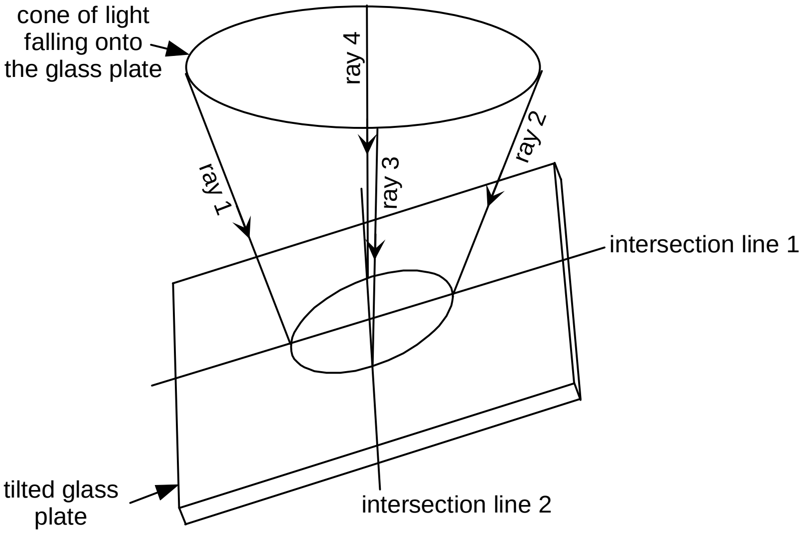

Figure 3.10: A cone of light incident on a tilted plane-parallel glass plate.

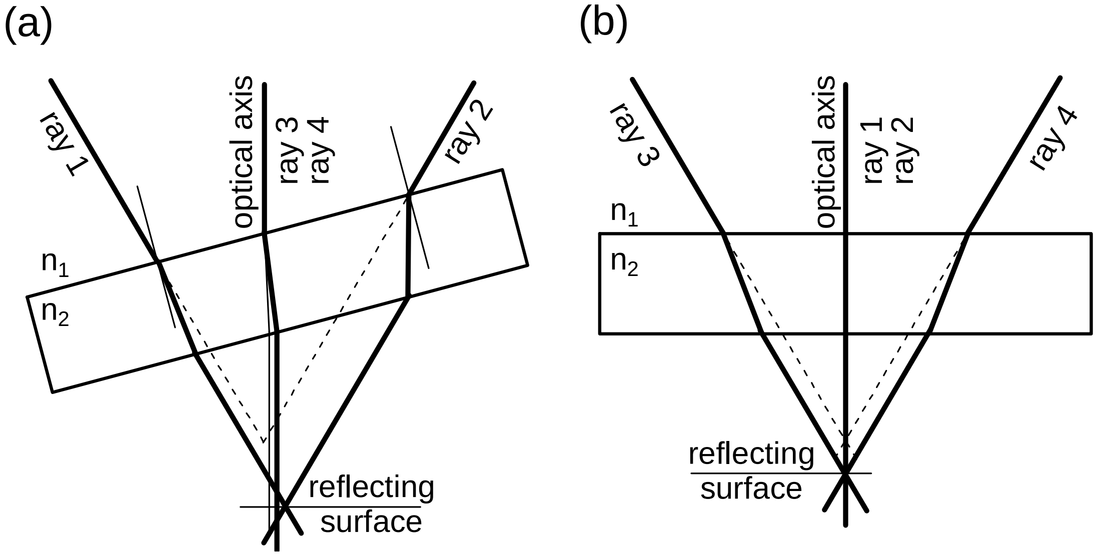

Figure 3.11: Schematic for the different foci locations of rays of equal angular aperture as depicted in Figure 3.10. (a) illustrates that, in addition to the focus shift down the OA an additional lateral shift of the focus occurs. (b) shows that in the cross-section perpendicular to (a) there is only a shift down the OA. The focus for rays 3 and 4 experiences a different shift laterally and a different shift down the OA than the focus of rays 1 and 2. These differences are coma and astigmatism, respectively. The symmetry with regard to the OA in case of a double pass (a mirror as a sample) is conserved whereas it breaks for a single pass through the glass plate (a scattering sample).

Deriving a theoretical estimate for the astigmatism coefficient

A theoretical estimate in this case was derived starting once again from a point on the OA, the focus. The lenslet array is situated in the BFP of the objective as in subsection 3.1.1, since this is the plane conjugate to the CCD sensor plane (cf. subsection 2.4.3). Different from subsection 3.1.1 now 3 spatial dimensions are considered.

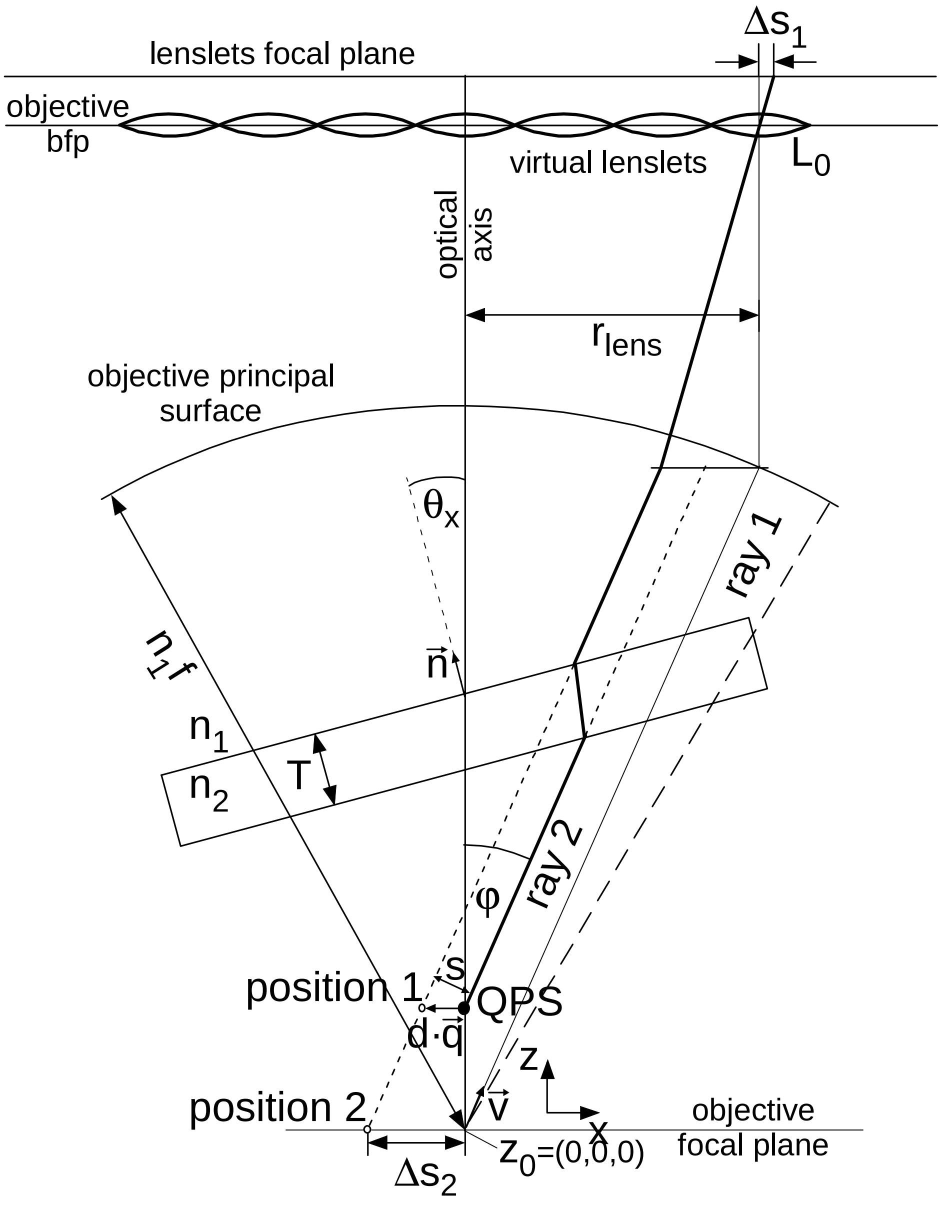

Figure 3.12: Schematic of the basic geometry for the derivation of the theoretical expectation for astigmatism induced by a plane-parallel glass plate. (Details see text).

The polar angle q and the distance $r_{lens} = \sqrt{x^2 + y^2}$ to the OA of each lenslet unambiguously describe the lenslet in the BFP of the objective. It is assumed that each lenslet is hit by exactly one ray, if the ray starts in the focus. Each of these rays is then unambiguous. For a certain lens, for example lens L_0 in Figure 3.12, this unambiguous ray (ray 1) is oriented along the unit vector $\vec{\mathrm{v}}$. The components of $\vec{\mathrm{v}}$ are given by

$$\vec{\mathrm{v}} = \frac{1}{n_1 \cdot f} \begin{pmatrix} r_{lens} \cdot \cos q \\ r_{lens} \cdot \sin q \\ \sqrt{n_1^2 \cdot f^2 - r_{lens}^2} \end{pmatrix}. \tag{3.94}$$

Here, the parameter n_1 is the index of refraction of the immersion medium. For a QPS situated on the OA above the original focus, ray 2, which is parallel to ray 1, will hit lens L_0. If in addition a plane-parallel glass plate is inserted between point source and objective with its surface normal $\vec{\mathrm{n}}$ slightly tilted away from the OA, i.e. with an angle q_x, ray 2 will be parallel shifted by an amount *s*. This shift takes place in the plane that is spread out by vectors $\vec{\mathrm{v}}$ and $\vec{\mathrm{n}}$, the plane-of-incidence. The amount of the parallel shift in that plane can be calculated applying Eq. (3.93) (the angle of incidence *a* is obtained via the scalar product of $\vec{\mathrm{v}}$ and $\vec{\mathrm{n}}$). To obtain the projection of the parallel shift s onto the xy-plane, at first the corresponding unit vector $\vec{\mathrm{q}}$ is determined:

This vector has to be a linear combination of the vectors $\vec{\mathrm{v}}$ and $\vec{\mathrm{n}}$ and its z-component has to be zero. Thus

$$\begin{gathered} \mathrm{q}_z = 0 \quad \text{and} \quad \vec{\mathrm{q}} = a \cdot \vec{\mathrm{v}} + b \cdot \vec{\mathrm{n}} \\ 0 = a \cdot \mathrm{v}_z + b \cdot \mathrm{n}_z \Rightarrow b = -a \cdot {}^{\mathrm{v}_z}\!/\!{}_{\mathrm{n}_z} \end{gathered} \tag{3.95}$$

$$\vec{\mathrm{q}} = a \cdot \left(\vec{\mathrm{v}} - \frac{\mathrm{v_z}}{\mathrm{n_z}} \vec{\mathrm{n}} \right). \tag{3.96}$$

Since $\vec{\mathrm{q}}$ is a unit vector the parameter *a* is the normalizing constant. Taking the orientation of $\vec{\mathrm{q}}$ due to the term in brackets in Eq. (3.96) into account, it becomes clear that the normalizing constant *a* has to have a negative sign (cf. Figure 3.12).

With $\vec{\mathrm{q}}$ (Eq. (3.96)) the orientation of the projection of the parallel shift of ray 2 in the xy-plane is known. The absolute value *d* of this projection can be determined using

$$\frac{s}{d \cdot |\vec{\mathrm{q}}|} = \cos j = \vec{\mathrm{v}} \cdot \begin{pmatrix} 0 \\ 0 \\ 1 \end{pmatrix} \quad \Rightarrow \quad d = \frac{s}{\mathrm{v}_z}. \tag{3.97}$$

Thus ray 2 is shifted parallel in the plane-of-incidence and parallel to the xy-plane along a shifting vector given by $d \cdot \vec{\mathrm{q}}$. That means that the QPS is virtually shifted to position 1, which has the coordinates

$$\begin{pmatrix} \mathrm{ps1}_x \\ \mathrm{ps1}_y \\ \mathrm{ps1}_z \end{pmatrix} = \begin{pmatrix} \mathrm{QPS}_x \\ \mathrm{QPS}_y \\ \mathrm{QPS1}_z \end{pmatrix} + \frac{s}{\mathrm{v}_z} \cdot \vec{\mathrm{q}} \, . \tag{3.98}$$

From the point of view of lens L_0, ray 2 appears to come from position 1. A shift Δs_1 of the diffraction spot in the focal plane of lens L_0 away from the lenslet center is the result (Figure 3.12). This shift is larger than the shift caused by ray 2 without the glass plate. The value of Δs_1 is, considering the magnification of the optical system, equal to $-\Delta s_2$, the projection of position 1 on the focal plane. The projection Δs_2 can be determined by calculating the coordinates of position 2 (cf. Figure 3.13):

$$\text{position 2} = \text{position 1} - \vec{\mathrm{u}} \, . \tag{3.99}$$

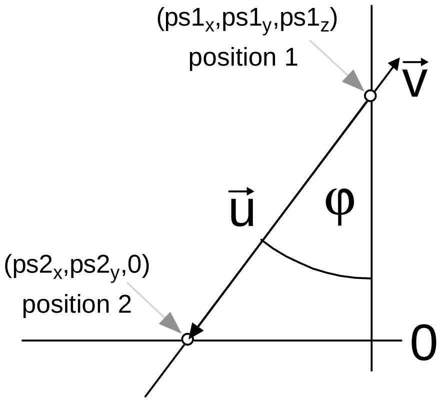

Figure 3.13: Calculating the coordinates of position 2 of Figure 3.12.

The result is given by

$$\frac{\mathrm{ps1_z}}{|\vec{\mathrm{u}}|} = \cos j = \vec{\mathrm{v}} \cdot \begin{pmatrix} 0 \\ 0 \\ 1 \end{pmatrix} \quad \Rightarrow \quad |\vec{\mathrm{u}}| = \frac{\mathrm{ps1_z}}{\mathrm{v_z}} \tag{3.100}$$

$$\begin{pmatrix} \mathrm{ps2_x} \\ \mathrm{ps2_y} \\ 0 \end{pmatrix} = \begin{pmatrix} \mathrm{ps1_x} \\ \mathrm{ps1_y} \\ \mathrm{ps1_z} \end{pmatrix} - \frac{\mathrm{ps1_z}}{\mathrm{v_z}} \vec{\mathrm{v}} \, . \tag{3.101}$$

For a QPS position the above calculations can be performed for each lenslet in the BFP, thereby determining all local wave-front slopes at the positions of the lenslets. Hence, the wave-front can be reconstructed following the same procedure as described in subsection 3.1.1.

Comparison of the theoretical estimate and the measurement

In case of a mirror sample rays that are symmetrical to the OA upon incidence keep this symmetry upon reflection (Figure 3.11). This is the reason that in case of a mirror no coma coefficient (ZC_7) is present (Figure 3.14). The quantity for the Zernike astigmatism coefficient (ZC_6) depends on the differences of foci shifts down the OA for different rays. For a mirror as a sample the parallel shifts are experienced twice. Thus the Zernike astigmatism coefficient (ZC_6) obtained with the above described calculation for a QPS has to be doubled.

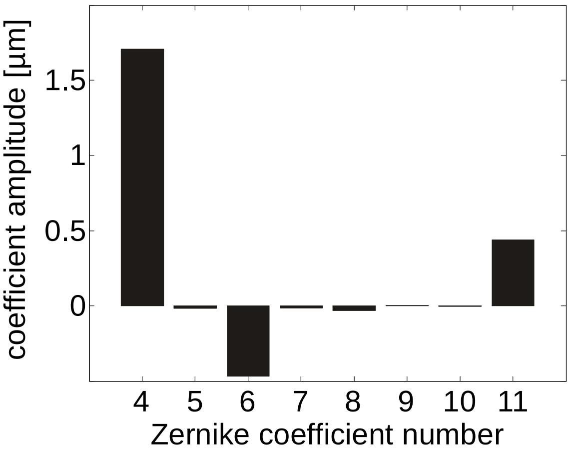

Figure 3.14: Typical example of Zernike coefficients number 4-11 for a tilted glass plate with a mirror as a sample positioned 20 mm below the original focus. Defocus, astigmatism and spherical aberration occur.

If the glass plate position is changed, but its tilt angle is kept constant, the parallel shifts of all rays are unchanged. ZC_6 should thus not change as a function of QPS position (Figure 3.15 b). To test whether this is really the case, a series of measurements for different QPS positions z (starting with the mirror from 20 µm below the original focus to 37.5 µm below the original focus in steps of 5 µm) was performed. The coefficient ZC_6 does, as expected, not change with QPS position. The mean measured value was (–0.4645±0.0013) µm, compared to the theoretical estimate ZC_6=–0.4651 µm. The deviation is smaller than 1%. Different from this the defocus coefficient should change as a function of QPS position. The measurement of the slope (dZC_4/dz) was (–0.096±0.001) (Figure 3.15 a) whereas the expected value was –0.0998. This is a deviation of less than 4%. The error for the measured slope was, in case of defocus, calculated using the standard procedure for fitting a straight line to data [Taylor 1997]. In case of ZC_6 the error is the standard deviation of the measurements.

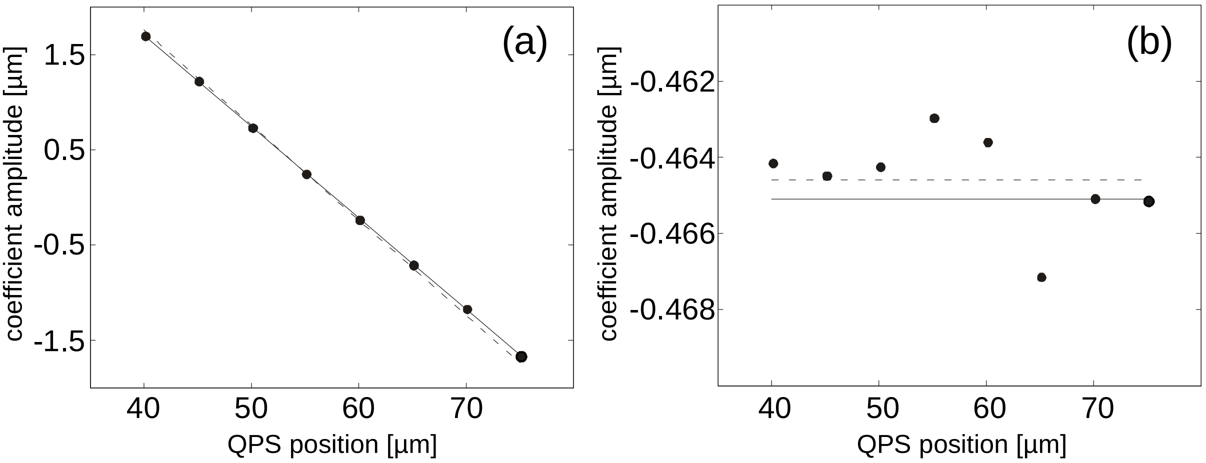

Figure 3.15: Zernike defocus coefficient ZC_4 as a function of QPS position (a). The solid line is a fit to the measured data points. The dashed line corresponds to the theoretical slope expectation. The astigmatism coefficient ZC_6 does not vary with QPS position (b). Again the solid line is a fit to the measured data and the dashed line is the theoretical estimate.

3.2 Experiments with Scattering Samples

3.2.1 Scattering Samples

The idea of CGWS is to measure wave-fronts using only light that was backscattered from the focal region within a scattering sample. To test the performance of the setup it was, therefore, necessary to produce phantoms of known scattering properties. This was achieved by using scattering beads (polystyrene beads from Polysciences Inc.) embedded in agarose (2%, high melting, Sigma A3768). Their scattering characteristics were determined using Mie's theory [Mie 1908] (cf. section 2.3).

First tests were made with 992 nm diameter beads. Their scattering behavior leads to a very inhomogeneous illumination of the BFP of the objective, which appears to be due to polarization effects. As explained in subsection 2.3.1, there is the possibility that the incident and the scattered light form a scattering plane which is parallel, perpendicular or a sum of both with respect to the original polarization direction of the incident light (Figure 3.16). For any given scattering plane the resulting light intensity of the scattered light can be split into components with perpendicular and parallel orientation (cf. subsection 2.3.1). The objective used has a NA of 0.9, corresponding to a maximum aperture angle of ≈ 42.6°, which results in a maximum scattering angle of about 85°. Taking the ratio of the intensities for different polarizations into account (in the case of the 992 nm diameter beads Figure 3.17 a), it becomes clear that the intensities are very different for the range of angles gathered by the objective and result in a inhomogeneity of backscattered light in the BFP. Different from that the corresponding intensities for 112 nm diameter beads diverge less from each other over the majority of the detectable angular range (Figure 3.17 b). Thus their scattering behavior is less critical and the illumination intensity is more regular. Due to this fact mainly, beads with a diameter of 112 nm were used in the scattering samples.

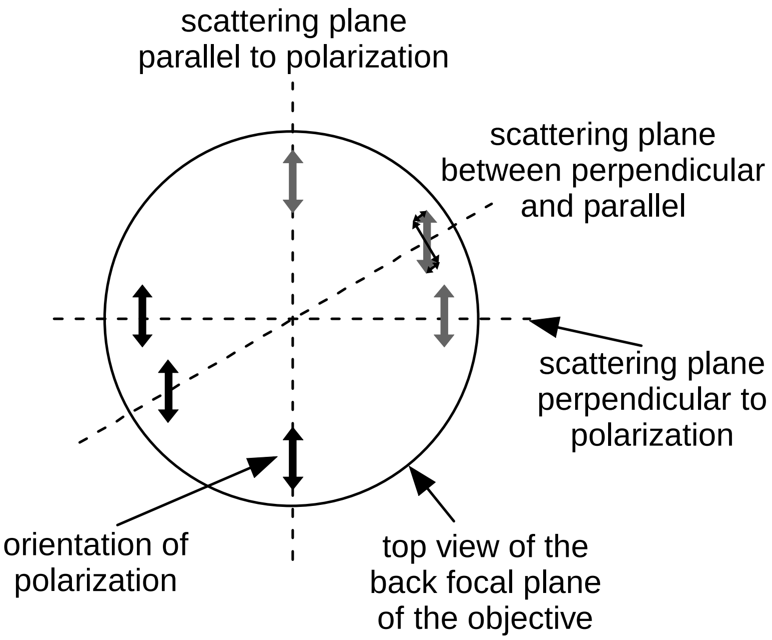

Figure 3.16: Polarization considerations for the intensity of light of parallel and perpendicular orientation with respect to the scattering plane. The direction of the bold arrows in the BFP of the objective corresponds to the original polarization of the incident light. Bold black arrows depict incoming, gray ones scattered light. The light intensity of the scattered light resulting for any scattering plane can be expressed in terms of a sum of two fractions with perpendicular and parallel orientation with respect to the plane. An example is illustrated for scattered light of a scattering plane, which is oriented between perpendicular and parallel direction. It can be seen that the fraction of light with perpendicular polarization orientation must be stronger weighted than the fraction with parallel polarization orientation. Since the amplitude for the orientations is dependent on the bead size according to Mie theory, the intensity in the BFP can look very different for different bead diameters.

To check the scattering length of the samples produced, two methods were used. The first was to measure the transmission of thin sample slices with a Cary 500 Scan spectrometer (Varian, Inc.). From the result the MFP can be determined using the Lambert-Beer law. The second method needed the addition of fluorescent markers to the sample because they allow for the measurement of the scattering length, i.e. the MFP, with two-photon induced fluorescence microscopy. Since the fluorescence is proportional to the square of the average excitation laser power $\overline{P}^{2}_{illu\min ation}$ (cf. Eq. (2.1)) the corresponding signal falls off with depth z following Lambert-Beer's law for the two-photon case

$$Fluorescence \propto \overline{P}^{2}_{\text{illuminati on}} \propto \overline{P}_{0}^{2} \exp\left(-2z/MFP\right). \qquad (3.102)$$

This equation can be solved for MFP, which gives the halved MFP for the one photon case.

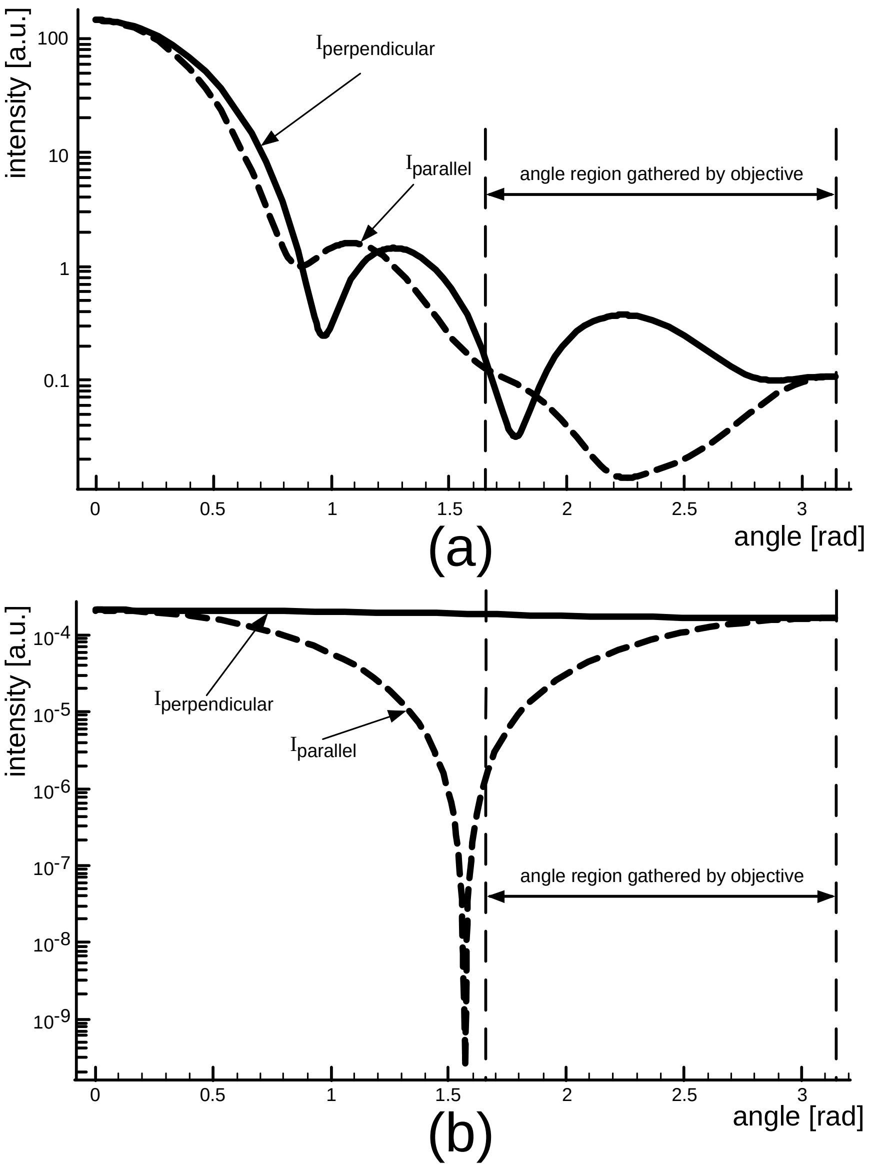

Figure 3.17: The two different intensities (cf. subsection 2.3.1) for light scattered by a sphere (in this case with a diameter of 992 nm, (a), and a diameter of 112 nm, (b)). For forward scattering the angle is zero. In depiction (b) the difference for the both, the parallel and the perpendicular intensity, is much smaller over the angular region that can be detected by the objective used. The intensity of the BFP due to backscattered light is more uniform than for 992 nm diameter beads.

Finally a scattering sample consisting mainly of 112 nm beads at a concentration of $\approx 9.8 \cdot 10^{13}$ beads/ml was used. Yellow-green fluorescent marker beads (2.5 μm, Molecular Probes Inc.) were added at a concentration of $\approx 2.1 \cdot 10^{7}$ beads/ml. According to Mie theory their scattering cross-section is $\approx 2.1 \cdot 10^{7}$ nm^2 compared to ≈ 21 nm^2 for the 112 nm beads. This has to be taken into account for the calculation of the anisotropy factor g.

The thin slices for the measurement with the Cary 500 were prepared by filling a small portion of the sample in liquid state between two microscope slides separated by a cover slip. A series of measurements to find out the cover slip thickness resulted in a value of (185.7±2.7) μm. The measured transmission value for this slice thickness at a wavelength of 915 nm was (66±3)%. The corresponding MFP is (447±49) μm. A practical difficulty with the measurements of such thin slices is that they dry up very fast. This was the motivation to measure the scattering length with fluorescent marker beads. While the illuminating laser power was kept constant two-photon absorption induced fluorescence of the marker beads was recorded at different depth positions in the sample. The fluorescence intensity was then plotted as a function of sample depth (Figure 3.18) and a Lambert-Beer function $I = I_0 \cdot \exp\left(-z / MFP_{2-photon}\right)$ was fitted to the resulting data. Here again the MATLAB functions *nlinfit* and *nlparci* were used to calculate the fit and the error. The MFP found was (404±18) µm.

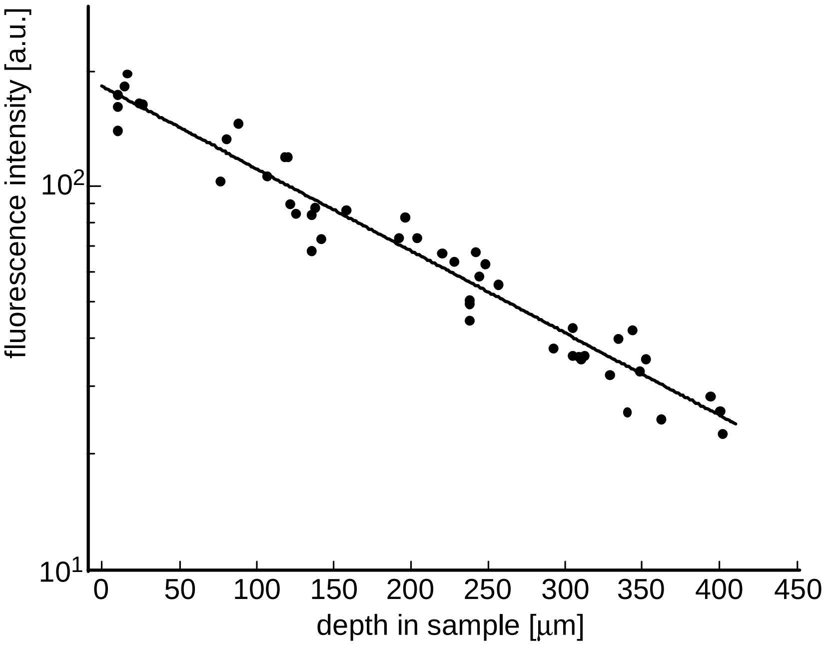

Figure 3.18: Fluorescence intensities of single fluorescence beads in various depths in the scattering sample.

A theoretical estimate can be obtained using Mie's theory Eq. (2.40)

$$mfp = \frac{1}{s_{112\,nm\,beads} \cdot n_{112\,nm\,beads} + s_{992\,nm\,beads} \cdot n_{992\,nm\,beads}}. \qquad (3.103)$$

The result was 399 µm. Thus, the MFP used in all further calculations involving the scattering samples was assumed to be 400 µm.

Since spherical particles were used as scatterers, the asymmetry parameter g is independent of polarization [Bohren and Huffman 1998] and Eq. (2.43) can be used to determine the anisotropy.

Taking the different influence of the two different bead types on the MFP into account the anisotropy for the sample can be calculated as follows

$$g = 0.78 \cdot g_{112\,nm} + 0.22 \cdot g_{2500\,nm} \tag{3.104}$$

resulting in a g of 0.24.

Concerning the overall index of refraction of the scattering sample it is of importance that the index of refraction for agarose is only slightly different from that of water (1.334 instead of 1.33). The concentration of 112 nm polystyrene beads corresponds to a volume fraction in the scattering sample of approximately 7.2 %. For the 2.5 μm beads the volume fraction is $2 \cdot 10^{-5}$ and hence was neglected. At that volume fraction the index of refraction of the 112 nm beads (n=1.56) causes a change of less than 1.5% for the index of refraction of the scattering sample.

3.2.2 Defocus with a Scattering Sample

Again the first aberration tried was defocus. Different from the mirror (cf. subsection 3.1.1) moving the sample does not actually induce defocus. The reason is, that the scattering sample is homogeneous. Moving the sample up and down does, therefore, not change the average backscattered wave-front.

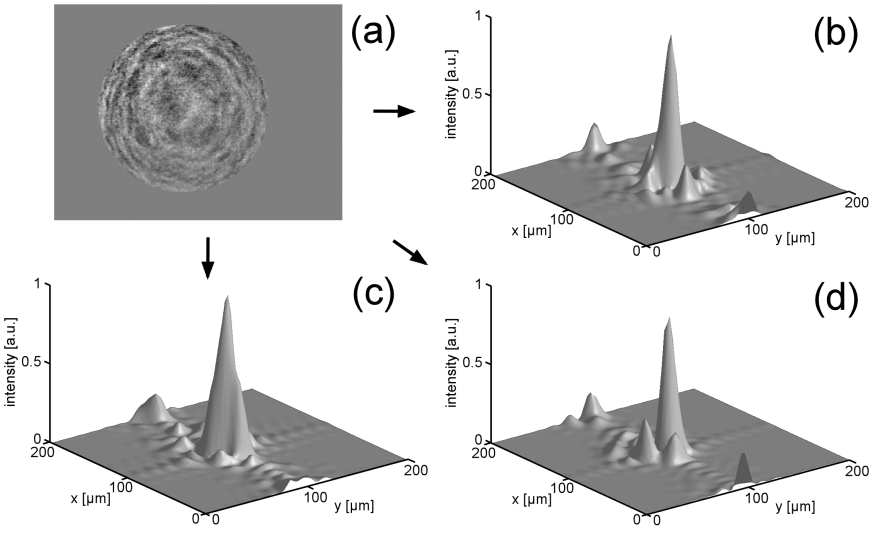

Figure 3.19: The real part of the complex amplitude of the electric field across the CCD chip for the scattering sample (a). Speckle, that are clearly visible result in inhomogeneous diffraction patterns after numerical propagation through individual lenslets by means of a FFT (b), (c) and (d). Such diffraction patterns makes a centroid finding algorithm as method to locate the diffraction peak positions unsuitable. The small elevations at the ends of the parallel to the x-axis through the center peaks are due to the interlaced operation of the camera resulting in an alternating intensity pattern in the recorded images.

To induce defocus in this case the CG was shifted by changes of the reference arm length. Increasing the optical path length in the reference arm results in a position change of the CG away from the objective while a reduction of the reference arm path length moves the CG closer to the objective. For the defocus experiment the CG position was shifted from 10 μm above to 10 μm below the original objective focus in steps of 1 μm and the focal plane of the objective was located one MFP below the scattering sample surface. For each CG position 600 image quadruplets for the PSI algorithm were taken at 24 different sample positions (shifts of 0.1 μm) to reduce speckle noise.

The speckle noise and its effect on the shape of the diffraction peaks of the virtual lenslets (Figure 3.19) are the main reason that a centroid finding algorithm, which would otherwise be easier and faster to execute, rarely produces sensible results (as was confirmed by practical tests) and therefore was not used.

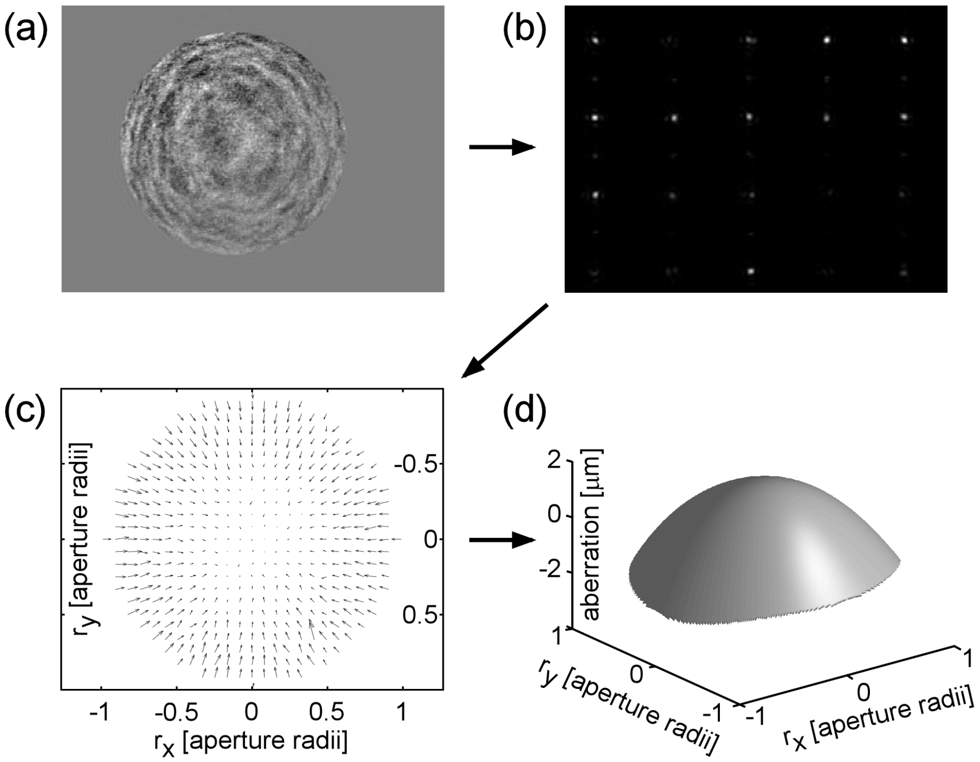

Figure 3.20: CGWS scheme for a scattering sample (cf.Figure 3.3). Real part (a) of the complex amplitude for a CG position 10 mm beneath the original focus, which was one MFP below the sample surface. Numerical propagation through the virtual lenslets via Fourier transformation leads to virtual diffraction spots. A zoom is depicted in (b). This was done for 24 different sample positions to reduce speckle noise. Gradient information was extracted for each position by fitting the diffraction spot positions and comparing them to the lenslet centers. Their average is depicted in (c). For all 24 sample positions Zernike coefficients were determined. To reconstruct the wavefront (d) the mean for each Zernike coefficient was calculated.

For each of the 24 slightly different sample positions the diffraction pattern peak shifts were determined by comparing the peak positions to the lenslet centers. In order to obtain the 20 Zernike coefficients used, a fit using the pseudo-inverse (cf. subsection 2.2.1) was performed each time. The resulting 24 different values for each Zernike coefficient were averaged for each coefficient separately to obtain the final set to be used for wave-front reconstruction. The measurement error for each coefficient was calculated as standard deviation of its 24 measurements (Figure 3.20). The effect of averaging can be studied in Figure 3.21.

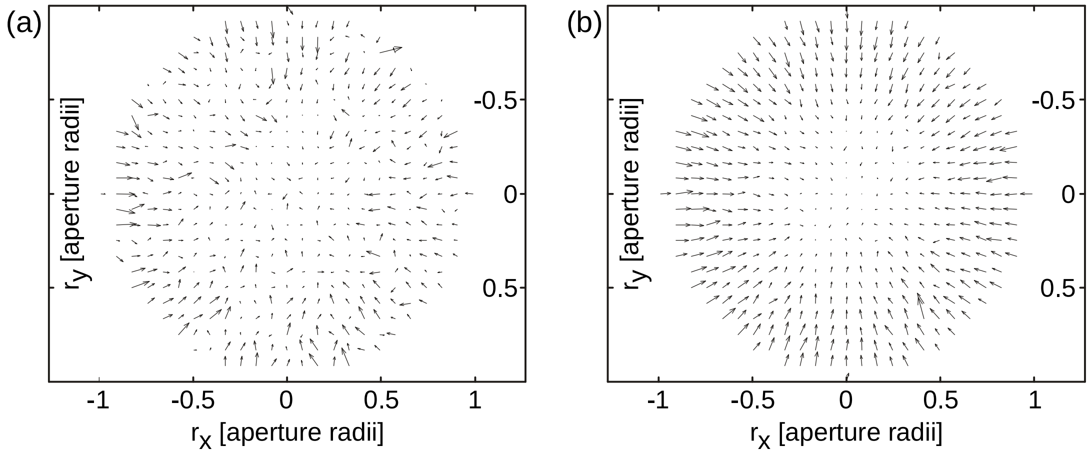

Figure 3.21: Peak shifts in a scattering sample (400 mm MFP, focus position one MFP beneath sample surface) for a CG position 10 mm below the original focus. Single instance (a). Average of 24 different measurements with slightly different sample positions to allow averaging out speckle (b).

Deriving a theoretical estimate for the defocus coefficient

A theoretical estimate was obtained by performing a simulation that was implemented in MATLAB. Random numbers were generated to simulate coordinates of scattering beads at positions within the geometrical volume of the illumination cone. It was assumed that each one of those beads acts like a point scatterer and that for each bead and each lenslet of the virtual lenslet array there exists an unambiguous ray that starts at the bead and hits the lenslet at its center (Figure 3.22). Since defocus is a symmetrical aberration only lenslets on the x-axis need to be considered. Nevertheless the entire 3-dimensional cone volume has to be taken into account and 3D bead coordinates have to be used. The distance Δs_1 in Figure 3.22 from the lenslet center to the position where such a ray hits the focal plane of a lenslet at position L_1 is proportional to the local slope of the wave-front. The shift Δs_1 is equal to the negative projection ($-\Delta s_2$) of the bead position (b_1) on the focal plane times the magnification of the optical system. In the simulation these projections of the bead positions onto the focal plane were determined first before they were converted to the shifts in the focal plane of the lenslets. Since there are many beads present, each “produces” its own shift Δs_1^* for each lenslet and its own projection Δs_2^* on the focal plane of the objective. An average projection Δs_2 was determined as weighted average for each lenslet. This weighted average was used to determine an average Δs_1, which is proportional to the local wave-front slope from which the wave-front can be reconstructed. The quantity for each weight in the weighted average calculation was determined according to the distance of each bead to the CG position, the light intensity at the position of each bead and the depth of each bead in the sample.

Due to the depth of a bead in the sample, the light travels a certain distance within the scattering sample on its way from the bead to the lenslet. On this way it will be attenuated according to Lambert-Beer’s law. The weight that takes this into account is given by

$$wgt_{LB} = \exp\left(-\frac{1.33 \cdot \frac{z(i)}{\cos\left(\arctan\left(\frac{d_{lens}}{n \cdot f}\right)\right)}}{400} \right), \tag{3.105}$$

where z(i) is the depth of the ith bead in the sample, d_{lens} is the lenslet distance from the z-axis and n·f is the focal length of the objective in the sample (with n, the refractive index of the sample) (Figure 3.22). The assumed scattering length was 400 µm. The principal surface of the objective was assumed to be planar (paraxial approximation).

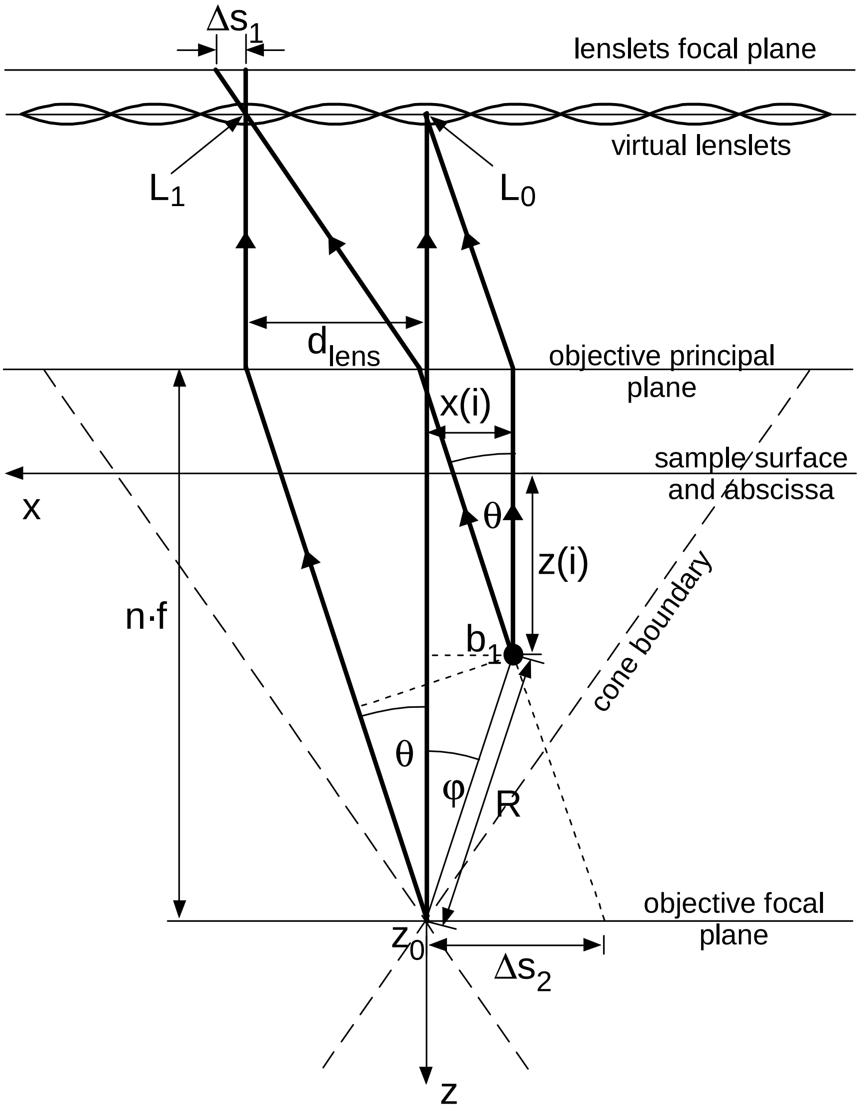

Figure 3.22: Simulation geometry to obtain a theoretical estimate for the Zernike defocus coefficient in the case of a scattering sample.

A bead closer to the focus scatters more light back than a bead far away from the focus where the light intensity is considerable lower. This is corrected by the intensity weight. The intensity in an illumination cone can be expressed as [Saleh and Teich 1991]

$$I(r,z) \equiv wgt_{\text{int}} = \frac{2}{p \cdot w^2(z-z_0)} \exp\left[-\frac{z-z_0}{400}\right] \exp\left[-\frac{2r^2}{w^2(z-z_0)}\right]$$
$$\text{with} \tag{3.106}$$
$$w(z) = w_0\sqrt{1+\left(\tfrac{z}{z_R}\right)^2}\ ;\ z_R = \frac{p\, w_0^2}{l}\ ;\ w_0 = \frac{l}{np \cdot \tan\left[\arcsin\left(\frac{NA}{n}\right)\right]}\,.$$

Here, z_0 is the focus position (400 µm), λ is the wavelength, $r^2=x^2+y^2$ is the distance of the bead from the z-axis and x, y ,z are the bead coordinates.

The last weight takes the distance of each bead to the CG position into account. The coherent signal falls off exponentially with interferometer arm length mismatch (cf. subsection 2.4.3). That means the higher the absolute value of the transit time difference between light that is backscattered from a bead and light that is backscattered from the CG, the lower the weight for the backscattered light from the bead. To determine the transit time difference for light backscattered from each bead the individual transit times are calculated. For a bead in the focus the light needs a time t_{01} to get there. To get out to a certain lenslet at position L_0 it needs a further time t_{02} (cf. Figure 3.22). In sum, a time $t_0=t_{01}+t_{02}$. For a bead b_1 the time for the light focused to reach the bead (inward time) is $t_{01}-R\cdot n/c$ (with R the distance of the bead to the focus and c the speed of light in vacuum). The transit time for the backscattered light from there to L_0 (outward time) is $t_{02} - R\frac{n}{c}\cos j$, hence altogether $t_1 = t_{01} + t_{02} - \frac{R\cdot n}{c} - \frac{R\cdot n\cdot\cos j}{c}$. For a lenslet at position L_1 the light for a bead in the focus needs the inward time t'_{01} and the outward time t_{02}. For a bead b_1 this becomes $t'_{01}-R\cdot n/c$ for inward time and $t_{02} - \frac{R\cdot n\cdot\cos(q-j)}{c}$ for the outward time (cf. Figure 3.22). In general the time difference with respect to the focus is given by

$$d\,t = t_1 - t_0 = -\frac{R\cdot n}{c}\left[1+\cos(q-j)\right]. \tag{3.107}$$

For $z\text{-}z_0<0$ dt has to be smaller than zero and for $z\text{-}z_0>0$ dt has to be larger than zero. Since only a lenslet row along the x-axis is considered with all y-coordinates equal to zero, the time difference Eq. (3.107) becomes

$$d\,t_b = sign\left[z(i)-z_0\right]\cdot\frac{n}{c}\cdot \left[\sqrt{x(i)^2+y(i)^2+\left(z(i)-z_0\right)^2}+\sqrt{x(i)^2+\left(z(i)-z_0\right)^2}\cdot\cos\left[\arctan\left(\frac{d_{lens}}{n\cdot f}\right)-\arctan\left(\frac{x(i)}{z(i)-z_0}\right)\right]\right]. \tag{3.108}$$

This transit time difference is compared to the transit time difference of the CG position $d\,t_{CG}$ and the weight, therefore, is

$$wgt_{CG} = \exp\left(-\frac{4\ln 2}{\left(100\cdot 10^{-15}\right)^2} \cdot \left(d\,t_b - d\,t_{CG}\right)^2 \right) \tag{3.109}$$

The mean projection Δs_2 for each lenslet is then calculated by

$$\Delta s_2 = \frac{\sum_i wgt_{LB,i} \cdot wgt_{\text{int},i} \cdot wgt_{CG,i} \cdot \Delta s_2^*}{\sum_i wgt_{LB,i} \cdot wgt_{\text{int},i} \cdot wgt_{CG,i}}\,. \tag{3.110}$$

Here *i* is the index of the beads. After computing the mean projections Δs_2, the resulting wave-front slopes over each lenslet can be calculated using Δs_1. With a nonlinear fit (MATLAB's *nlinfit*) of the derivative of the Zernike defocus polynomial to these data the defocus coefficient value was determined. In order to obtain an error estimate the simulation was repeated several times and the resulting shift positions were averaged. A somewhat surprising result of this simulation is that for different lenslets different volumina in the sample contribute to the signal (Figure 3.23). This should not pose a problem when an iterative wave-front correction algorithm is used, because the measured values for the defocus coefficient (ZC_4) deviate not that much from the values obtained from this simulation.

Comparison of the theoretical estimate and the measurement

If the ZC_4-amplitude is plotted as a function of the CG position *z* the slope (dZC_4/dz) for the simulation described above is equal to (–0.0998±0.0065). If a QPS is assumed only on the OA the simulation provides a slope (dZC_4/dz) of –0.0872. For reasons of comparability the simulation in subsection 3.1.2 was recoded to simulate the paraxial case. The curved principal surface of the objective (cf. Figure 3.12), therefore, was assumed to be planar. The modified simulation provided the same value –0.0872 as the simulation above. A third method, using the Newtonian form of the lens equation was used to verify this value. It will be described later. The actual measurement (CG position shifted from 10 μm above the original focus to 10 μm below the original focus in steps of 1 μm) showed a slope value of (-0.083±0.002) (Figure 3.24). A control experiment with distances of 0.5 μm instead of 0.1 μm for the 24 different sample positions for speckle averaging provided (–0.084±0.002). The probable reason for the discrepancy between measurement and the theoretical estimate is that the fitting algorithm used to determine the peak positions of the virtual SHS weighs backscattered light from regions closer to the focus more strongly (Figure 3.25).

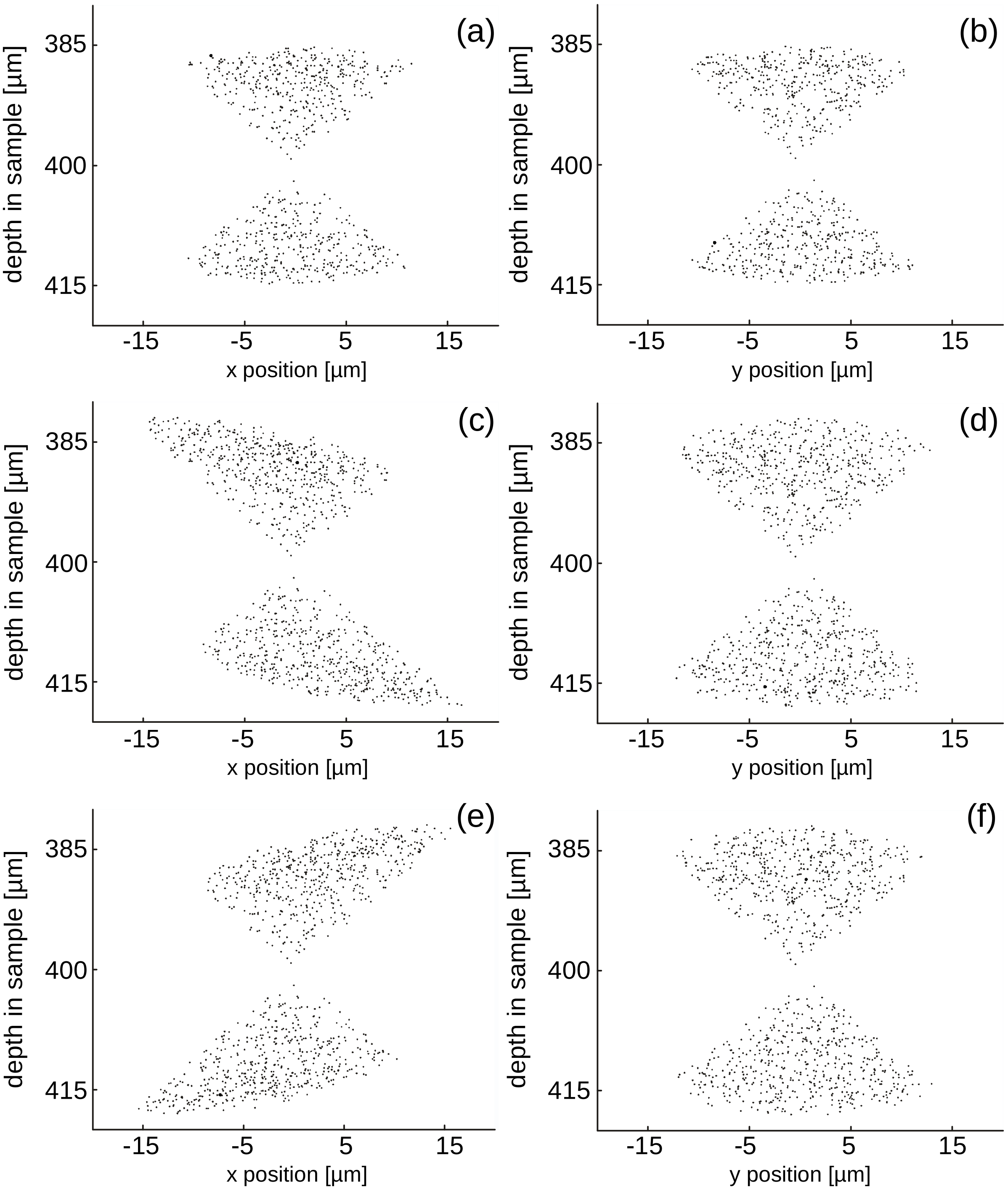

Figure 3.23: Projections of the bead volumina that, according to the simulation, contribute to the signal for individual lenslets. The left column corresponds to the projection onto the xz-plane whereas the right corresponds to the projection onto the yz-plane. The focus and the CG were situated in a sample depth of 400 mm. The first row (a) and (b) correspond to the lenslet, which is located on the OA. The second row (c) and (d) represents bead volumina for the lenslet with the x-coordinate 2340 mm and the last row (e) and (f) illustrates the same for the lenslet with x-coordinate -2340 mm.

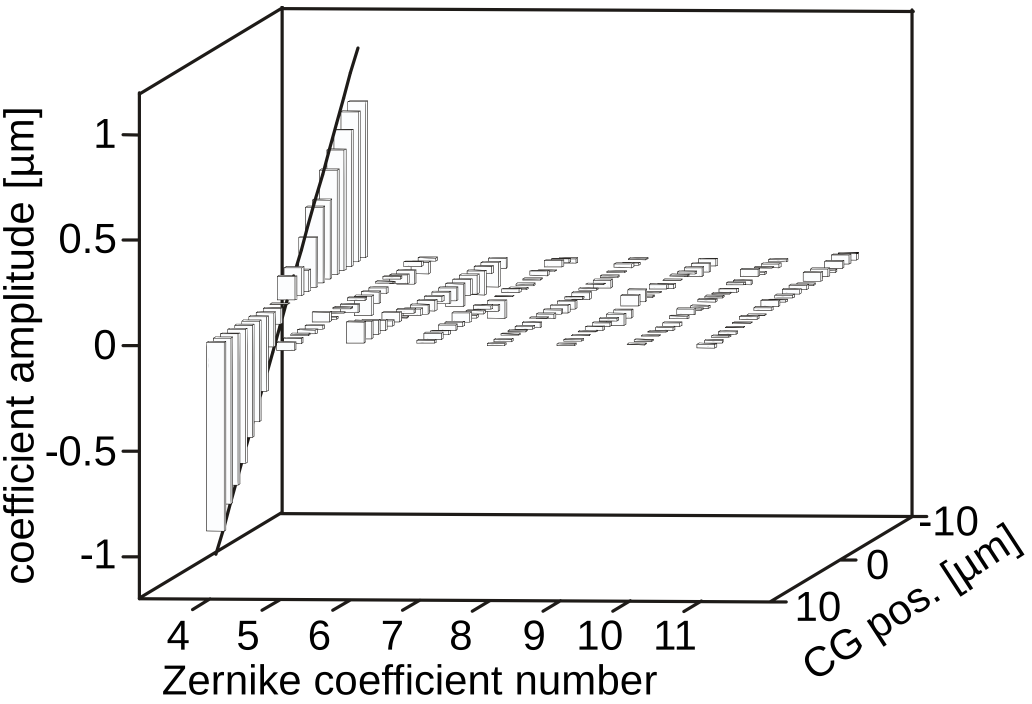

Figure 3.24: Zernike coefficients (ZC_4-ZC_{11}) as a function of CG position. Negative positions are for the CG between focus and objective. The solid line shows the theoretical expectation due to the described simulation. The deviation of the fit to the data compared to this expectation was 17%.

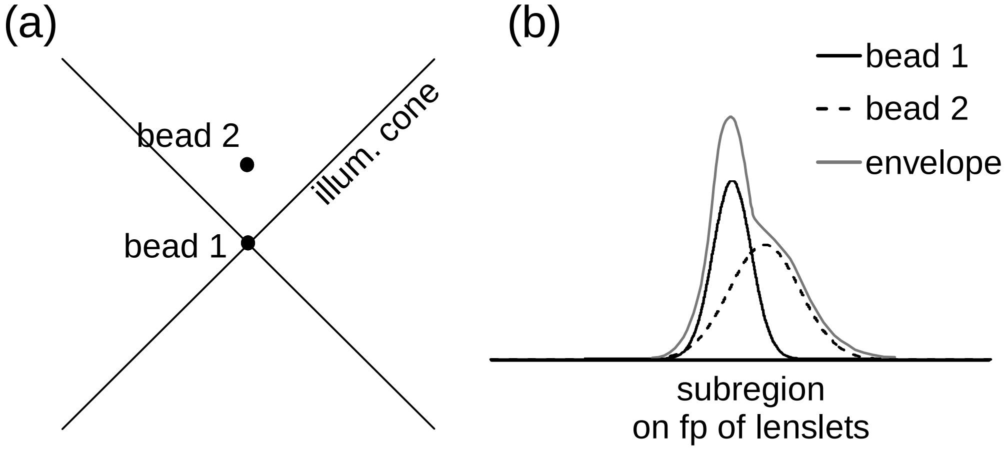

Figure 3.25: The probable reason for the deviation between the expected slope (dZC_4/dz) and the actual measurement is the manner how the fitting algorithm used finds the diffraction peaks. As mentioned in subsection 2.4.3 the fit was restricted to a small area around the focus. This was done because a larger region leads to problems in peak finding. The diffraction peak on the focal plane (fp) of a lenslet off the OA due to a bead in the focus (bead 1 in (a)) has a small width and large amplitude (solid Gaussian in (b)). The diffraction peak due to a bead further away from the focus (bead 2 in (a)) is wider and smaller in amplitude (dashed Gaussian in (b)). The resulting diffraction pattern in the sub region of the lenslet corresponds to the envelope of both (gray solid line in (b)), which is still narrow around its peak. If the region for peak finding is small the nonlinear fit to the data will be influenced only little by the data caused by bead 2. Thus the smaller the chosen region for peak finding the more position information of bead 2 gets lost. This is a problem to which attention has to be paid in future work.

Using the Newtonian form of the lens equation to derive a theoretical estimate for the defocus coefficient

Using the Newtonian form of the lens equation [Hecht 1990] confirms the paraxial result for the defocus coefficient behavior of the two simulations described earlier:

The optical setup can be considered in a simplification as an assembly of three lenses and a lenslet array (cf. Figure 3.26). The objective L_{OBJ}, the imaging lenses L_1 and L_2 that make the BFP of the objective and the lenslet array conjugates and a virtual lenslet array that mimics a SHS. A QPS is assumed to be located on the OA a distance ***e*** away from the original objective focus. In this case the Newtonian form of the lens equation for the individual lenses becomes

$$\begin{aligned} L_{OBJ}: \quad & e\,\Delta_1 = n\,f_0^2 \quad \Rightarrow \quad \Delta_1 = \frac{n\,f_0^2}{e} \\ L_1: \quad & \Delta_1\,\Delta_2 = f_1^2 \quad \Rightarrow \quad \Delta_2 = \frac{f_1^2}{\Delta_1} = \frac{f_1^2\,e}{n\,f_0^2} \\ L_2: \quad & \Delta_2\,\Delta_3 = f_2^2 \quad \Rightarrow \quad \Delta_3 = \frac{f_2^2}{\Delta_2} = \frac{f_2^2\cdot n\,f_0^2}{f_1^2\,e} \equiv R_C\,. \end{aligned} \tag{3.111}$$

Here, the parameter *n* is the refractive index of the immersion medium. As can be seen in Figure 3.26, Δ_3 is equal to the radius of curvature R_C of the wave-front at the position of the virtual SHS due to a QPS position shift ***e***. The AWF in this case is a spherical wave and can be approximated with the help of Pythagoras' theorem with the parameter d_k (Figure 3.27)

$$r_k^2 + (R_C - d_k)^2 = R_C^2 \quad \Rightarrow \quad d_{k_{1/2}} = R_C \pm \sqrt{R_C^2 - r_k^2}\,. \tag{3.112}$$

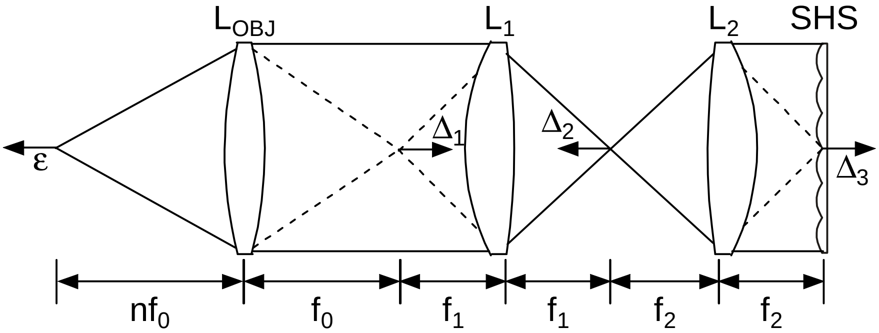

Figure 3.26: The crucial elements of the setup for calculating the expectation for the Zernike defocus coefficient. Using the Newtonian form of the lens equation yields the relation between D_3, the measured value of the radius of curvature at the virtual SHS and the focus shift e.

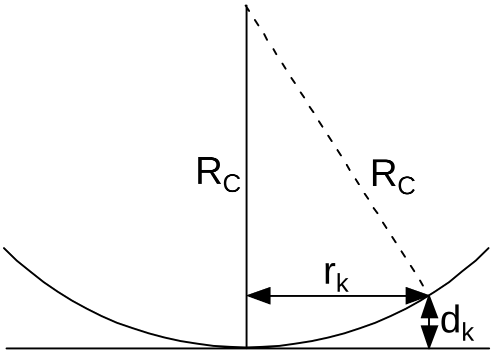

Figure 3.27: Using Pythagoras's theorem to describe the wave-front of a spherical wave resulting from defocus by means of the optical path length difference d_k to a planar wave-front.

The following consideration explains why in Eq. (3.112) the negative result is the one to use:

- If r_k equals zero it is obvious that d_k has to be equal to zero as well.
- If r_k equals the radius of curvature R_C, then d_k has to be equal to R_C as well.

Thus $d_k \le R_C$ and hence

$$d_k = R_C - \sqrt{R_C^2 - r_k^2}\ . \tag{3.113}$$

If the spatially extent of the SHS is small, i.e. the occurring r_k's are small in comparison to R_C then Eq. (3.113) can be Taylor expanded

$$\begin{aligned} d_k &\overset{\text{Taylor}}{=} R_C - R_C\left(1 - \frac{r_k^2}{2R_C^2}\right) + O(4) \\ &\Rightarrow\ d_k \cong \frac{r_k^2}{2R_C}\ . \end{aligned} \tag{3.114}$$

This expression corresponds to the Zernike defocus polynomial. As explained in section 2.2 the SHS measures the average slope, i.e. the gradient of the wave-front. Thus the derivatives of Eq. (3.114) and the derivative of the Zernike defocus polynomial can be compared in order to find the Zernike defocus coefficient ZC$_4$. To accomplish that d_k has to be mapped onto the unit circle

$$r_k \quad \to \quad r = \frac{r_k}{r_{\max}} \qquad \Rightarrow \qquad d_k = \frac{r^2 r_{\max}^2}{2R_C}\ . \tag{3.115}$$

Here, $r_{\max}$ means the maximum radius of the lenslet array, measured from the lenslet array center to the last lenslet that is illuminated. Coefficient comparison yields

$$\begin{gathered}\frac{\partial d_k}{\partial r} = \frac{\partial Z_4}{\partial r} \\ \frac{r \cdot r_{\max}^2}{R_C} = ZC_4 \cdot 4\sqrt{3} \cdot r \quad \Rightarrow \quad ZC_4 = \frac{r_{\max}^2}{4\sqrt{3} \cdot R_C}\,.\end{gathered} \tag{3.116}$$

If this is combined with the result of Eqs. (3.111) and the fact that in the setup used, the focal lengths f_1 and f_2 are the same, then ZC_4 becomes

$$ZC_4 = \frac{r_{\max}^2 \cdot e}{4\sqrt{3} \cdot f_0^2 \cdot n}\,. \tag{3.117}$$

Insertion of the parameters of the optical elements used yields a slope of the Zernike defocus coefficient ($dZC_4/d\varepsilon = -0.0872$) that is in agreement with the two simulations described above.

3.2.3 Astigmatism with a Scattering Sample

The high-order aberration that was used to test CGWS for a scattering sample was astigmatism. To induce astigmatism a glass cover slip (BK7, 180 μm thick) was inserted between objective lens and sample with the surface normal tilted away from the OA (≈ 15°). The focal plane of the objective was positioned 400 μm, i.e. 1 MFP, below the scattering sample surface. The measurement procedure was analogous to subsection 3.2.2. In the Zernike fit strong astigmatism $ZC_6=(-0.264\pm0.026)$ μm, coma $ZC_7=(0.327\pm0.027)$ μm and spherical aberration $ZC_{11}=(0.2\pm0.01)$ μm were found. Unlike uniform curvature (ZC_4), which leads to a change of focus position but not shape, these aberrations do lead to a distortion of the focus and need to be corrected for optimal imaging. Again, the effect of changing the CG position (from 14 μm to 24 μm below the original objective focus position in steps of 1 μm; averaging was done as above but with sample position shifts of 0.5 μm) was tested. Qualitatively the measurement confirmed that only ZC_4 changed systematically (slope: –0.073±0.003) (Figure 3.28). A theoretical estimate (-0.0998) was obtained with the simulation for a QPS (subsection 3.1.2). For astigmatism a constant value of $ZC_6=-0.233$ μm and for coma a constant value of $ZC_7=0.409$ μm is expected. Spherical aberration showed a systematical change (slope: -0.0042) in the simulation that could not be confirmed by the actual measurement. It must be stressed, that the theoretical estimates for this experiment were obtained with a simulation for a single point source (cf. subsection 3.1.2). Future work will have to include the derivation of a more appropriate simulation for this kind of experiment. The most probable reason for the deviation of the measured slope (dZC_4/dz) to the simulation of subsection 3.2.2 is the problem of the algorithm used to determine the diffraction peak positions (cf. Figure 3.25).

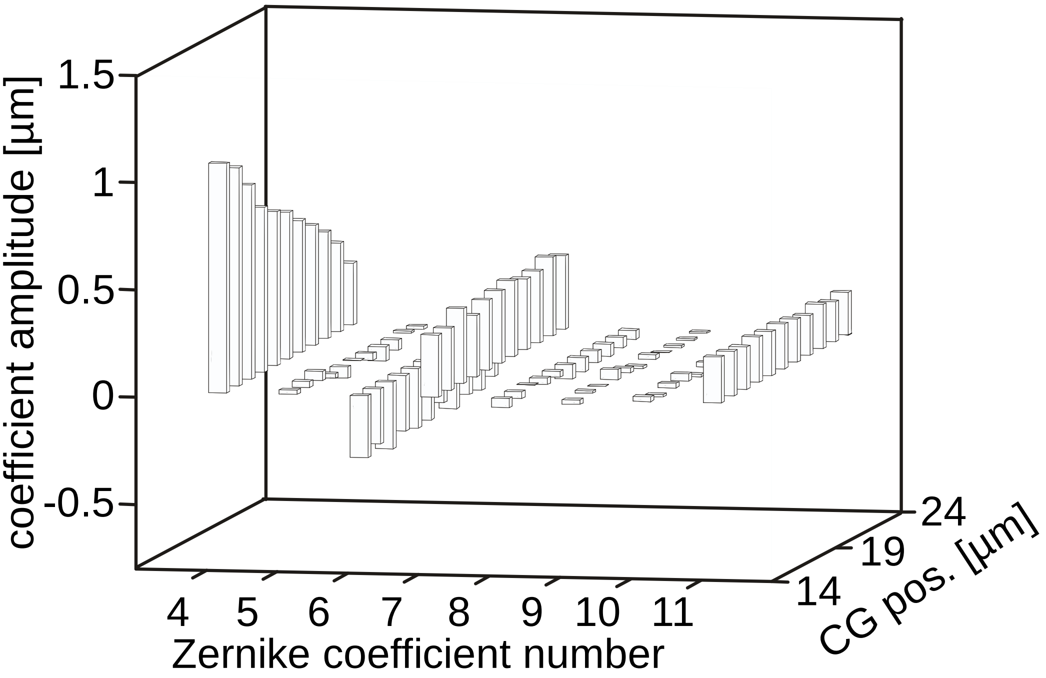

Figure 3.28: Zernike coefficients (ZC_4-ZC_{11}) as a function of CG position. As expected coma appears in the Zernike fit. Also expected is that only the coefficient for defocus (ZC_4) changes systematically with CG position.

3.2.4 Sensitivity and Accuracy

Lambert-Beer's law can be used to obtain a rough estimate of the fraction of light that passes the CG when experiments as described in subsections 3.2.2 and 3.2.3 are performed. The CG was assumed to be positioned 400 µm below the sample surface. Thus, essentially all light that comes from a sample depth between 385 µm and 415 µm can contribute to the signal. The portion of light, that is still unscattered after traveling a distance of 385 µm through the sample is given by $P_0 \cdot \exp(-385/400)$. The part that is unscattered after a distance of 415 µm is $P_0 \cdot \exp(-415/400)$. The difference between these two parts is the amount of light that is scattered once between 385 and 415 µm, and can in principle contribute to the signal. On its way back to the sample surface this amount of light is attenuated once more by a factor of approximately *1/e*. To obtain an order-of-magnitude estimate of the fraction of light that is scattered back into the objective, it was assumed that scattering in the sample is isotropic, i.e. the fraction of light that is scattered into an infinitesimal solid angle element dΩ is $1/(4p)$. The solid angle subtended by the objective is given by

$$\Omega = 2p\,(1-\cos a)\,. \tag{3.118}$$

Here a is the angle governed by the numerical aperture of the objective (Figure 3.29).

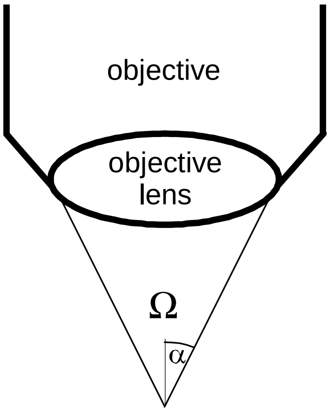

Figure 3.29: The solid angle of the objective.

Thus the amount of light gathered by the objective is given by the multiplication of the solid angle subtended by the objective and the fraction of light that is scattered into dΩ and thus the fraction of useful light (FUL) is given by

$$FUL_{theo} = \left(e^{-\frac{385}{400}} - e^{-\frac{415}{400}}\right) \cdot e^{-1} \cdot \frac{1}{2}\left(1 - \cos \arcsin \tfrac{NA}{n}\right). \tag{3.119}$$

The result for this estimate is $1.3 \cdot 10^{-3}$. To determine the fraction of light that passes the CG experimentally the square of the complex amplitude (cf. Eq. (2.56)) was used. For equal interferometer arm lengths this square is, if reference and sample arms are completely coherent, given by

$$\begin{aligned}\tilde{E}^2 &= \left[(I_1 - I_3) + i(I_4 - I_2)\right] \cdot \left[(I_1 - I_3) - i(I_4 - I_2)\right] \\ &= (I_1 - I_3)^2 + (I_4 - I_2)^2 \\ &= 16 \cdot I_{ref} \cdot I_{smp}\end{aligned} \tag{3.120}$$

Thus the coherent part of the sample arm light, which corresponds to the light that passes the CG, can be estimated from Eq. (3.120):

$$I_{coh\,theo} = \frac{\tilde{E}^2}{16 \cdot I_{ref}}. \tag{3.121}$$

Since the images taken in scattering samples suffer from speckle, the quadruplet used for CGWS does too (Figure 3.30). Applying Eq. (3.120) does not change this fact (Figure 3.30). It would be wrong, therefore, to simply sum up the entire pixel values of the squared complex amplitude image and divide this sum by the sum obtained in equal manner from the background corrected sample arm image to get the FUL. According to Lauterborn

[Lauterborn et al. 1993] the mean intensity of a speckle field is equal to its standard deviation and hence a mean and from that an overall intensity can be calculated. With the CG at one MFP below the surface of the scattering sample described in subsection 3.2.1 and under the assumption that reference and sample arm are completely coherent† the FUL was measured with a value of

$$FUL_{measured} = (0.55 \pm 0.08) \cdot 10^{-3}, \tag{3.122}$$

which is lower than the ‘Lambert-Beer’ value possibly due to polarization effects induced in the scattering sample. The $FUL_{measured}$ corresponds (according to subsection 2.4.2) to (2±0.3) photons per pixel and frame. This is considerably below the dark noise of the camera (cf. subsection 2.4.2), which is equivalent to ≈ 218 photons but still detectable due to the interferometric detection.

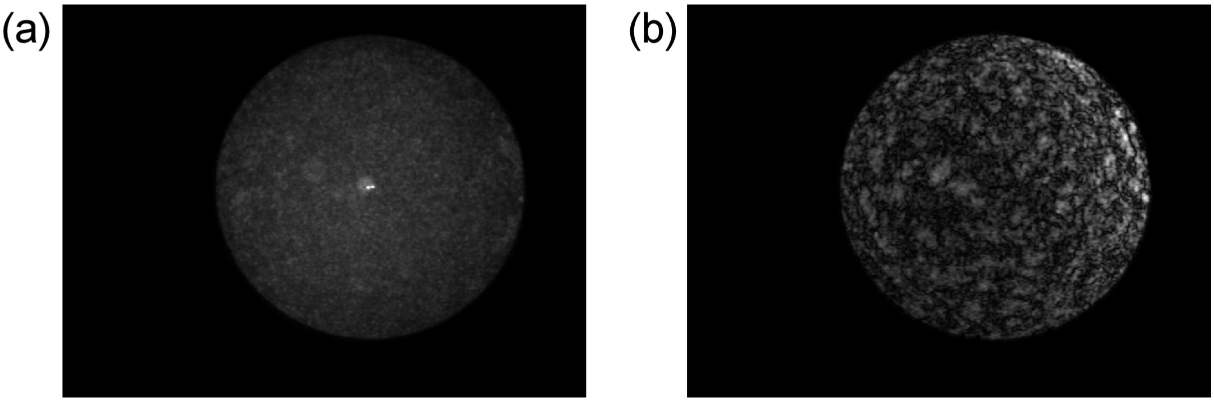

Figure 3.30: Background corrected image of the sample arm (a). Square of the complex amplitude calculated from a quadruplet of images. Clearly visible, both images suffer from speckles.

The standard deviation of the diffraction peak position found experimentally for $FUL_{measured}$ (cf. Eq.(3.122)) was s_P=11.91 µm. From this standard deviation the mean-square wave-front reconstruction error $s_{\hat{W}}^2$ can be calculated according to Eq. (2.21) of subsection 2.2.1:

$$s_{\hat{W}}^2 = s_g \cdot tr\left\{\left(D^T D\right)^{-1}\right\}. \tag{3.123}$$

---

† Experimentally it was found, using a mirror as a sample, that in the denominator of Eq. (3.120) a value of about 8 rather than 16 has to be used possibly due to incomplete polarization overlap. This is a subject of future work.

The mean-square error in each slope measurement, s_g^2, is calculated via $(s_P/f_{lenslet})^2$, with the focal length of the lenslets f_{lenlet}=10120 µm. Using the measured value of s_P=11.91 µm yields a root mean-square wave-front reconstruction error of

$$s_{\hat{W}} \approx 0.145\,\mu\text{m}. \tag{3.124}$$

This is equivalent to ≈ λ/6.

4 Summary and Future Prospects

In the dissertation at hand a new approach for measuring wave-fronts in strongly scattering samples, CGWS, was presented.

CGWS is mainly based on two techniques, Shack-Hartmann wave-front sensing and phase-shifting interferometry (PSI). These techniques were combined in an experimental setup that at its core contains a low-coherence interferometer with the microscope objective, the sample and a CCD camera in one arm, and the path length-varying element, a piezo-mounted mirror in the other, the reference arm. Coherence gating was achieved by applying a four-step PSI algorithm, which both rejects wrong path length light and extracts phase and thus wave-front information. In order to establish this algorithm by means of steps of the piezo an adequate electronic control circuitry was assembled. The extracted phase was used to calculate the complex field amplitude in the CCD sensor plane of the camera. Dividing the CCD chip virtually into small, square shaped compartments makes it possible to mimic the function of a Shack-Hartmann wave-front sensor (SHS) by numerically propagating the complex field amplitude through these compartments via Fourier transforms. The compartments thereby act as virtual lenses. A substantial advantage of such a virtual SHS, compared to a real one, is that a much larger effective dynamic range can be accessed because light intensity at the sensor plane is relatively uniform, avoiding pixel saturation, which is an issue in real SHS. Phase-slope extraction was performed by fitting the peak positions in the focal plane of the virtual lenses and comparing them to the lens centers. Since the phase slope is the directional derivative of the phase, a modal estimation algorithm for wave-front reconstruction can be applied and was implemented in MATLAB. The result of this algorithm was a set of the Zernike polynomial coefficients up to the fifth radial degree. They allow the approximation of the wave-front by a linear combination of 20 Zernike polynomials.

For the reconstruction as well as for the building of the piezo control circuitry it was indispensable to have detailed knowledge about some of the essential properties of the camera used. How these in general can be determined has been demonstrated.

In order to validate CGWS two different kinds of tests were carried out: First with a mirror and then with a strongly scattering phantom as a sample (400 µm scattering length, the focus 1 MFP below the sample surface). For both of these samples the performance of the CGWS was checked for defocus and astigmatism. In the case of the mirror as a sample defocus was induced by shifting the mirror parallel to the OA. For the scattering phantom defocus was induced by shifting the CG. Astigmatism was induced for both samples by inserting a glass cover slip between the samples and the objective with its surface normal tilted away from the OA. Unlike uniform curvature (defocus), which leads to a change of focus position but not shape, the aberrations caused by a tilted glass plate do lead to a distortion of the focus and need to be corrected for optimal imaging. Four different models for obtaining corresponding theoretical estimates were derived and partly implemented in MATLAB.

In the case of defocus, the expectation is that the Zernike defocus coefficient ZC_4 is dominant and varies linearly with changes (*Dz*) of the mirror or the CG, respectively. Both facts were confirmed by actual measurements. The value (dZC_4/dz) measured in the case of the mirror (-0.0968±0.0029) was in agreement with the theoretical estimate (-0.0999). For the scattering sample the measurement provides a slope (dZC_4/dz) of (–0.083±0.002), which is slightly smaller than expected (–0.0998). This small discrepancy is possibly due to the fact that the fitting algorithm used to determine the peak positions of the virtual SHS weighs backscattered light from regions closer to the focus more strongly. In both cases, the mirror and the scattering sample, all higher Zernike coefficients were small. The induced astigmatism should not change with the position of the mirror or the position of the CG. This was confirmed by measurements with a tilted glass cover slip between sample and objective. As qualitatively expected, only ZC_4 changed systematically in the real measurements with a slope (dZC_4/dz) of (–0.0960±0.0003) in the mirror measurement and (–0.073±0.003) in the scattering sample measurement. The theoretical estimates were –0.0999 for the mirror and –0.0998 for the scattering sample. For the mirror, the expectation for the astigmatism coefficient ZC_6 was –0.4651 μm, in comparison to the actual measurement (–0.4646±0.0013) μm. For the sample, ZC_6 was expected to have a value of –0.233 μm in comparison to the measurement (–0.264±0.026) μm. Different from the mirror sample, coma (ZC_7) is, as expected, present in case of the scattering sample. The measured value was ZC_7=(0.327±0.027) μm (expected value: ZC_7=0.409 μm). The discrepancies between theoretical estimates and measurements are probably, again, due to increased weighing of light from closer to the focus by the algorithm that fits the diffraction peak positions.

The fraction of light that passes the CG and thus can be used to measure the wave-front was theoretically estimated and compared with a real measurement. The interference signal falls off rapidly with arm length mismatch, which leads to a selection volume of about 6 picoliters and a depth discrimination of about 30 μm, given by the coherence length of the light source used. Using Lambert-Beer’s law it was estimated that the fraction of backscattered light that is used by the CGWS is about $1.3 \cdot 10^{-3}$. An actual measurement of this fraction yielded a value of $(0.55 \pm 0.08) \cdot 10^{-3}$ under the assumption of completely coherent interferometer arms with the discrepancy between estimate and measurement probably due to polarization effects induced by the scattering phantom. The measured fraction corresponds to (2±0.3) photons per camera pixel and frame. Finally, for this fraction of useful light the root mean-square wave-front reconstruction error was determined (result: λ/6).

In conclusion, CGWS allows the measurement of wave-front distortion in scattering samples in the presence of background light that is dominant by about three orders of magnitude. The coherence gating technique has the additional advantage of increasing the effective detection sensitivity, with potentially shot noise limited performance even for low-photon fluxes and detectors with large dark noise. This will allow the use of CMOS detector chips, which could contain additional procession circuitry to perform the PSI and even the wave-front calculations on the chip. The usability of such devices will be the topic of future work. To additionally improve CGWS it is necessary to optimize the algorithm for finding the diffraction peak positions. Future work also has to focus on the development of a simulation for astigmatism for samples consisting not only of one but of many QPSs. Additionally, considerations on how to further reduce the influence of speckle noise have to be made. However, the major aim of the near future will be the extension of CGWS to a fully working closed-loop adaptive correction system. Once accomplished, this will allow applying pre-emptive corrections to the wave-front, resulting in the improvement of the quality of the optical focus. This will considerably restore the loss of resolution induced by sample inhomogeneities and, thereby, significantly increase the tissue depth penetration.

References

[Albert et al. 2000] Albert, O., L. Sherman, G. Mourou, T. B. Norris and G. Vdovin (2000). "Smart microscope: an adaptive optics learning system for aberration correction in multiphoton confocal microscopy." Optics Letters **25**(1): 52-54.

[Babcock 1953] Babcock, H. W. (1953). "The possibility of compensating astronomical seeing." Publications of the Astronomical Society of the Pacific **65**: 229-236.

[Bille et al. 1989] Bille, J. F., B. Grimm, J. Liang and K. Mueller (1989). "Imaging of the retina by scanning laser tomography." Proceedings of Spie - the International Society for Optical Engineering **1161**: 417-25.

[Bohren and Huffman 1998] Bohren, C. F. and D. R. Huffman (1998). Absorption and Scattering of Light by Small Particles. New York, Chichester, Weinheim, Brisbane, Singapore, Toronto, John Wiley & Sons, Inc.

[Born and Wolf 1999] Born, M. and E. Wolf (1999). Principles of Optics. Cambridge, U.K., Cambridge University Press.

[Bronstein et al. 1995] Bronstein, I. N., K. A. Semendjajew, G. Musiol and H. Mühlig (1995). Taschenbuch der Mathematik. Thun und Frankfurt am Main, Verlag Harri Deutsch.

[Brown et al. 2001] Brown, E. B., R. B. Campbell, Y. Tsuzuki, L. Xu, P. Carmeliet, D. Fukumura and R. K. Jain (2001). "In vivo measurement of gene expression, angiogenesis and physiological function in tumors using multiphoton laser scanning microscopy." Nature Medicine **7**(7): 864-868.

[Carré 1966] Carré, P. (1966). "Installation et utilisation du comparateur photoelectrique et interferentiel du Bureau International des Poids et Mesures." Metrologia **2**(1): 13-23.

[Centonze and White 1998] Centonze, V. E. and J. G. White (1998). "Multiphoton Excitation Provides Optical Sections from Deeper within Scattering Specimens than Confocal Imaging." Biophys. J. **75**(4): 2015-2024.

[Christie et al. 2001] Christie, R. H., B. J. Bacskai, W. R. Zipfel, R. M. Williams, S. T. Kajdasz, W. W. Webb and B. T. Hyman (2001). "Growth arrest of individual senile plaques in a model of Alzheimer's disease observed by in vivo multiphoton microscopy." Journal of Neuroscience **21**(3): 858-864.

[Crane 1969] Crane, R. (1969). "Interference Phase Measurement." Applied Optics **8**(3): 538-542.

[Cubalchini 1979] Cubalchini, R. (1979). "Modal Wavefront Estimation from Phase Derivative Measurements." Journal of the Optical Society of America **69**(7): 972-977.

[Dai 1996] Dai, G. M. (1996). "Modal wave-front reconstruction with zernike polynomials and Karhunen-Loeve functions." Journal of the Optical Society of America a-Optics Image Science and Vision **13**(6): 1218-1225.

[Denk et al. 1994] Denk, W., K. R. Delaney, A. Gelperin, D. Kleinfeld, B. W. Strowbridge, D. W. Tank and R. Yuste (1994). "Anatomical and functional imaging of neurons using 2-photon laser scanning microscopy." Journal of Neuroscience Methods **54**(2): 151-162.

[Denk et al. 1995] Denk, W., D. W. Piston and W. W. Webb (1995). Two-Photon Molecular Excitation in Laser-Scanning Microscopy. Handbook of Biological Confocal Microscopy. J. B. Pawley. New York and London, Plenum Press**:** 445-458.

[Denk et al. 1990] Denk, W., J. H. Strickler and W. W. Webb (1990). "Two-Photon Laser Scanning Fluorescence Microscopy." Science **248**(4951): 73-76.

[Denk et al. 1995] Denk, W., M. Sugimori and R. Llinas (1995). "2 Types of Calcium Response Limited to Single Spines in Cerebellar Purkinje-Cells." Proceedings of the National Academy of Sciences of the United States of America **92**(18): 8279-8282.

[Denk and Svoboda 1997] Denk, W. and K. Svoboda (1997). "Photon upmanship: Why multiphoton imaging is more than a gimmick." Neuron **18**(3): 351-357.

[Denk et al. 1996] Denk, W., R. Yuste, K. Svoboda and D. W. Tank (1996). "Imaging calcium dynamics in dendritic spines." Current Opinion in Neurobiology **6**(3): 372-378.

[Dirnagl et al. 1991] Dirnagl, U., A. Villringer, R. Gebhardt, R. L. Haberl, P. Schmiedek and K. M. Einhaupl (1991). "3-Dimensional Reconstruction of the Rat-Brain Cortical Microcirculation Invivo." Journal of Cerebral Blood Flow and Metabolism **11**(3): 353-360.

[Duguay and Mattick 1971] Duguay, M. A. and A. T. Mattick (1971). "Ultrahigh Speed Photography of Picosecond Light Pulses and Echoes." Applied Optics **10**(9): 2162-&.

[Euler et al. 2002] Euler, T., P. B. Detwiler and W. Denk (2002). "Directionally selective calcium signals in dendrites of starburst amacrine cells." Nature **418**(6900): 845-852.

[Feierabend et al. 2004] Feierabend, M., M. Rückel and W. Denk (2004). "Coherence-gated wave-front sensing in strongly scattering samples." Optics Letters **submitted**.

[Foy and Labeyrie 1985] Foy, R. and A. Labeyrie (1985). "Feasibility of Adaptive Telescope with Laser Probe." Astronomy and Astrophysics **152**(2): L29-L31.

[Geary 1995] Geary, J. M. (1995). Introduction to Wavefront Sensors. Bellingham, SPIE Optical Engineering Press.

[Golub and Van Loan 1983] Golub, G. H. and C. F. Van Loan (1983). Matrix Computations. Baltimore, The Johns Hopkins University Press.

[Goodman 2000] Goodman, J. W. (2000). Statistical Optics. New York, John Wiley and Sons.

[Göppert-Mayer 1931] Göppert-Mayer, M. (1931). "Über Elementarakte mit zwei Quantensprüngen." Annalen der Physik **9**: 273-294.

[Hardy 1998] Hardy, J. W. (1998). Adaptive Optics For Astronomical Telescopes. Oxford, Oxford University Press.

[Hartmann 1900] Hartmann, J. (1900). "Bemerkungen über den Bau und die Justirung von Spektrographen." Zeitschrift für Instrumentenkunde **20**: 47-58.

[Hartmann 1904] Hartmann, J. (1904). "Objektivuntersuchungen." Zeitschrift für Instrumentenkunde **24**: 1-21.

[Hecht 1990] Hecht, E. (1990). Optics. Reading, Massachusetts, Addison-Wesley Publishing Company.

[Helmchen and Denk 2002] Helmchen, F. and W. Denk (2002). "New developments in multiphoton microscopy." Current Opinion in Neurobiology **12**(5): 593-601.

[Hopt and Neher 2001] Hopt, A. and E. Neher (2001). "Highly nonlinear photodamage in two-photon fluorescence microscopy." Biophysical Journal **80**(4): 2029-2036.

[Huang et al. 1991] Huang, D., E. A. Swanson, C. P. Lin, J. S. Schuman, W. G. Stinson, W. Chang, M. R. Hee, T. Flotte, K. Gregory, C. A. Puliafito and J. G. Fujimoto (1991). "Optical Coherence Tomography." Science **254**(5035): 1178-1181.

[Humphreys et al. 1991] Humphreys, R. A., C. A. Primmerman, L. C. Bradley and J. Herrmann (1991). "Atmospheric-Turbulence Measurements Using a Synthetic Beacon in the Mesospheric Sodium Layer." Optics Letters **16**(18): 1367-1369.

[Inoué and Spring 1997] Inoué, S. and K. R. Spring (1997). Video Microscopy The Fundamentals. New York and London, Plenum Press.

[Juškaitis 2003] Juškaitis, R. (2003). Characterizing High Numerical Aperture Microscope Objective Lenses. Optical Imaging and Microscopy. P. Török and F.-J. Kao. Berlin Heidelberg New York, Springer-Verlag.

[Kaiser and Garrett 1961] Kaiser, W. and C. G. B. Garrett (1961). "Two-Photon excitation in CaF2:Eu2+." Physical Review Letters **7**(6): 229-231.

[Koester et al. 1999] Koester, H. J., D. Baur, R. Uhl and S. W. Hell (1999). "Ca2+ fluorescence imaging with pico- and femtosecond two-photon excitation: Signal and photodamage." Biophysical Journal **77**(4): 2226-2236.

[König et al. 1999] König, K., T. W. Becker, P. Fischer, I. Riemann and K. J. Halbhuber (1999). "Pulse-length dependence of cellular response to intense near-infrared laser pulses in multiphoton microscopes." Optics Letters **24**(2): 113-115.

[Kuhn et al. 2004] Kuhn, B., P. Fromherz and W. Denk (2004). "High Sensitivity of Stark-Shift Voltage-Sensing Dyes by One- or Two-Photon Excitation near the Red Spectral Edge." Biophysical Journal **in press**.

[Lauterborn et al. 1993] Lauterborn, W., T. Kurz and M. Wiesenfeldt (1993). Kohärente Optik. Berlin, Heidelberg, New York, Springer-Verlag.

[Liang et al. 1997] Liang, J. Z., D. R. Williams and D. T. Miller (1997). "Supernormal vision and high-resolution retinal imaging through adaptive optics." Journal of the Optical Society of America a-Optics Image Science and Vision **14**(11): 2884-2892.

[Linnik 1993] Linnik, V. P. (1993). On the possibility of reducing the influence of atmospheric seeing on the image quality of stars. Original 1957 article translated and reprinted. ESO Conference and Workshop Proccedings No. 48, Garching, Germany.

[Malacara 1992] Malacara, D. (1992). Optical Shop testing. New York, John Wiley & Sons, Inc.

[Marsh et al. 2003] Marsh, P. N., D. Burns and J. M. Girkin (2003). "Practical implementation of adaptive optics in multiphoton microscopy." Optics Express **11**(10): 1123-1130.

[Merkle et al. 1989] Merkle, F., P. Kern, P. Lena, F. Rigaut, J. C. Fontanella, G. Rousset, C. Boyer, J. P. Gaffard and P. Jagourel (1989). "Successful Tests of Adaptive Optics." ESO Messenger(58): 1-4.

[Mie 1908] Mie, G. (1908). "Beiträge zur Optik trüber Medien, speziell kolloidaler Metallösungen." Annalen der Physik **25**(4): 377-445.

[Minsky 1961] Minsky, M. (1961). Microscopy Apparatus. U.S. Patent 3013467. USA.

[Minsky 1988] Minsky, M. (1988). "Memoir on Inventing the Confocal Scanning Microscope." Scanning **10**(4): 128-138.

[Neil et al. 2000] Neil, M. A. A., R. Juškaitis, M. J. Booth, T. Wilson, T. Tanaka and S. Kawata (2000). "Adaptive aberration correction in a two-photon microscope." Journal of Microscopy-Oxford **200**: 105-108.

[Noll 1976] Noll, R. J. (1976). "Zernike Polynomials and Atmospheric-Turbulence." Journal of the Optical Society of America **66**(3): 207-211.

[Oertner et al. 2002] Oertner, T. G., B. L. Sabatini, E. A. Nimchinsky and K. Svoboda (2002). "Facilitation at single synapses probed with optical quantal analysis." Nature Neuroscience **5**(7): 657-664.

[Rayces 1964] Rayces, J. L. (1964). "Exact Relation between Wave Aberration + Ray Aberration." Optica Acta **11**(2): 85-&.

[Saleh and Teich 1991] Saleh, B. E. A. and M. C. Teich (1991). Fundamentals Of Photonics. New York, John Wiley & Sons, Inc.

[Shack and Platt 1971] Shack, R. V. and B. C. Platt (1971). "Lenticular Hartmann-screen." Optical Sciences Center Newsletter **5**(1): 15-16.

[Sherman et al. 2002] Sherman, L., J. Y. Ye, O. Albert and T. B. Norris (2002). "Adaptive correction of depth-induced aberrations in multiphoton scanning microscopy using a deformable mirror." Journal of Microscopy-Oxford **206**: 65-71.

[Siegman 1986] Siegman, A. E. (1986). Lasers. Mill Valley, California, University Science Books.

[Southwell 1980] Southwell, W. H. (1980). "Wave-Front Estimation from Wave-Front Slope Measurements." Journal of the Optical Society of America **70**(8): 998-1006.

[Spence et al. 1991] Spence, D. E., P. N. Kean and W. Sibbett (1991). "60-Fsec Pulse Generation from a Self-Mode-Locked Ti-Sapphire Laser." Optics Letters **16**(1): 42-44.

[Svoboda and Block 1994] Svoboda, K. and S. M. Block (1994). "Biological Applications of Optical Forces." Annual Review of Biophysics and Biomolecular Structure **23**: 247-285.

[Svoboda et al. 1997] Svoboda, K., W. Denk, D. Kleinfeld and D. W. Tank (1997). "In vivo dendritic calcium dynamics in neocortical pyramidal neurons." Nature **385**(6612): 161-165.

[Taylor 1997] Taylor, J. R. (1997). An Introduction To Error Analysis. Sausalito, California, University Science Books.

[Theer et al. 2003] Theer, P., M. T. Hasan and W. Denk (2003). "Two-photon imaging to a depth of 1000 mu m in living brains by use of a Ti : Al2O3 regenerative amplifier." Optics Letters **28**(12): 1022-1024.

[Tyson 1997] Tyson, R. K. (1997). Principles Of Adaptive Optics. Boston, Academic Press.

[Yura and Tavis 1985] Yura, H. T. and M. T. Tavis (1985). "Centroid Anisoplanatism." Journal of the Optical Society of America a-Optics Image Science and Vision **2**(5): 765-773.

[Yuste et al. 1999] Yuste, R., A. Majewska, S. S. Cash and W. Denk (1999). "Mechanisms of calcium influx into hippocampal spines: Heterogeneity among spines, coincidence detection by NMDA receptors, and optical quantal analysis." Journal of Neuroscience **19**(6): 1976-1987.

[Zernike 1934] Zernike, F. (1934). "Beugungstheorie des Schneidenverfahrens und seiner verbesserten Form, der Phasenkontrastmethode." Physica 1: 689-704.

Acknowledgments

Here I would like to express my gratitude to all those people who helped me in completing this thesis.

In particular thanks to

- **Prof. Dr. Winfried Denk**

  for giving me the opportunity to work on this very interesting and challenging topic and for his support and professional scientific advice during my time as a PhD student in his department.

- **Prof. Dr. Josef F. Bille**

  for his willingness to act as second referee for this work.

- **Dr. Dorine Keusters, Markus Rückel and Patrick Theer**

  for many productive discussions and valuable suggestions about the topics of this work in particular and on the topics of optics in general. Dorine and Markus also for careful reading of the manuscript.

- **Michael Müller, Jürgen “Schorsch” Sawinski and Jürgen Tritthardt**

  for their appreciated advice in and around the world of computers and electronics.

- **Dr. Thomas Euler, Dr. Bernd Kuhn**

  for their non-academic advice. Bernd also for careful reading of the manuscript.

- **The people of the mechanical workshop**

  for machining precision parts.

- **Christa Hörner-Ehm**

  for helping with all kinds of administrative stuff and many, many other things.

- **Megan and Stephan Frank, Carlo Götz, Dr. Wolfgang Kirsch, Eva Kranz, Dr. Gerhard Laubscher and Kirsty Macdonald**

  for careful reading of the manuscript.

- **The remaining colleagues of the BMO department**

  for the time they shared with me.

- **My family**

  for making this way of education possible to me.

- **My wife Silke**

  for her perpetual, unconditional support, her never-ending patience and her understanding.